

HABILITATION À DIRIGER DES RECHERCHES

Pour le grade de

HDR DE L'UNIVERSITÉ SAVOIE MONT BLANC

Spécialité : **Sciences Terre, Univers et Environnement**

Arrêté ministériel : 25 mai 2016

Présentée par

Yajing YAN

préparée au sein du **Laboratoire LISTIC**
dans **l'École Doctorale SISEO**

**Vers la surveillance opérationnelle de la
déformation de la Terre et la prévision
des risques naturels**

**Towards operational monitoring of Earth
deformation and prediction of natural ha-
zards**

HDR soutenue publiquement à Annecy le XXX 2021
devant le jury composé de :

M. Jérôme MARS

Professeur des Universités, Université Grenoble Alpes, Rapporteur

M. Jean-Philippe OVARLEZ

Directeur de recherche, ONERA, Rapporteur

Mme Cécile LASSERRE

Directrice de recherche, CNRS, Rapportrice

Mme Florence TUPIN

Professeur Télécom, Télécom ParisTech, Examinatrice

M. Laurent FERRO-FAMIL

Professeur des Universités, Université de Rennes 1, Examineur

M. Guillaume GINOLHAC

Professeur des Universités, Université Savoie Mont Blanc, Examineur

Abstract

My research activities have been developed around Synthetic Aperture Radar (SAR) imagery, but cover a broad range of subjects starting from the exploitation of SAR images for displacement measurement at the Earth's surface until the estimation of geophysical parameters which characterize the subsurface geological structures that induce the displacement observed at the surface. I am interested in both methodological developments, especially those to better exploit the mass of available SAR data, and applications of the methods to targets of geophysical interest such as earthquakes, volcanoes, subsidence in urban environments and alpine glaciers. In this report, I give a summary of my research works carried out in recent years, mainly through Master internships and Ph.D theses that I co-supervised or co-supervise. I also introduce the related state-of-the-art works, as well as the perspectives of my research activities. These works will be presented in line with four research axes organized according to four different scientific objectives : estimation of the displacement from time series of SAR images, reconstruction of the missing data in the time series of SAR/optical displacement, analysis of the time series of displacement measurement and estimation and prediction of geophysical parameters.

Keywords : SAR, multi-temporal InSAR, displacement measurement, time series, inversion, data assimilation.

Résumé

Mon activité de recherche se développe autour de l'imagerie SAR (Synthetic Aperture Radar), mais couvre un spectre large des sujets allant de l'exploitation des images SAR pour la mesure de déplacement à la surface de la Terre jusqu'à l'estimation des paramètres géophysiques qui caractérisent la source en profondeur du déplacement observé en surface. Je m'intéresse à la fois aux développements méthodologiques, notamment ceux pour mieux exploiter la masse de données SAR disponibles, et aux applications des méthodes aux objets d'intérêt géophysiques telles que les séismes, les volcans, les subsidences en milieux urbains et les glaciers alpins. Dans ce rapport, je présente de manière synthétique mes travaux de recherche menés ces dernières années essentiellement à travers des stages et thèses que j'ai co-encadrés ou co-encadre; je présente également l'état de l'art permettant un positionnement approprié de mes travaux, ainsi que les perspectives de mon activité de recherche. Ces travaux seront présentés suivant quatre axes de recherche organisés selon quatre objectifs scientifiques différents : l'estimation du déplacement à partir de séries temporelles d'images SAR, la reconstruction des données manquantes dans les séries temporelles de déplacement SAR/optique, l'analyse des séries temporelles de mesure de déplacement, et l'estimation et la prédiction des paramètres géophysiques.

Mots-clefs : SAR, multi-temporal InSAR, mesure de déplacement, série temporelle, inversion, assimilation de données.

Table des matières

Abstract	i
Résumé	iii
Table of content	vi
I Administrative part	1
II Research work	22
Introduction	23
1 Measure displacement from SAR images	26
1.1 Introduction	26
1.2 SAR images in displacement measurement	27
1.2.1 Differential inteferometry SAR	27
1.2.2 Offset Tracking	28
1.3 Recent advances in multi-temporal InSAR	29
1.3.1 Permanent Scatterer Interferometry	31
1.3.2 Small BAseline Subset	33
1.3.3 Phase linking approaches	35
1.3.4 Multi-link InSAR	40
1.3.5 Least-square phase estimator	41
1.3.6 Combination of PSI & DSI	43
1.3.7 Sequential estimator	44
1.4 Conclusion & perspective	45
2 Impute missing data in displacement measurement time series	48
2.1 Introduction	48
2.2 Common theoretical background - EOF-based analysis	49
2.2.1 Data organization	49
2.2.2 Sample covariance estimation	49
2.2.3 Eigenvalue decomposition	50
2.2.4 Data reconstruction	50
2.3 Principal modes method	51
2.3.1 Methodology	51
2.3.2 Case study	53
2.3.3 Discussions	58
2.4 EM-EOF method	59
2.4.1 Methodology	59
2.4.2 Case study	60
2.4.3 Discussions	64

2.5	Extended EM-EOF method	65
2.5.1	Methodology	65
2.5.2	Case study	68
2.5.3	Discussions	70
2.6	Conclusions & perspective	71
3	Explore displacement measurements time series	73
3.1	Introduction	73
3.2	Least-square inversion	74
3.2.1	3D displacement estimation	74
3.2.2	Displacement time series fusion	75
3.3	Multiscale InSAR time series analysis	81
3.4	Spatio-temporal random effect model	83
3.5	Kalman filter based time series analysis	84
3.6	Median of Multiple Common Master Series	86
3.7	Machine learning based approaches	87
3.7.1	Traditional ML approaches	88
3.7.2	Neural networks approaches	90
3.8	Conclusions & Perspectives	91
4	Estimate and predict geophysical parameters by inversion and data assimilation	93
4.1	Introduction	93
4.2	Model driven approaches	94
4.2.1	Inversion	94
4.2.2	Data assimilation	98
4.2.3	Discussions	109
4.3	Data driven approaches	110
4.4	Conclusion & perspectives	111
	Conclusions & perspectives	114

Première partie

Administrative part

Curriculum vitæ

Situation administrative

- ▷ Prénom : Yajing
- ▷ Nom : YAN
- ▷ Date de naissance : 26/01/1984
- ▷ Adresse : 17 avenue du Rhône, 74000, Annecy
- ▷ Fonction actuelle : Maître de Conférences - classe normale
- ▷ Date d'installation : 01/09/2014
- ▷ Laboratoire : Laboratoire d'Informatique, Systèmes, Traitement de l'Information et de la Connaissance (LISTIC)
- ▷ Établissement : Polytech Annecy-Chambéry, Université Savoie Mont-Blanc

Parcours professionnel

- 09/2014 - Aujourd'hui : **Maître de Conférences** à l'Université Savoie Mont-Blanc (USMB), Annecy.
 - Recherche : LISTIC
 - Enseignement : Polytech Annecy-Chambéry.
- 07/2012 - 08/2014 : **Chercheuse post-doctorale** à l'Université de Liège, Liège, Belgique.
 - Recherche : GeoHydrodynamics and Environment Research (GHER), travaux dans le cadre du projet Européen "Stochastic Assimilation for the Next Generation Ocean Model Applications (SANGOMA)", en collaboration étroite avec MEOM IGE (Grenoble)
- 01/2012 - 06/2012 : **Chercheuse post-doctorale** à l'Université de Rennes 1, Rennes,
 - Recherche : Institut d'Électronique et de Télécommunications de Rennes (IETR), travaux dans le cadre du projet ANR "Extraction et Fusion d'Informations pour la mesure de Déplacement par Imagerie Radar (EFIDIR)", en collaboration étroite avec Gipsa-lab.
- 10/2008 - 12/2011 : **Doctorante** à l'Université Savoie Mont-Blanc, Annecy
 - Recherche : sous la direction d'Emmanuel Trouvé (LISTIC) et Virginie Pinel (ISTerre), travaux dans le cadre du projet ANR EFIDIR
 - Enseignement : vacataire à Polytech Annecy-Chambéry et à l'IUT d'Annecy

Formation

- 10/2008 – 12/2011 : **Thèse de doctorat**, laboratoires LISTIC/ISTerre, Université Savoie Mont-Blanc.
Nominée au Prix de thèse de l'Université de Grenoble 2012.
- 09/2007 – 06/2008 : **Master**, Méthode Physique en Télédétection, Université Paris 6.
Major de promotion.
- 09/2006 – 06/2007 : **Maîtrise** en Géosciences, Université Lille 1.
- 09/2005 – 06/2006 : **Licence** en Géosciences, Université Lille 1.
- 09/2003 – 06/2005 : **Licence** 1 et 2 en Géo-informatique, Université de Tongji, Shanghai, Chine.
Major de promotion.

Activités pédagogiques

Mon activité d'enseignement a débuté durant ma thèse, puis s'est poursuivie lors de ma prise de poste MCF. Ci-dessous une liste des domaines dans lesquels je suis intervenue en enseignement :

- Algorithmique & numération
- Base de données
- Système embarqué
- Traitement du signal et d'images

Quand j'étais en thèse, je suis intervenue, sous forme de vacation, dans des modules de traitement d'images dans la filière "Instrumentation Automatique Informatique" (IAI) à Polytech Annecy-Chambéry et au département informatique à l'IUT d'Annecy. Depuis ma prise de poste MCF, j'interviens principalement dans la filière IAI à Polytech Annecy-Chambéry. J'interviens également dans les filières Mécanique & Mécatronique (MM) et Informatique Données et Usage (IDU) dans des modules informatiques du tronc commun.

Mes enseignements ont été dispensés à des publics variés, incluant les étudiants en cycle préparatoire (PEIP) (ou L1) et en cycle ingénieur de l'année 3 à l'année 5. En plus des enseignements classiques, je m'investis également dans les enseignements innovants développés au sein de Polytech Annecy-Chambéry. Je me charge de plus des suivis de stages ingénieurs et de projets de fin d'études.

Lors de mes deux premières années en poste MCF (09/2014 - 08/2016), j'avais une décharge de 64 h en enseignement, mon service était limité à 128 h/an. Depuis septembre 2016, le volume d'enseignement annuel que j'effectue est autour de 250 h (y compris les suivis de stages et projets).

Enseignements classiques

Une partie importante de mes enseignements correspondent aux enseignements classiques sous forme de CM/TD/TP. Je suis la responsable de deux modules, Corrélation d'images (Ing. 4) et Technique Traitement de l'Information (Ing. 5) dans la filière IAI. J'étais la responsable du module "Système embarqué I" (Ing. 4) dans la filière MM pendant la période 2015 - 2020.

La Table 1 présente un résumé des matières et des heures d'enseignement classique que j'effectue depuis septembre 2016 (après la décharge jeune MCF). Pour certaines matières (e.g. Système embarqué I, Signaux aléatoires, Corrélation d'images et Technique traitement de l'information) en ingénieur 4^e et 5^e année, le nombre d'heures varie légèrement d'une année à l'autre en fonction du nombre d'étudiants recrutés.

Module	Volume (h/an)			Public
	CM	TD	TP	
Algorithmique & numération	-	21	32	PEIP 1, Ing.3
Base de données	-	4,5	36	Ing.3
Signal & image : opérateur de base	-	12	-	Ing.3
Imagerie & Télédétection	*	*	12	Ing.3
Système embarqué I	-	9/12	52	Ing.4
Signaux aléatoires	-	0/12	12	Ing.4
Corrélation d'images	4,5	4,5/9	12	Ing.4
Technique traitement de l'information	*	*	10/20	Ing.5
Total	4,5	51/70,5	166/176	-

Tableau 1 – Résumé des matières et des heures d'enseignement classique que j'effectue depuis septembre 2016. * signifie que le type d'enseignement n'existe pas dans le module, alors que – signifie que je n'y intervins pas.

Enseignements innovants

En plus des enseignements classiques, je m'investis également dans les enseignements innovants, Apprentissage par Problème et par Projet (APP), mis en place dans la filière IAI au sein de Polytech Annecy-Chambéry. En APP, les étudiants travaillent en groupe (composé de 4 à 8 étudiants qui souhaitent travailler sur le même sujet) sous forme de projet pendant 4 semestres (S6 - S9). En plus des problèmes techniques à résoudre, les étudiants se forment à gérer et organiser leurs projets. Les tuteurs enseignants ont le rôle de guider les étudiants dans l'avancement de leurs projets, avec un encadrement de plus en plus lâche au cours des semestres afin de les mener vers l'autonomie. L'évaluation à la fin de chaque semestre comprend une présentation orale collective, un rapport écrit collectif et un entretien individuel. Lors de ce dernier, les étudiants sont évalués par compétence avec 4 niveaux (notion, application, maîtrise, avancé), selon la grille des compétences techniques et transversales établie par l'équipe APP.

Je fais partie de l'équipe APP depuis ma prise de poste MCF. J'interviens en thème "Imagerie pour l'Environnement" (IE). J'étais la responsable du sous-thème "Imagerie Dronoportée et Télédétection" pendant la période de 2016 - 2019 et je prends la responsabilité du sous-thème "Imagerie satellitaire et Télédétection" depuis janvier 2021. Je participe régulièrement aux réunions APP en tant que représentant IE et j'ai participé à l'établissement de la grille des compétences. J'ai obtenu en juillet 2016 le brevet de télépilotage d'aéronef Ultra-Léger Motorisé (ULM) et le certificat d'inspecteur de pilote d'aéronef ULM afin de faciliter l'encadrement du projet "Imagerie Dronoportée et Télédétection". Par rapport aux enseignements classiques, l'encadrement et le suivi des projets APP nécessitent beaucoup plus d'énergie.

En plus des APPs, dans le module "Technique Traitement de l'Information", dont je suis responsable, j'interviens avec 3 autres collègues portant des compétences complètement différentes, nous gardons la même pédagogie que les APPs. L'objectif de ce module consiste à développer une application Android qui permet de reconnaître les visages en utilisant l'analyse en composante principale. Les étudiants organisent les 3 tâches techniques : reconnaissance de visages par analyse en composante principale, développement Android et communication, dans un projet en déployant

des méthodes avancées en gestion de projet. La stratégie de l'évaluation du module est aussi la même que celle en APP. Cette pédagogie enrichit largement les compétences que les étudiants peuvent acquérir dans un module et les aide à se préparer plus rapidement pour leur future carrière d'ingénieur.

Stages et projets Recherche & Développement (R&D)

Chaque année, je me charge des suivis de 4 stages ingénieurs de 4^e ou 5^e année en France ou à l'étranger dans la filière IAI. De temps en temps, je suis les stages (orientée informatique) de 4^e année dans la filière MM suite à la demande des collègues.

J'encadre également des Travaux Personnels Encadrés (TPE) au cycle préparatoire et des projets R&D de fin d'études de la filière IAI.

Réunions pédagogiques

Pendant les deux premières années en poste MCF, j'ai participé régulièrement aux formations et ateliers pédagogiques afin de renforcer mes compétences en enseignement. Plus tard, suite à l'augmentation des charges d'enseignement, de recherches et administratives, je participe moins à ce genre de formations. Cependant, je maintiens toujours ma participation aux réunions pédagogiques pour les APPs et aux réunions organisées au sein de la filière IAI.

Activités de recherche

Mon activité de recherche se développe autour de l'imagerie SAR (Synthetic Aperture Radar), mais couvre un spectre large des sujets allant de l'exploitation des images SAR pour la mesure de déplacement à la surface de la Terre jusqu'à l'estimation des paramètres géophysiques qui caractérisent la source en profondeur du déplacement observé en surface. Je m'intéresse à la fois aux développements méthodologiques, notamment ceux pour mieux exploiter la masse de données disponibles, et aux applications des méthodes aux objets d'intérêt géophysiques telles que les séismes, les volcans, les subsidences en milieux urbains et glaciers alpins.

Ci-dessous sont présentés les 4 grands axes de mon activité de recherche.

Mesure de déplacement par imagerie SAR

Les images SAR constituent actuellement la source principale d'information pour la mesure de déplacement terrestre, grâce à leur grande couverture spatiale et leur disponibilité régulière. Un grand nombre de méthodes Interférométrie SAR (InSAR) multi-temporelles ont été développées, grâce auxquelles l'analyse et le suivi pluriannuels du déplacement deviennent possibles et la précision de la mesure de déplacement atteint l'ordre du millimètre par an. Cependant, ces dernières années, le développement méthodologique en InSAR multi-temporelle voit un ralentissement. Plus d'efforts ont été menés à construire des systèmes de surveillance à l'échelle nationale et à développer des services de traitement automatique en ligne. D'autre part, l'exploitation de la technique InSAR dans des contextes opérationnels en génie civil et en surveillance des risques naturels commence à voir le jour, mais leur application est souvent limitée par la difficulté d'intégrer de manière graduelle des nouvelles images dans une chaîne de traitement plus ou moins compliquée.

Ma première expérience en mesure du déplacement par image SAR date de mon stage M2 pour lequel j'ai utilisé la méthode InSAR multi-temporelle, Permanent Scatterer (PS), pour estimer la vitesse de la subsidence de la ville de Mexico (Yan et al., 2012). Durant ma thèse, j'ai utilisé la technique InSAR classique et la technique de la corrélation d'amplitude pour calculer les champs de déplacement induits par le séisme du Pakistan en 2015. Ces premières activités étaient plutôt sur la prise en main et l'application des méthodes qui existaient à l'époque.

J'ai repris mon activité en mesure du déplacement par image SAR depuis l'encadrement de la thèse de Matthias Jauvin (taux d'encadrement 40%). Dans cette thèse, la méthode PS a été appliquée aux séries temporelles d'images Sentinel-1 dans un contexte opérationnel pour la surveillance de grand chantier, i.e. l'exploitation des lignes de métro à Paris. Pour répondre au besoin d'un suivi régulier, une mise à jour tous les 3 mois de la carte de déplacement a été effectuée par relance de la chaîne de traitement en ajoutant les nouvelles images. Des résultats cohérents avec les mesures in situ ont été obtenus, ce qui a permis de convaincre de l'intérêt de l'InSAR auprès des maîtres de chantier, malgré une stratégie de traitement assez lourde. À cause de la confidentialité, ces travaux n'ont pas pu être publiés. Matthias a étudié également la faisabilité de l'InSAR avec les images Sentinel-1 disponibles tous les 6 jours pour mesurer l'écoulement des glaciers alpins. Il a proposé une méthode PS "ad hoc", avec l'aide des installations des coins réflecteurs, pour mesurer

les déplacements sur les moraines (Jauvin et al., 2019). Sur les glaciers, malgré la présence des franges interférométriques sur certains endroits pour certaines dates, une application systématique de l'InSAR pour suivre les mouvements des glaciers alpins reste toujours pessimiste.

Étant donné la conclusion sur l'utilisation de l'InSAR avec les données Sentinel-1 pour mesurer les déplacements des glaciers alpins, dans la thèse de Suvrat Kaushik (taux d'encadrement 25%), nous avons proposé d'exploiter les images de haute résolution TerraSAR-X et PAZ aux collègues glaciologues (qui font également partie de l'encadrement de la thèse), afin de mesurer les déplacements sur des glaciers suspendus dans le massif du Mont Blanc.

L'observation des travaux réalisés dans la thèse de Matthias pour la surveillance de grand chantier m'a motivé à développer une nouvelle méthode InSAR multi-temporelle qui permet de prendre en compte les nouvelles images au fil de l'eau sans recommencer toute la chaîne de traitement. Pour ceci, je me suis approchée des collègues spécialisés en traitement statistique du signal et donc coencadré un stage M2 en 2018 (stage de Ségolène Martin) avec G. Ginolhac. À travers ce stage, nous avons identifié des pistes de développement et avons mis en place d'un sujet de thèse. En octobre 2020, la thèse de Viet-Hoa Vu Phan a démarré avec l'objectif de développer une méthode InSAR multi-temporelle récursive et robuste qui permettra 1) d'intégrer les nouvelles images au fil de l'eau et 2) de prendre en compte la distribution non gaussienne des données.

Publications associées :

- Yan. Y., Doin M.P., Lopez-Quiroz P., Tupin F., Fruneau B., Pinel V., Trouvé E. Mexico City subsidence measured by InSAR time series : Joint analysis using PS and SBAS approaches. IEEE Journal of Selected Topics in Applied Earth Observations and Remote Sensing, Vol. 5, No. 4, pp.1312 – 1326. 2012. DOI : 10.1109/JSTARS.2012.2191146
- M. Jauvin, Y. Yan, E. Trouvé, B. Fruneau, M. Gay, B. Girard. Integration of Corner Reflectors for the Monitoring of Mountain Glacier Areas with Sentinel-1 Time Series. Remote Sensing, MDPI, 11(8), 988, <https://doi.org/10.3390/rs11080988>

Reconstruction de données manquantes

Malgré la masse de données disponibles, le problème de données manquantes existe toujours dans les séries temporelles de mesures de déplacement, à cause des changements de la surface observée ou limite technique des méthodes utilisées pour le calcul du déplacement. En particulier, pour les objets qui décorrèlent rapidement comme les glaciers alpins, l'incomplétude de données est fréquemment présente, ce qui dégrade la fiabilité des mesures de déplacement et donc gêne l'utilisation de ce dernier dans des problèmes de modélisation. Par conséquent, le développement de méthodes avancées permettant de reconstruire les données manquantes dans des séries temporelles de mesures de déplacement semble nécessaire.

Mon début en traitement de données manquantes était durant le stage M2 de Rémi Prébet (taux d'encadrement 80%). Une série temporelle d'interférogrammes formés entre les dates d'acquisition consécutives ont été obtenus sur le glacier Gorner, courant la période hivernale 2016 - 2017. La difficulté d'une analyse directe de cette série temporelle se trouve, d'une part, sur la présence des données manquantes, i.e. des zones ou des interférogrammes entiers où la perte de cohérence est observée; et d'autre part sur le manque de la redondance des informations de déplacement dans la série temporelle à cause de la manière de former les interférogrammes. Nous avons proposé une méthode, nommée Principal Modes (PM), afin d'extraire les informations cohérentes du déplacement dans les séries temporelles des interférogrammes enroulés et déroulés en nous appuyant sur une analyse en composante principale. Ces travaux ont été publiés dans (Prébet et al.,

2019).

Dans la thèse Alexandre Hippert-Ferrer que j'ai encadrée principalement (taux d'encadrement 80%), nous avons proposé 3 méthodes pour reconstruire les données manquantes dans des séries temporelles de mesure de déplacement par télédétection (images optiques/radar, GPS). Les deux premières méthodes, nommées "Expectation Maximization - Empirical Orthogonal Functions (EM-EOF)" et "EM-EOF étendue", s'appuient respectivement sur la décomposition de la covariance temporelle et spatio-temporelle de la série temporelle de mesure de déplacement en fonctions empiriques orthogonales (EOFs) et nécessitent une initialisation des valeurs manquantes avant le traitement. La troisième méthode est orientée vers l'estimation robuste de la matrice de covariance du signal de déplacement, sans initialisation préalable des valeurs manquantes. Ces trois approches ont en commun de s'appuyer sur un schéma de résolution itératif de type espérance-maximisation (EM) ainsi que sur la sélection d'un nombre réduit de modes décrivant le maximum de variabilité du signal de déplacement. Les deux premières méthodes ont été publiées dans (Hippert-Ferrer et al., 2020a) et (Hippert-Ferrer et al., 2020b). La poursuite du développement de la troisième méthode s'est poursuivi par Alexandre Hippert-Ferrer, recruté en post-doctorant au LEME dans le cadre du projet ANR MARGARITA.

Publications associées :

- R. Prébet, Y. Yan, M. Jauvin, E. Trouvé. A Data-Adaptive EOF-Based Method for Displacement Signal Retrieval From InSAR Displacement Measurement Time Series for Decorrelating Targets. *IEEE Transactions on Geoscience and Remote Sensing*, 2019, 57(8), pp.5829-5852. <10.1109/TGRS.2019.2902719>
- A. Hippert-Ferrer, Y. Yan, P. Bolon. 2020a, EM-EOF : Gap – Filling in Incomplete SAR Displacement Time Series, *IEEE Transactions on Geosciences & Remote Sensing*, doi : 10.1109/TGRS.2020.3015087
- A. Hippert-Ferrer, Y. Yan, P. Bolon. 2020b, Spatiotemporal Filling of Missing Data in Remotely Sensed Displacement Measurement Time Series, *IEEE Geosciences & Remote Sensing Letters*, doi : 10.1109/LGRS.2020.3015149

Analyse des séries temporelles de mesures de déplacement

Avec la disponibilité régulière et gratuite des données Sentinel, des séries temporelles d'images sont disponibles pour les mesures de déplacement. De manière générale, on construit un réseau de mesure en reliant les paires d'images entre lesquelles on calcule le déplacement. De ce fait, une grande quantité de mesures de déplacements de différentes baselines temporelles, de différentes qualités (en termes d'incertitude et d'incomplétude), portant des informations redondantes ou complémentaires, sont à notre disposition. D'autre part, l'ensemble de ces mesures de déplacement ne permet pas une interprétation directe du comportement du déplacement étudié (e.g. vitesse moyenne pendant une période, variabilité saisonnière, etc.). Une étape de post-traitement est indispensable afin d'extraire les informations du déplacement de meilleure qualité et directement interprétables ou utilisables par d'autres techniques d'analyse.

Le problème de fusion des mesures de déplacement a été abordé dans ma thèse, avec l'objectif de réduire les incertitudes par la redondance dans un cadre statique (phénomène instantané, pas de série temporelle de mesure de déplacement). Des stratégies de fusion ont été proposées avec une modélisation des incertitudes présentes dans les données (Yan et al., 2012a, Yan et al., 2012b).

Dans la thèse de Laurane Charrier (taux d'encadrement 33%), le problème est nettement plus compliqué. Des mesures de déplacement issues de l'offset tracking des images Sentinel-2 de diffé-

rentes baselines temporelles et de différentes qualités sont à disposition pour étudier l'écoulement du glacier Fox. L'incomplétude, la redondance, la complémentarité et l'incertitude sont présentes dans les données. L'objectif de l'étude consiste à obtenir une série temporelle de mesures de déplacement entre les dates d'acquisition consécutives avec une qualité améliorée (incertitude et incomplétude réduite). La méthode proposée pour le traitement de ce jeu de données nécessite la prise en compte de la redondance, de l'incomplétude, de l'incertitude, ainsi que de la particularité du comportement du déplacement étudié. Pour ceci, nous sommes partis de la démarche courante, et nous nous appuyons sur le principe de la fermeture temporelle de déplacement dans un système d'inversion au sens moindre carré. Afin de prendre en compte les incertitudes, une stratégie d'inversion à 2 étapes a été adoptée : une première inversion sans pondération et les valeurs de pondération à l'étape 2 sont estimées à partir des résidus obtenus à la première étape. Étant donné l'information a priori du déplacement (vitesse varie sous forme d'un sinus), les mesures de petites baselines temporelles sont privilégiées dans l'inversion, car les mesures de grandes baselines temporelles ont tendance à favoriser une estimation d'une vitesse moyenne. Ces travaux font l'objet d'un papier en préparation.

Publications associées :

- Yan Y., Mauris G., Trouvé E., Pinel V. Fuzzy uncertainty representations of co-seismic displacement measurements issued from SAR imagery. *IEEE Transactions on Instrumentation & Measurement*, vol. 61, No. 5, pp. 1278 – 1286, 2012. DOI : 10.1109/TIM.2011.2175825.
- Yan Y., Trouvé E., Pinel V., Mauris G., Pathier E., Galichet S. Fusion of D-InSAR and subpixel image correlation measurements for coseismic displacement field estimation : Application to the Kashmir earthquake (2005). *International Journal of Image and Data Fusion*, Vol. 3, No. 1, pp.71-92, 2012. DOI :10.1080/19479832.2011.577563.

Estimation des paramètres géophysiques à partir des mesures de déplacement

Un objectif important de la mesure de déplacement consiste à prédire les risques naturels. Pour ceci, il est indispensable de comprendre la source en profondeur à l'origine du déplacement observé depuis la surface. La géométrie et la force de la source sont caractérisées par un ensemble des paramètres géométriques et physiques qui peuvent être estimés à partir des mesures de déplacement en surface, ce dernier est réalisé par inversion d'un modèle géophysique. Deux types d'inversion, statique et dynamique, existent. Dans le cas d'inversion statique, les valeurs des paramètres géophysiques à estimer n'évoluent pas, alors qu'elles varient au cours du temps dans le cas d'inversion dynamique. Les méthodes d'inversion statique (déterministe ou stochastique) ont été développées depuis très longtemps dans la communauté géophysique et ont déjà gagné beaucoup de maturité, la difficulté de leur implémentation se trouve essentiellement sur la modélisation du phénomène observé. Quant à l'inversion dynamique, très récemment l'assimilation de données a été proposée en volcanologie, ce qui ouvre une nouvelle direction de recherche dans cette communauté.

J'ai acquis la compétence en inversion statique pendant ma thèse. Dans l'étude du séisme du Pakistan en 2015, j'ai estimé les paramètres géométriques de la faille et la distribution du glissement sur le plan de la faille à partir des mesures de déplacement issues de l'InSAR et de la corrélation d'amplitude. Par rapport aux études similaires pré-existantes, j'ai réussi à proposer un modèle de faille qui explique mieux les données (Yan et al., 2013). Cette première expérience, même si c'était juste une application des outils mis à disposition, m'a permis de maîtriser la démarche d'inversion statique.

Avec deux ans de postdoc en assimilation de données en océanographie dans le cadre d'un projet Européen, j'ai pu acquérir de solide connaissance en assimilation de données (une technique permettant de combiner un modèle dynamique et les données dans le passé et au présent pour prédire l'état futur du système observé, en s'appuyant sur les statistiques des erreurs), en particulier avec le filtre de Kalman d'ensemble (Yan et al., 2014, Yan et al., 2015, Yan et al., 2017). En collaborant avec Virginie Pinel, spécialiste en modélisation volcanique, nous avons introduit la technique de l'assimilation de données pour la première fois en volcanologie dans le cadre de la thèse de Mary Grace Bato (taux d'encadrement 30%). L'objectif de cette thèse était de prédire l'évolution des surpressions dans des chambres magmatiques en utilisant des mesures de déplacement en surface issues de données InSAR et GNSS. L'ensemble des cas d'études sur données réelles et synthétiques fournissent des résultats prometteurs, renforçant l'intérêt que porte l'assimilation de données. Ces travaux ont été publiés dans (Bato et al., 2017) et (Bato et al., 2018). Cette thèse a gagné un prix de thèse en géophysique en 2019 du fait de son originalité.

Avec les avancées en réseau de neurones, je souhaite développer des nouvelles méthodes d'inversion qui permettront de combiner les réseaux de neurones convolutionnels et récurrents, et les modèles physiques afin de répondre au besoin de surveillance des risques naturels. Cette idée fait l'objet d'un workpackage de mon projet ANR soumis.

Publications associées :

- Bato M.-G., Pinel V., Yan Y., Jouanne F., Vandemeulebrouck J., Possible deep connection between volcanic systems evidenced by sequential assimilation of geodetic data, Scientific Reports, Nature Publishing Group, 2018, <https://doi.org/10.1038/s41598-018-29811-x>
- Bato M.-G., Pinel V., Yan Y., "Assimilation of Deformation Data for Eruption Forecasting : Potentiality Assessment Based on Synthetic Cases", Frontiers in Earth Science, Frontiers Media, 2017, doi : 10.3389/feart.2017.00048
- Yan Y., Barth A., Beckers J.-M., Brankart J.-M., Brasseur P., Candille G., « Comparison of different incremental analysis update schemes in a realistic assimilation system with Ensemble Kalman Filter », Ocean Modelling, 2017, 115, pp.27-41. <10.1016/j.ocemod.2017.05.002>
- Yan Y., Barth A., Beckers J.-M., Candille G., Brankart J.-M., Brasseur P., « Ensemble assimilation of ARGO temperature profile, sea surface temperature, and altimetric satellite data into an eddy permitting primitive equation model of the North Atlantic Ocean », Journal of Geophysical Research. Oceans, 2015, pp.vol. 120. <10.1002/2014JC010349>
- Yan Y., Barth A., Beckers J.M. Comparison of different assimilation schemes in a sequential Kalman filter assimilation system. Ocean Modelling, Vol. 73, pp. 123-137, 2014
- Yan Y., Pinel V., Trouvé E., Pathier E., Perrain J., Bascou P., Jouanne F. Coseismic slip distribution of the 2005 Kashmir earthquake from SAR amplitude image correlation and differential interferometry. Geophysical Journal International, Vol. 193, No. 1, pp. 29-46, 2013. DOI :10.1093/gji/ggs102

Bilan des publications

- ▷ Nombre de chapitres dans des ouvrages : 1 publié, 1 en préparation
- ▷ Nombre d'articles dans des revues à comité de lecture : 18
- ▷ Nombre de communications au niveau international avec comité de lecture : 14
- ▷ Nombre de communications au niveau national avec comité de lecture : 1

-
- ▷ Nombre de communications dans des congrès internationaux : 20
 - ▷ Nombre de communications dans des congrès nationaux : 11

Liste de publications

Revues à comité de lecture

1. A. Hippert-Ferrer, **Y. Yan**, P. Bolon. EM-EOF : Gap – Filling in Incomplete SAR Displacement Time Series, IEEE Transactions on Geosciences & Remote Sensing, doi : 10.1109/TGRS.2020.3015087
2. A. Hippert-Ferrer, **Y. Yan**, P. Bolon. Spatiotemporal Filling of Missing Data in Remotely Sensed Displacement Measurement Time Series, IEEE Geosciences & Remote Sensing Letters, doi : 10.1109/LGRS.2020.3015149
3. R. Prébet, **Y. Yan**, M. Jauvin, E. Trouvé. A Data-Adaptive EOF-Based Method for Displacement Signal Retrieval From InSAR Displacement Measurement Time Series for Decorrelating Targets. IEEE Transactions on Geoscience & Remote Sensing, 2019, 57(8), pp.5829-5852, <10.1109/TGRS.2019.2902719>
4. M. Jauvin, **Y. Yan**, E. Trouvé, B. Fruneau, M. Gay, B. Girard. Integration of Corner Reflectors for the Monitoring of Mountain Glacier Areas with Sentinel-1 Time Series. Remote Sensing, MDPI, 11(8), 988, <https://doi.org/10.3390/rs11080988>
5. R. Fallourd, A. Dehecq, M. Jauvin, **Y. Yan**, G. Vasile, et al.. Suivi des glaciers de montagne par imagerie radar satellitaire. Revue Française de Photogrammétrie et de Télédétection, Société Française de Photogrammétrie et de Télédétection, 2019, pp.91-105
6. Bato M.-G., Pinel V., **Yan Y.**, Jouanne F., Vandemeulebrouck J., Possible deep connection between volcanic systems evidenced by sequential assimilation of geodetic data, Scientific Reports, Nature Publishing Group, 2018, <https://doi.org/10.1038/s41598-018-29811-x>
7. Bato M.-G., Pinel V., **Yan Y.**, Assimilation of Deformation Data for Eruption Forecasting : Potentiality Assessment Based on Synthetic Cases, Frontiers in Earth Science, Frontiers Media, 2017, doi : 10.3389/feart.2017.00048
8. **Yan Y.**, Barth A., Beckers J.-M., Brankart J.-M., Brasseur P., Candille G., Comparison of different incremental analysis update schemes in a realistic assimilation system with Ensemble Kalman Filter, Ocean Modelling, Elsevier, 2017, 115, pp.27-41. 10.1016/j.ocemod.2017.05.002
9. Barth A., **Yan Y.**, Alvera-Azcárate A., Beckers J.-M., Local ensemble assimilation scheme with global constraints and conservation, Ocean Dynamics, Springer Verlag, 2016, 66 (12), pp. 1651-1664
10. **Yan Y.**, Dehecq A., Trouvé E., Mauris G., Gournelen N., Vernier F., Fusion of Remotely Sensed Displacement Measurements : Current status and challenges, IEEE geoscience and remote sensing magazine, IEEE, 2016, 4 (1), pp.6-25. 10.1109/MGRS.2016.2516278
11. **Yan Y.**, Barth A., Beckers J.-M., Candille G., Brankart J.-M., Brasseur P., Ensemble assimilation of ARGO temperature profile, sea surface temperature, and altimetric satellite data into an eddy permitting primitive equation model of the North Atlantic Ocean, Journal of Geophysical Research. Oceans, Wiley-Blackwell, 2015, pp.vol. 120. 10.1002/2014JC010349
12. **Yan Y.**, Barth A., Beckers J.M. Comparison of different assimilation schemes in a sequential Kalman filter assimilation system. Ocean Modelling, Vol. 73, pp. 123-137, 2014

-
13. **Yan Y.**, Pinel V., Trouvé E., Pathier E., Perrain J., Bascou P., Jouanne F. Coseismic slip distribution of the 2005 Kashmir earthquake from SAR amplitude image correlation and differential interferometry. *Geophysical Journal International*, Vol. 193, No. 1, pp. 29-46, 2013. DOI :10.1093/gji/ggs102.
 14. **Yan Y.**, Trouvé E., Pinel V., Mauris G., Pathier E., Galichet S. Fusion of D-InSAR and subpixel image correlation measurements for coseismic displacement field estimation : Application to the Kashmir earthquake (2005). *International Journal of Image and Data Fusion*, Vol. 3, No. 1, pp.71-92, 2012. DOI :10.1080/19479832.2011.577563.
 15. **Yan Y.**, Mauris G., Trouvé E., Pinel V. Fuzzy uncertainty representations of co-seismic displacement measurements issued from SAR imagery. *IEEE Transactions on Instrumentation Measurement*, vol. 61, No. 5, pp. 1278 – 1286, 2012. DOI : 10.1109/TIM.2011.2175825.
 16. **Yan. Y.**, Doin M.P., Lopez-Quiroz P., Tupin F., Fruneau B., Pinel V., Trouvé E. Mexico City subsidence measured by InSAR time series : Joint analysis using PS and SBAS approaches. *IEEE Journal of Selected Topics in Applied Earth Observations and Remote Sensing*, Vol. 5, No. 4, pp.1312 – 1326. 2012. DOI : 10.1109/JSTARS.2012.2191146
 17. Vernier, F., Fallourd R., Friedt J.M., **Yan Y.**, Trouvé E., Nicolas J.M., Moreau L. Fast Correlation Technique for Glacier Flow Monitoring by Digital Camera and Space-borne SAR Images. *EURASIP Journal on Image and Video Processing*, 2011 :11, DOI :10.1186/1687-5281-2011-11
 18. Pétillet I., Trouvé E., Bolon Ph., Julea A., **Yan Y.**, Gay M., Vanpé J.-M. Radar-Coding and Geocoding Lookup Tables for the Fusion of GIS and SAR Data in Mountain Areas. *IEEE Geoscience and Remote Sensing Letters*, Vol. 7, No. 2, pp. 309-313, 2010. Doi : 10.1109/LGRS.2009.2034118

Chapitre dans des ouvrages

1. Bato M.G., Pinel V., **Yan Y.**, Ensemble data assimilation in volcanology, *Remote Sensing Imagery*, ISTE – John Wiley Sons, to appear.
2. **Yan Y.**, Pinel V., Vernier F., Trouvé E., Displacement measurements, Florence Tupin, Jordi Inglada, Jean-Marie Nicolas Eds. *Remote Sensing Imagery*, ISTE – John Wiley Sons, pp. 251-282, 2014, Digital and image processing series, <ISBN : 978-1-84821-508-5>
3. **Yan Y.**, Pinel V., Vernier F., Trouvé E., Mesures de déplacement, Florence Tupin, Jean-Marie Nicolas, Jordi Inglada Eds. *Imagerie de télédétection*, Hermes Science – Lavoisier, pp. 269-301, 2014, *Traité IC2, série Signal et image*.

Conférences internationales avec comité de lecture

...

Encadrements

Thèses

1. Mme **Mary Grace Bato**

- Sujet de thèse : Vers une assimilation de données de déformation en volcanologie
- Financement : ministériel ordinaire
- Durée : 02/01/2015 - 02/07/2018
- Encadrement
 - Yajing Yan (LISTIC, 30 %).
 - Virginie Pinel (ISTerre, 70 %).
- Prix et distinction : le premier Accessit du Prix de thèse Géophysique décerné par le Comité National Français de Géodésie et Géophysique en 2019
- Bilan de production scientifique
 - Revues : 2
 - Conférences internationales : 5 sans acte (dont 1 invitée)
 - Colloques nationaux : 4
 - Diffusion media grâce à l'innovation de la thèse :
 - * Volcano Forecast ? New Technique Could Better Predict Eruptions, Scientific American
 - * Scientists are trying to use satellites to forecast volcanic eruptions, CNBC
 - * Think weather forecasts are bad ? Try forecasting a volcanic eruption, Popular Science
 - * Predicting eruptions using satellites and math, Eurekalert
 - * Scientists predict volcanic eruptions with satellites and GPS, CNN Tech
- Devenir de la doctorante : chercheuse post-doctorale au JPL, NASA, USA

2. M. **Matthias Jauvin**

- Sujet de thèse : Mesure des déformations de surface par imagerie radar satellitaire : Application à la surveillance des territoires de montagne et de l'impact de grands chantiers
- Financement : 50% Université Savoie Mont-Blanc, 50% Industriel
- Durée : 01/10/2015 - 18/12/2019
- Encadrement
 - Yajing Yan (LISTIC, 40 %)
 - Emmanuel Trouvé (LISTIC, 40 %)
 - Bénédicte Fruneau (MATIS-IGN, 20 %)
- Bilan de production scientifique et industrielle

-
- Revue : 1
 - Conférences internationales : 3 avec acte, 2 sans acte
 - Conférence nationale : 1
 - Création du Groupe d'Intérêt Economique (GIE) AURIGAMI
 - Devenir du doctorant : Directeur technique du GIE AURIGAMI

3. M. **Alexandre Hippert-Ferrer**

- Sujet de thèse : Reconstruction de données manquantes dans des séries temporelles de mesures de déplacement par télédétection
- Financement : Ministériel ordinaire
- Durée : 01/10/2017 - 16/10/2020
- Encadrement
 - Yajing Yan (LISTIC, 80 %).
 - Philippe Bolon (LISTIC, 20 %).
- Bilan de production scientifique
 - Revue : 2
 - Conférence internationale : 2 avec acte, 2 sans acte
 - Conférence nationale : 1 avec acte, 2 sans acte
- Devenir du doctorant : Chercheur post-doctoral au LEME, France

4. Mme **Laurane Charrier**

- Sujet de thèse : Fusion d'images de télédétection multi-capteurs/multi-temporelles pour la surveillance de glaciers et de glissements de terrain
- Financement : 50% Université Savoie Mont-Blanc, 50% ONERA
- Date de la première inscription : 01/10/2019
- Encadrement
 - Yajing Yan (LISTIC, 33 %).
 - Emmanuel Trouvé (LISTIC, 33 %).
 - Elise Koeniguer (ONERA, 33 %).
- Bilan de production scientifique
 - Conférence internationale : 1 avec acte, 1 sans acte

5. M. **Suvrat Kaushik**

- Sujet de thèse : Couverture glacio-nivale & glacier suspendu
- Financement : Ministériel ordinaire
- Date de la première inscription : 01/11/2019
- Encadrement
 - Yajing Yan (LISTIC, 25 %).
 - Emmanuel Trouvé (LISTIC, 25 %).
 - Ludovic Ravanel (EDYTEM, 25 %).
 - Florence Magnin (EDYTEM, 25 %).

6. Mme **Viet-Hoa Vu Phan**

- Sujet de thèse : Apprentissage statistique pour la surveillance de la déformation terrestre avec l'InSAR

-
- Financement : ONERA
 - Date de la première inscription : 01/10/2020
 - Encadrement
 - Yajing Yan (LISTIC, 25 %).
 - Guillaume Ginolhac (LISTIC, 25 %).
 - Frédéric Brigui (ONERA, 25 %).
 - Arnaud Breloy (LEME, 25 %).

Étudiants Master

1. M. **Rémi Prébet** (Ecole Normale Supérieure Paris-Saclay)
 - Sujet du stage : Extraction du signal de déplacement à partir d'une série temporelle d'interferogrammes Sentinel-1 dans des milieux montagneux
 - Durée : 04/04/2017 - 25/07/2017
 - Encadrement
 - Yajing Yan (LISTIC, 80%)
 - Emmanuel Trouvé (LISTIC, 20%)
 - Production scientifique :
 - Revue : 1
 - Conférence internationale : 1 avec acte
2. Mme **Ségolène Martin** (Ecole Normale Supérieure Paris-Saclay)
 - Sujet du stage : Calcul de la borne de Cramer-Rao pour l'évaluation de la performance de l'interférométrie radar en mesure de déplacement terrestre
 - Durée : 09/04/2018 - 27/07/2018
 - Encadrement
 - Yajing Yan (LISTIC, 50%)
 - Guillaume Ginolhac (LISTIC, 50%)
 - Production scientifique : préparation du sujet de thèse de Viet-Hoa Vu Phan
3. Mme **Aurélien Pourrin** (Université Grenoble - Alpes)
 - Sujet du stage : Pré-étude sur la surveillance des glissements de terrain dans la région Savoie/Haute Savoie par séries temporelles d'images radar à synthèse d'ouverture
 - Durée : 02/03/2020 - 17/07/2020
 - Encadrement
 - Yajing Yan (LISTIC, 100%)
 - Production scientifique : prestation SAGE/Conseil Départemental 73

Activités scientifiques et associatives

Présentations invitées

- **Séminaire invité 02/2021**, Présentation : *Exploitation des images SAR pour la mesure de déplacement et l'estimation des paramètres géophysiques*, Yan Y., ISTerre, Grenoble, France, 23/02/2021
- **AGU Fall Meeting 12/2018**, Présentation : *Volcanic data assimilation : Towards and beyond near real-time eruption forecasting*, Bato M.G. Pinel V. Yan Y, session "Better Living Through Volcano Geodesy : Constraints on Volcanic Hazards from Geodetic Observations and Multidisciplinary Models I", December 10-14, Washington D.C, United States.
- **IEEE International Geoscience and Remote Sensing Symposium 07/2016**, Présentation : *An overview of remotely sensed displacement measurements fusion : current status and challenges*, Yan Y., Dehecq A., Trouvé E., Mauris G., Gourmelen N., Vernier F., Session invitée : Data fusion II, July 10-15, Beijing, China.
- **GDR-ISIS Journée : Série d'images multi-temporelles à haute revisite, 10/2017**, Exposé : *Extraction d'informations de déplacement à partir de séries temporelles d'images SAR : Applications aux glaciers Alpains*, Toulouse.
- **MDIS 10/2015** ; Exposé : *Data assimilation : new perspective in displacement measurement by remote sensing*, Autrans.
- **Journée en Assimilation de données en géosciences 05/2015** ; Exposé : *De la fusion à l'assimilation de mesures de déplacement issues d'imagerie SAR : Application à des modèles de déformation terrestre*, Paris.

Animatrice de session dans des conférences

- 09/2020, Animatrice de la session "Analysis of Multitemporal Images", **IEEE International Geoscience and Remote Sensing Symposium**, Virtuel, septembre 2020.
- 07/2018, Animatrice de la session poster "SAR/InSAR Surface Evolution Analysis", **IEEE International Geoscience and Remote Sensing Symposium**, Valence, Espagne, juillet 2018.
- 10/2017, Co-animatrice de la session poster "Extraction du signal physique", **Mesure de la Déformation par Imagerie Spatiale**, Clermont-Ferrand, octobre 2017.
- 07/2015, Co-animatrice de la session orale "Inverse Problems and Data Assimilation Special Session", **International Workshop on the Analysis of Multitemporal Remote Sensing Images**, Annecy, France, Juillet 2015.
- 05/2015, Animatrice de la session orale "Modelling", The 47th Liège Colloquium, **Marine Environmental Monitoring, Modelling And Prediction**, Liège, Belgique, mai 2015.

Projets de recherche

En tant que porteur/co-porteur du projet

- Programme National de Télédétection Spatiale (n° PNTS-2019-11),
 - Sujet : Reconstruction de données manquantes dans des séries temporelles de mesures de déplacement issues d'images SAR par apprentissage statistique
 - Années : 2019 - 2020
 - Porteur : Y. Yan
 - Financement : 15000 euros
 - Consortium : LISTIC, ISTerre, IGE, LEME
- Appel à projet Université Savoie Mont-Blanc
 - Sujet : Surveillance par imagerie radar des glaciers alpins
 - Années : 2019 - 2020
 - Porteur : Y. Yan
 - Financement : 8200 euros
 - Consortium : LISTIC, ISTerre, IGE, India Institute of Technology Bombay
- Appel à projet CNES
 - Sujet : AssimSAR : Assimilation des données SAR acquises en contexte volcanique
 - Années : 2018 - 2019
 - Porteur : V. Pinel, Y. Yan
 - Financement : 22447 euros
 - Consortium : ISTerre, LISTIC
- Contrat industriel
 - Sujet : Mesure des déformations de surface par imagerie radar satellitaire
 - Années : 2015 - 2019
 - Porteur : E. Trouvé, Y. Yan
 - Financement : 60000 euros
 - Consortium : LISTIC, MATIS-IGE, MIRE SAS, ALITERE VIDERE

En tant que participant

- Projet MIAI
 - Sujet : Interférométrie satellite SAR pour l'estimation de la déformation de surface : comment apprendre la cohérence temporelle à partir de matrices de covariance complètes de séries temporelles d'images SAR ?
 - Années : 2020 - 2021
 - Porteur : S. Roisin-Giffard (ISTerre)
 - Financement : 4300 euros
 - Consortium : ISTerre, LISTIC
- Projet ANR MARGARITA
 - Sujet : Modern Adaptive Radar : Great Advances in Robust and Inference Techniques and Application
 - Années : 2018 - 2021

-
- Porteur : G. Ginolhac (LISTIC)
 - Financement : 297477 euros
 - Consortium : LISTIC, IMS, L2S, LEME
 - Projet EUMETSAT/CNES
 - Sujet : Merging Ocean Models and Observations at Mesoscale and Submesoscale (MOMOMS)
 - Années : 2016 - 2020
 - Porteur : E. Cosme (IGE)
 - Financement : 171000 euros
 - Consortium : IGE, LJK, LEGOS, IMB, IMEDEA, GHER, CLS, Mecator-Océan, LISTIC
 - Projet LEFE-GMMC
 - Sujet : Vers la prochaine génération de méthodes d'assimilation pour le contrôle de la circulation et des traceurs dans les systèmes d'océanographie opérationnelles
 - Années : 2014 - 2016
 - Porteur : P. Brasseur (IGE)
 - Financement : 23000 euros
 - Consortium : IGE, LJK, LISTIC, LOV

Activités administratives

Responsabilité en enseignement

- Responsable semestre 7 de la spécialité IAI du Polytech Annecy-Chambéry (06/2018 - aujourd'hui)
- Responsable année 4 de la spécialité IAI du Polytech Annecy-Chambéry (09/2020 - aujourd'hui)
- Responsable du thème "Imagerie Dronoportée et Télédétection" en enseignement innovant "Apprentissage par Problème et par Projet" (09/2016 – 07/2019)

Responsabilité administrative

- Membre du comité consultatif CNU 61 de l'Université Savoie Mont-Blanc (2016 – aujourd'hui)
- Membre du comité de sélection 4281/261 MCF 61 LISTIC/Polytech Annecy-Chambéry, 2020

Responsabilité éditoriale

- Editrice associée d'un numéro spécial du journal "Ocean Dynamics" (09/2015 – 02/2017)
- Editrice du livre "Inversion & Assimilation de données" (2019 - aujourd'hui)

Responsabilité en comité de conférences

- Membre dans le comité du programme technique de la session "Multitemporal analysis" de la conférence internationale "IGARSS 2021" (12/07/2021 - 16/07/2021)
- Membre dans le comité d'organisation de la conférence internationale "Multitemp 2015" (22/07/2015 – 24/07/2015)
- Membre dans le comité d'organisation de la conférence internationale "The 47th international Liège Colloquium" (04/05/2015 – 08/05/2015)

Deuxième partie

Research work

Introduction

My research activities have been developed around SAR (Synthetic Aperture Radar) imagery, but cover a broad spectrum of subjects starting from the exploitation of SAR images for displacement measurement until the estimation and prediction of geophysical parameters which characterize the subsurface geological structures that induce the displacement observed at the Earth's surface. I'm interested in both methodological developments, especially those to better exploit the mass of available SAR data, and geophysical applications such as earthquakes, volcanoes, subsidence in urban areas and Alpine glaciers.

With an initial formation in geophysics and geology, I decided to do a Master in remote sensing, thinking that remote sensing would be the future of geophysics. My Master thesis entitled "Calculation of the subsidence of Mexico City by differential interferometry" opened the door of SAR interferometry for me. My Ph.D thesis thus continued in this community with applications to seismic and volcanic modeling. Besides InSAR, I also took data fusion and geophysical model inversion in hand during my Ph.D thesis. The perspective of my Ph.D thesis was to do data fusion in a dynamical context, thus to do data assimilation. As a fresh person, I was sufficiently lucky to be selected as a post-doc researcher in an European project. My supervisor told me later that I was chosen among other candidates with experience, because I'm a honest person ... (not for science). Later, I spent two years in the domain of data assimilation for oceanic applications. Until now, I am not able to interpret complex oceanic phenomena (even though 3 articles have been published in *Ocean Modelling* and *Journal of Geophysical Research*), but I succeeded in getting skills in Ensemble Kalman Filter, a commonly used operational data assimilation technique in real time weather forecasting. Since taking up my actual Associate Professor position at LISTIC in September 2014, I came back to the InSAR community. Obviously, at that moment, my knowledge about InSAR was out of date due to the more than two years spent on data assimilation. Therefore, during the first three years of my Associate Professor career, on one hand, I finished my works related to my post-doc research (I was involved in another data assimilation project since September 2014 following the invitation of a previous European project partner with whom I collaborated during my post-doc research); on the other hand, I read a lot of papers about the development of multi-temporal InSAR approaches that I missed. At the same time, I co-supervised the Ph.D thesis of Mary Grace Bato (01/2015-07/2018), in which data assimilation has been introduced for the first time to volcanology and its potential in real time forecasting of volcanic eruptions has been highlighted; and the Ph.D thesis of Matthias Jauvin (10/2015-12/2019), in which InSAR techniques, in particular the Permanent Scatterer interferometry, have been deployed for operational urban infrastructure monitoring and for Alpine glaciers tracking. In 2017, I supervised the Master 1st year internship of Rémi Prébet (04/2017 - 07/2017), in which a namely Principal Mode method has been proposed to extract displacement information from SAR interferogram time series for decorrelating targets. From October 2017, I supervised primarily the Ph.D thesis of Alexandre Hippert-Ferrer (10/2017-10/2020) which constitutes a pioneering work that deals with missing data issues in remote sensing displacement time series by statistical learning. In 2018, I co-supervised the Master 1st year internship of Ségolène Martin (04/2018 - 07/2018) with my colleague Guillaume Ginolhac specializing in statistical signal processing. A preparation to develop a new robust and recursive multi-temporal InSAR approach, combining skills in InSAR and robust

covariance estimation, has been carried out in this internship. The Ph.D thesis of Viet-Hoa Vu Phan for further development of this subject has been started in October 2020. Since 2019, I also co-supervise the Ph.D thesis of Laurane Charrier (10/2019 - today) who works on displacement time series analysis and interpretation and the Ph.D thesis of Suvrat Kaushik (11/2019 - today) who works on hanging glacier monitoring with high resolution SAR images.

After the aforementioned data assimilation project (2014-2016), I was also solicited for the EUMETSAT/CNES project (2016-2020) and the international Dragon-4 project (2016-2020), but my involvement in these two projects was very limited. In 2018, the two-year project AssimSAR related to the Ph.D thesis of Mary Grace Bato was funded by CNES. At the same time, I tried three times an Auvergne-Rhône-Alpes region funded project on the subject of operational monitoring of displacement by SAR images, but without success. In 2019, two two-year projects coordinated by myself and funded by Université Savoie Mont-Blanc (USMB) and national program of spatial remote sensing (PNTS) respectively, related to the Ph.D thesis of Alexandre, were accepted. The PNTS funded project was more focused on methodological development for missing data imputation, while the USMB project was more focused on applications to the Alpine glacier monitoring. Since 2019, I began to prepare an ANR young researcher project, "recursive estimation and prediction of Earth deformation from SAR image time series", with the objective to promote methodological development for operational monitoring of displacement and natural hazards prediction by means of both statistical learning and deep learning.

I take the opportunity of this report to summarize my past and ongoing research works, as well as related state-of-the-art works around my research activities. I will also talk about the future works that I want to develop in the coming years, that is, towards operational monitoring of Earth deformation and prediction of natural hazards.

This report is organised into 4 chapters according to main directions of my research activities. In Chapter 1, I focus on InSAR techniques, in particular multi-temporal InSAR approaches, for displacement measurement from SAR images. After a quick introduction of SAR images and the two traditional techniques used for displacement measurement, i.e. InSAR and offset tracking, I provide a summary of the actually firmly established state-of-the-art multi-temporal InSAR approaches. This chapter ends up with the presentation of my future work, i.e. development of a new recursive and robust multi-temporal InSAR approach. In Chapter 2, I present the missing data problem in SAR/optical displacement time series and missing data imputation techniques proposed in the Ph.D thesis of Alexandre Hippert-Ferrer that I mainly supervised. These methods are based on the analysis of the temporal and spatio-temporal covariance of SAR/optical displacement time series in an Expectation-Maximization (EM) scheme. Both the technical details of the proposed methods and the results obtained in the Ph.D thesis of Alexandre will be demonstrated. I will end this chapter with further development of these methods towards parametric methods focused on the robust estimation of the covariance of SAR/optical displacement time series. Chapter 3 is dedicated to the fusion and exploitation of SAR/optical displacement time series. The main scientific problem to resolve consists of estimating a reliable and easily interpretable displacement time series from displacement networks with redundancy, uncertainty and incompleteness. State-of-the-art approaches are mainly discussed. Ideas of the Ph.D thesis of Laurane Charrier that I co-supervise actually will also be mentioned. Because this is an ongoing Ph.D thesis, I prefer not to show results that have not yet been published. In Chapter 4, I talk about the estimation and prediction of geophysical parameters related to natural hazards. Both classical model driven inversion and data assimilation techniques will be presented. The works performed in the Ph.D thesis of Mary Grace Bato will be showcased. This chapter ends up with my future works, i.e. geophysical parameter estimation and prediction by means of neural networks.

This report is written in English in order that some parts of this report can be useful for ongoing and future English speaking Ph.D students.

Measure displacement from SAR images

1.1 Introduction

Nowadays, SAR images constitute the principal source of information for displacement measurements at the Earth's surface, thanks to the high spatial coverage, all-day all-time functionality and regular availability. Interferometric SAR (InSAR), one of the most important techniques in SAR imagery, has been deployed for displacement measurement and Digital Elevation Model (DEM) generation since more than two decades. This technique can be considered as a great revolution compared to conventional geodetic approaches, since it is the only tool capable of providing displacement measurement with sub-centimeter accuracy over large areas. Enhanced performances have further been achieved by advanced multi-temporal InSAR methods, such as Small BAseline Subset (Berardino et al. (2002), Doin et al. (2011), Lanari et al. (2004), Usai (2003)), Permanent Scatterer Interferometry (Ferretti et al. (2001), Hooper et al. (2007), Kampes (2006)), SqueeSAR (Ferretti et al. (2011)), CAESAR (Fornaro et al. (2015)), phase linking with maximum likelihood estimator (Guarnieri and Tebaldini (2008)), Multi-link InSAR (Pinel-Puysségur et al. (2012)), Least square estimator (Samiei-Esfahany et al. (2016)), EMI (Ansari et al. (2018)), etc. These methods have been extensively developed and implemented in the past twenties of years, thanks to which, long term monitoring of displacement evolution becomes possible and the accuracy of the displacement velocity estimation has been revolutionized to millimeters per year, for example, on the order of 1 mm/yr based on a time series with more than 60 SAR images. Actually, with the systematic acquisition and free access of Sentinel 1 A/B images every 6 days over Europe and every 12 days elsewhere, the time series of SAR images has particularly become an unprecedented living subject. Multi-annual analysis of displacement constitutes the subject of numerous studies of landslide, subsidence, volcano deformation, glacier flows, etc.

Recent methodological development in multi-temporal InSAR has, however, seen a slowdown. More efforts have been made to build regional or national monitoring systems to be able to process SAR images at large scales and to develop automatic online processing services to facilitate the utilization of the actually existing approaches by non-experts. This is mainly because the actual existing multi-temporal InSAR approaches have already been capable of meeting the need of displacement measurement with sufficient satisfaction. On the other hand, the exploitation of InSAR techniques in operational contexts such as civil engineering monitoring and natural hazard alert, begins to emerge, but the progress is especially limited by the difficulty in integrating gradually new images that arrive over time in a more or less complex processing chain. Most actual multi-temporal InSAR approaches are retrospective analysis approaches. They have rather

been used for backward-looking analyses than for real time analyses or for prediction purpose. An integration of new SAR images into most multi-temporal InSAR processing chains implies a restart of the whole or at least a significant part of the processing chain, which can be computationally overwhelming, thus not suitable for the operational context where timely delivery of products is of particular importance. Therefore, further development of multi-temporal InSAR approaches towards operational use seems necessary and meaningful. It will significantly contribute to the near real time monitoring of anthropogenic and natural hazards.

In the following, the conventional 2-pass InSAR and offset tracking techniques for displacement estimation are presented after the quick introduction of SAR images. Then, more focus will be given to actually firmly established state-of-the-art multi-temporal InSAR approaches. The chapter ends up with my research perspective towards operational development of multi-temporal InSAR approaches.

1.2 SAR images in displacement measurement

A Single Look Complex (SLC) SAR image, z , is composed of pixels each containing a bi-dimensional complex signal, characterized by an amplitude, A , and a phase, ϕ (equation 1.1). The amplitude measures the backscattering strength of the target on the ground and depends on the properties such as soil moisture, terrain slope, etc. The phase contains geometrical information related to the distance between the sensor and the target, as well as information related to the backscattering property of the target.

$$z = Ae^{j\phi} \quad (1.1)$$

The displacement information can be obtained by comparing two SAR images acquired at two different dates and co-registered to the same geometry, namely the reference image and the secondary image respectively in this report. Two principle methods, differential interferometry SAR (also called D-InSAR) and offset tracking, deploying the phase and the amplitude of SAR images respectively, have been developed and extensively used since the 1990s.

1.2.1 Differential inteferometry SAR

The conventional 2-pass D-InSAR deploys the phase difference, sensitive to distance variation in the line of sight (LOS) direction of SAR image acquisition, between the reference and the secondary images, by computing the interferogram. The interferogram obtained from equation 1.2 is also composed of bi-dimensional complex signals, with its amplitude called the coherence and its phase called the interferometric phase.

$$\gamma e^{j\phi}(i, j) = \frac{\sum_{i, j \in \Omega} z_1(i, j) z_2^*(i, j)}{\sqrt{\sum_{i, j \in \Omega} z_1(i, j) z_1^*(i, j) \sum_{i, j \in \Omega} z_2(i, j) z_2^*(i, j)}} \quad (1.2)$$

where γ denotes the coherence, ϕ is the interferometric phase (with $\phi = \phi_1 - \phi_2$). Ω denotes the multi-looking window, a spatial neighborhood around the pixel (i, j) . In the conventional D-InSAR, a complex multi-looking (i.e. simple complex average) is often performed during the computation of the interferogram in order to reduce decorrelation noise at the expense of the spatial resolution. In case of a single look interferogram, Ω is reduced to the pixel (i, j) .

The coherence varies between 0 and 1 and indicates the similarity between the reference image and the secondary image. It is a measure of the quality of the interferometric phase. A high coherence indicates a reliable interferometric phase. The interferometric phase appears as fringe patterns on the interferogram and is sensitive to the topography and the displacement along the

LOS direction. Moreover, orbital component (due to the orbit shift between two acquisitions), atmospheric component (due to differences in the refractivity of the atmosphere between image acquisitions caused by variations in concentrations of water vapor and hydrostatic pressure) and noise component (due to various geometrical and temporal decorrelation noise) also contribute to the interferometric phase (equation 1.3).

$$\phi = \phi_{orb} + \phi_{topo} + \phi_{def} + \phi_{atm} + \phi_{noise} \quad (1.3)$$

The main processing of D-InSAR consists of separating the component related to displacement from other components. The orbital and topographic components can be removed by using auxiliary orbit data and a DEM (ideally of the same resolution as that of the interferogram). The interferogram with the orbital and topographic components removed is called the differential interferogram.

The interferometric phase is known modulo 2π , called wrapped phase, due to the round trip of the radar wave. One of the important but challenging processing step, namely phase unwrapping, thus consists of retrieving the absolute phase (i.e. unwrapped phase) from the wrapped phase. The success of phase unwrapping determines the applicability of the D-InSAR technique to the phenomenon under consideration. Coherence loss constitutes the major source of phase unwrapping failure. Phase unwrapping is performed on differential interferograms. Lots of phase unwrapping methods, including local propagation method (Chen and Zebker (2002), Goldstein and Werner (1998)), global optimization method (Yan et al. (2013)), deep learning method (Sica et al. (2021), Zhou et al. (2020)), etc., can be found in the literature. The choice of the appropriate method depends on the data quality and the user knowledge. No method always outperforms the others.

The unwrapped phase of the differential interferogram is composed of the displacement phase, the atmospheric phase and the phase term related to noise. The phase term related to noise is mainly reduced by spatial and/or temporal filtering. The separation of the atmospheric phase from the displacement signal constitutes another major challenging step in the interferometric processing. The atmospheric phase is a combination of ionospheric and tropospheric signals. The ionospheric signal depends on the radar wavelength and is less pronounced in C-band than in L-band. The tropospheric signal includes a stratified component and a turbulent component. When the atmosphere is stratified, changes to water vapor concentration are correlated with topography and can mask displacement signals with similar or lower magnitude. When turbulent mixing is dominant, atmospheric phase is spatially correlated on the scale of tens of kilometers (Doin et al. (2009), Ebmeier (2016)). Classical methods include 1) using GPS data or multi-spectral satellite data 2) meteorological model to simulate the atmospheric phase and 3) simply assuming a linear or nonlinear dependence of the (stratified) atmospheric phase on the topography (Doin et al. (2009)). Recent advances propose to use Independent Component Analysis (ICA) to separate displacement signal from atmospheric perturbations (Ebmeier (2016), Gaddes et al. (2018, 2019), Maubant et al. (2020)). Due to the chaotic characteristics of the atmospheric phase, the efficiency of the atmospheric correction is in fact case dependent.

D-InSAR provides displacement measurement with high accuracy (on the order of centimeters or sub-centimeters), but is particularly efficient for small displacement (i.e. several multiples of the wavelength of the radar signal). In case of large displacement, on one hand, coherence loss occurs. On the other hand, narrow fringe patterns increase the difficulty in phase unwrapping.

1.2.2 Offset Tracking

Offset tracking is based on the cross correlation of amplitude between the reference image and the secondary image. By defining a sliding window centered on the considered pixel on the reference image, we search for the most similar window on the secondary image, and the similarity is quantified by the cross correlation value. The relative position of the two windows gives the bi-dimensional (range and azimuth directions related to the acquisition of SAR images used) displacement information. Further interpolation needs to be performed in order to obtain a

sub-pixel estimation of the displacement. For technique details, please refer to (Fallourd (2012), Vernier et al. (2011)).

The accuracy of the displacement measurement provided by offset tracking depends on the spatial resolution of the SAR amplitude images used. In general, it can reach $1/10$ pixel. In case of time series with careful processing, an accuracy of $1/30$ pixel has been reported in Casu et al. (2011). This technique is only efficient for large displacement (e.g. on the order of meters), due to its limited accuracy. Offset-tracking is used as a complementary tool to D-InSAR in a number of studies in order to provide a complete displacement field (e.g. Yan et al. (2013)). Notice also that offset tracking is not dedicated to SAR images, it can also be applied to other images such as optical satellite images and digital camera photos.

1.3 Recent advances in multi-temporal InSAR

The development of multi-temporal InSAR approaches has been based on how the signal decorrelation can be accounted for. For this, analyses of backscattering properties of SAR images are essential. Within a resolution cell of a SAR image, the signal is the coherent sum of returns from many scatterers on the ground. If these scatters move relative to each other over time, e.g. with the presence of vegetation, the backscattering signal varies randomly, which induces the temporal decorrelation. From a spatial point of view, if the scatters within a resolution cell are observed with even slightly different incidence angles, which results of a change of the relative positions among them, the spatial decorrelation occurs. The signal decorrelation in a resolution cell is thus complex and depends on the relative behaviors of individual scatterers. In the literature, we distinguish two kinds of scatterers : Permanent Scatterer (PS) and Distributed Scatterer (DS) (Figure 1.1). In case of PS, the resolution cell is dominated by one stable scatter that is brighter than the background scatterers. In such a pixel, the variance in the phase of the backscattering signal due to the relative movement of the background scatterers is much reduced. The pixel thus appears coherent over time, subject to neither temporal nor spatial decorrelation. In the case of DS, a large number of scatters contribute more or less equally to the backscattering signal in a pixel. This pixel is subject to temporal and/or spatial decorrelation. In practice, many neighboring pixels share similar backscattering signals, as they belong to the same object.

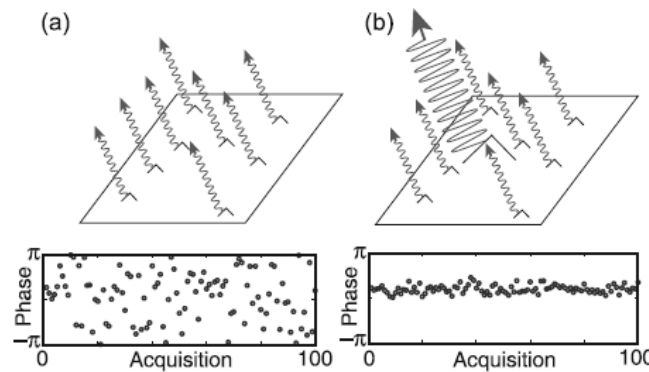


Figure 1.1 – Illustration of different behaviors of (a) DS and (b) PS (Hooper et al. (2007)).

Actual state-of-the-art multi-temporal InSAR approaches rely on

1. processing with point-wise time coherent permanent scatterers, namely Permanent Scatterer Interferometry (PSI), (e.g. Ferretti et al. (2001), Hooper et al. (2007), Kampes (2006))

2. construction of redundant multi-looked interferograms networks in Distributed Scatterer Interferometry (DSI) (e.g. Small BASeline Subset (e.g. Berardino et al. (2002), Doin et al. (2011), Lanari et al. (2004), Usai (2003)), Phase Linking or Phase Triangulation methods (e.g. Ansari et al. (2018), Guarnieri and Tebaldini (2008)), Multi-link method (Pinel-Puysségur et al. (2012)), Integer Least-Square method (Samiei-Esfahany et al. (2016)), etc.)
3. combination of PSI and DSI (e.g. squeeSAR Ferretti et al. (2011)).

Depending on the way to account for the decorrelation, the fundamental idea of multi-temporal InSAR approaches is to construct interferometric networks from a SAR image time series and to estimate a set of consistent single reference wrapped or unwrapped interferometric phase. Figure 1.2 presents several common interferometric networks.

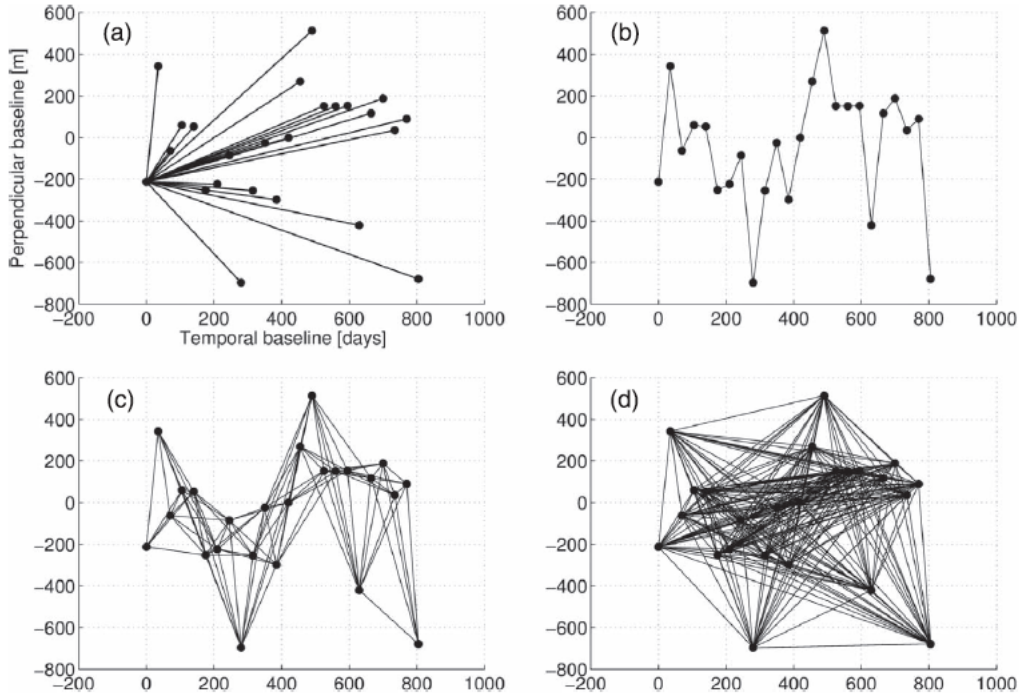


Figure 1.2 – Illustration of several common interferometric networks used in multi-temporal InSAR approaches. a) single reference b) auto-regressive b) small baselines d) all combination. (Samiei-Esfahany et al. (2016))

The single reference (SR) network, i.e. interferograms are formed between a common reference SAR image and other images in the time series, is widely adopted in PSI. Despite the simplicity of this interferometric network (i.e. without redundancy), it is sufficient to obtain reliable phase estimation, thanks to the high coherence of PS points. The auto-regressive (AR) network is most used for decorrelating targets for which coherence loss is observed on interferograms of longer time span and interferograms can only be constructed between consecutive acquisitions. The small baseline network and the all combination network are two widely used networks in DSI. In both cases, the constructed interferometric networks are redundant. The redundancy is used to retrieve the phase consistency at the level of unwrapped interferograms in case of the small baseline network (i.e. SBAS approach) and at the level of wrapped interferograms in case of the all combination network (i.e. phase linking approaches).

The phase consistency is explained as follows : assume that z_m , z_n and z_o are three coregistered SLC images, we can obtain three single-look interferograms (without multi-looking), I_{mn} , I_{om} and I_{on} , from any two of them. It can be shown that the phase of any of these interferograms can

be obtained from the other two (equation 1.4). This is called the phase consistency.

$$\phi_{mn} = \phi_{om} - \phi_{on} \quad (1.4)$$

This condition is always hold for single look pixels (e.g. PS), but not necessarily valid for multi-looked (spatially averaged) interferometric pixels (e.g. DS). All DS-based multi-temporal InSAR approaches perform phase consistency restoration to filter the wrapped or unwrapped interferograms in order to be able to estimate a set of consistent single reference interferometric phase.

1.3.1 Permanent Scatterer Interferometry

Permanent Scatterer Interferometry (PSI) distinguishes itself from other multi-temporal InSAR approaches by the use of point-wise long term coherent permanent scatterers. The network of interferograms is generated with respect to a common reference image (i.e. the SR network in Figure 1.2 (a)), without limitations in temporal or spatial baselines of SAR image pairs. Notice that, in PSI, there is no need to compute the full coherence matrix that will provide the same phase information as a SR interferometric network (i.e. only $N - 1$ useful phase values in case of N SAR images), the rank of the full coherence matrix being 1.

Given a SLC SAR image stack (already coregistered to a common reference image), PS candidates are selected based on their backscattering properties. In general, they should exhibit high phase stability over the whole time period of observation and are typically characterized by high reflectivity values (e.g. generated by dihedral reflection or simple single-bounce scattering). Two criteria are thus considered for the selection of PS candidates : temporal phase stability and amplitude brightness. For the former, the statistic of amplitude can be used as a proxy for the phase stability (Ferretti et al. (2001)), and the amplitude dispersion index is often used to describe the temporal phase variability (equation 1.5). For the latter, the average amplitude of the pixel under consideration is compared to the average amplitude of all the pixels (equation 1.6).

$$D_a = \frac{\sigma_a}{\bar{a}} \leq \lambda_1 \quad (1.5)$$

$$\bar{a} \geq \lambda_2 \bar{A} \quad (1.6)$$

where D_a is the amplitude dispersion index, \bar{a} is the average amplitude and σ_a is the amplitude standard deviation of the pixel under consideration, \bar{A} is the average amplitude of all pixels. λ_1 and λ_2 , two threshold values, do not have nominal values and are mainly determined based on the trade-off between the PS points density and the phase quality provided by the selected PS points. For example, 0.58 and 1.2 were given to λ_1 and λ_2 respectively in Yan et al. (2012a).

For each selected PS point, the single look interferogram is computed as in equation 1.2 with the multi-looking window reduced to one pixel. In this way, the PS approaches work on full resolution SAR images. The advantages are two folds, 1) the phase consistency is naturally retained and 2) point like information will not be lost by the spatial average as performed in most DS approaches. Same as in the conventional 2-pass D-InSAR approach, the interferometric phase of each PS point includes several contributions (equation 1.3) and differential interferogram is computed by removing orbital and topographic components using auxiliary orbit data and a DEM. Notice that, because of the inaccuracy of the orbit data and the DEM error, it is possible that residual orbital and topographic phases remain in the phase of the differential interferogram.

PS approaches generally propose a 2-dimensional phase model and adopt a local processing strategy (i.e. propagation through nearby pixels). The residual topographic phase (related to the DEM error) and the displacement phase (related to the linear displacement velocity) are mainly taken into account in the phase model (equation 1.7). The rational to take the residual topographic phase rather than atmospheric phase or residual orbital phase into account lies in the fact that, on one

hand, for nearby pixels, the atmospheric phase and the residual orbital phase can be considered very similar; on the other hand, in PSI, interferograms can be formed with large perpendicular baselines (i.e. distance between the orbits of two acquisitions) regardless of the spatial decorrelation. Since the residual topographic phase is proportional to the perpendicular baseline, its contribution can thus be large in the interferometric phase.

$$\phi^m = \frac{4\pi}{\lambda} \frac{B_{\perp}}{R \sin \theta} h + \frac{4\pi}{\lambda} v T \quad (1.7)$$

where λ is the wavelength of the radar signal, B_{\perp} is the perpendicular baseline, θ is the incidence angle, h is the DEM error, T is the temporal baseline, v is the linear displacement velocity.

In the phase model shown in equation 1.7, the linear displacement velocity, v , and the DEM error, h , constitute two major parameters to estimate. They can be obtained by minimising the difference between the phase model and the measured phase, with the constraint that the phase is modulo 2π . For this, a temporal phase unwrapping strategy is adopted and a local (inside a small patch) 2D regression in the space of (B_{\perp}, T) between nearby PS points is performed. The temporal phase unwrapping is possible because the phase consistency condition is met. The solution is obtained by maximising the temporal coherence defined as in equation 1.8.

$$\gamma = \frac{1}{N} \sum_{k=1}^N e^{j(\phi_k^m - \phi_k)} \quad (1.8)$$

with N the number of SAR images, ϕ^m modeled wrapped phase, ϕ measured wrapped phase.

The local 2D regression leads to relative DEM error and displacement rate, $(\delta h, \delta v)$, across arcs linking PS points. The relative DEM error and displacement rate are integrated through space, i.e. connecting each point to others in a propagating way, to get a global solution (h, v) .

The residual of the 2D regression corresponds to phase terms not considered in the phase model, including residual orbital trend, atmospheric delay and nonlinear motion, etc. A 2D regression performed on the residual (or the residual plus the temporally unwrapped phase) allows further refinement of the estimation. An iterative procedure leads to a more accurate solution. At each iteration, the phase standard deviation of the 2D regression can be used as an assessment of the quality of the obtained $(\delta h, \delta v)$. A thresholding on the phase standard deviation is performed to reject PS candidates that do not provide reliable phase information. Thus, more and more fake PS candidates are removed during the iteration.

The final products of PS approaches include a linear displacement velocity estimation, a DEM error estimation and a SR phase time series over reliable PS points. Nonlinear motion is not considered in the phase model, this part of displacement is filtered to the residual phase after the 2D regression. According to (Yan et al. (2012a)), the phase standard deviation is strongly related to the presence of nonlinear motion. Large phase standard deviation is observed over areas where nonlinear motion presents. It is thus necessary to check the phase standard deviation and the residual phase to retrieve the nonlinear motion. Note also that, a priori displacement information (e.g. from previous surveys) can help better define the searching space of (B_{\perp}, T) , which potentially improves the efficiency of the PS approaches.

PS approaches have the capability to provide point-wise displacement measurements of high accuracy. With an accurate localisation of PS points, PS approaches present great interest for urban infrastructure monitoring where we see their widespread applications. Figure 1.3 presents the linear displacement velocity map and the DEM error correction between November 2002 and March 2007 obtained from PSI over the Mexico city (Yan et al. (2012a)). The interest of PSI in providing displacement information on individual targets on the ground has been highlighted in Yan et al. (2012a) : the point like displacement information is essential to quantify the relative importance of surface loads, surface drying and drying due to underground water over-exploitation in the subsoil compaction.

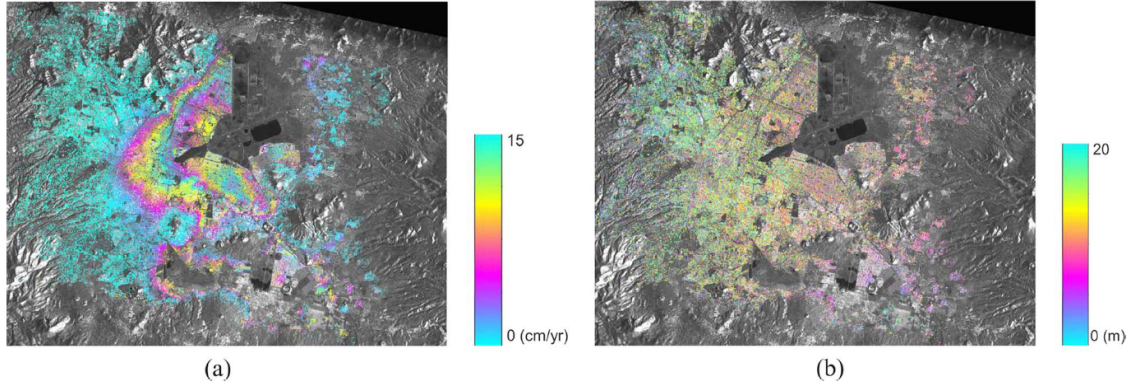


Figure 1.3 – (a) Linear displacement velocity (a color cycle represents 15 cm/yr) (b) elevation correction (a color cycle represents 20 m) over the Mexico city during the period between November 2002 and March 2007 obtained from PSI applied to 38 ENVISAT images (Yan et al. (2012a)).

Despite the success of PSI, their applications are mainly limited by the PS points density, particularly over natural areas where few man-made structures exist, only tree trunks, single large rocks or facet amongst the vegetation can be considered as PS points. Installation of corner reflectors networks in natural areas can help the implementation of PSI. In Jauvin et al. (2019), ad hoc PSI processing has been performed successfully over the moraine of the Argentière glacier (Figure 1.4), with the help of a small corner reflectors network. However, note that the accuracy of the phase estimation in this case is not comparable with that obtained from a dense PS points network.

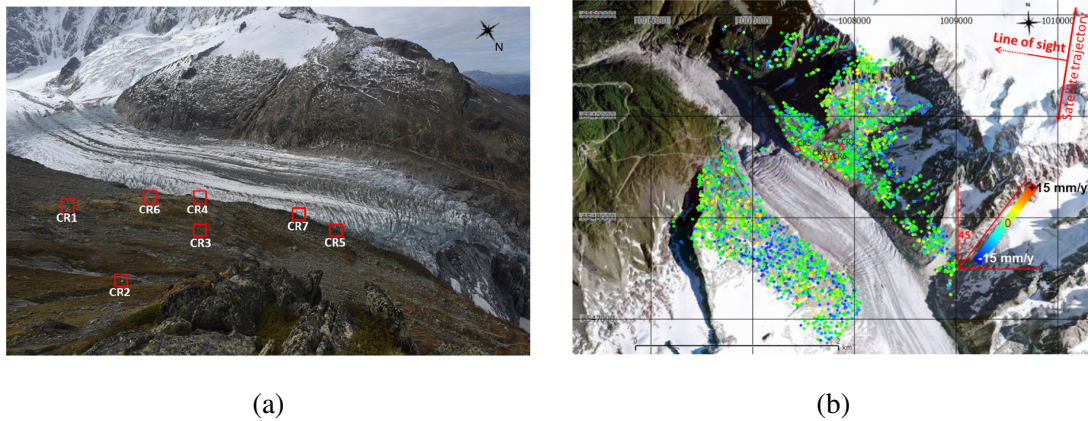


Figure 1.4 – (a) Corner reflectors network (b) linear velocity over the period between 01/08/2017 and 30/10/2018 obtained from 27 Sentinel-1 images over the moraine of the Argentière glacier (Jauvin et al. (2019)).

1.3.2 Small Baseline Subset

The Small Baseline Subset (SBAS) approach (Berardino et al. (2002), Doin et al. (2011), Lanari et al. (2004), Usai (2003)) increases the spatial coverage over which we extract reliable phase time series, especially outside urban areas, by working on distributed targets. To maximize the coherence, interferograms are computed only for SAR image pairs separated by small temporal and spatial baselines (Figure 1.2 (c)). Multi-looked interferograms are computed in the same way as in the 2-pass D-InSAR (equation 1.2). Adaptive filtering using the Goldstein filter is carried out on interferograms to further reduce decorrelation noise. Spatial phase unwrapping is performed on each individual filtered interferogram. Atmospheric phase and other residual terms (e.g. residual orbital contribution) that appears as a ramp on interferograms are jointly estimated by linear

adjustment to the unwrapped phase outside the deformation area. Afterwards, a singular value decomposition (SVD) inversion allows an examination of the phase consistency of the redundant unwrapped interferometric network (including both the phase inconsistency introduced by spatial average and phase unwrapping errors on individual interferograms) and an estimation of a SR displacement time series. The SVD is especially useful when the used SAR image time series breaks into several disjoint subsets or at least one critical link in the interferometric network is missing, as linking separate subsets is an ill-posed problem. An alternative solution to SVD consists of a linear or nonlinear interpolation of the phase between separate subsets. This is realized by adding a constraint, stating for example that the phase varies linearly or as a quadratic polynomial in time and linearly with the perpendicular baseline, to the design matrix of the inverse problem with an appropriate weight (often a small weight).

In the SBAS variant proposed in (Doin et al. (2011), Lopez-Quiroz et al. (2009)), a deformation model is estimated from a stack of properly unwrapped interferograms of high signal-to-noise ratio. Residual interferograms are obtained by subtracting the deformation model from the wrapped interferograms. Then, phase unwrapping is only performed on residual interferograms, which makes it possible to avoid phase unwrapping errors as much as possible. This procedure is repeated in an iterative way until the temporal misclosure error (i.e. root mean square error between the observed phase and the one reconstructed from inverted phases) after the SVD inversion drops to a predefined threshold.

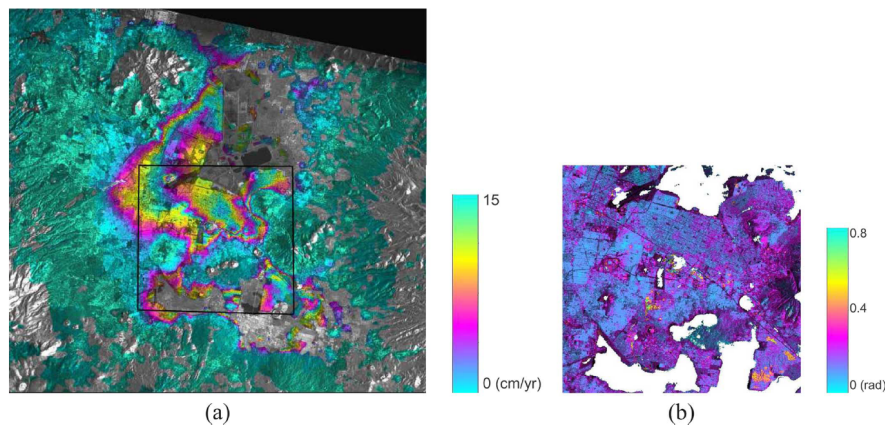


Figure 1.5 – (a) Linear displacement velocity over the Mexico city during the period between November 2002 and March 2017 obtained from the SBAS approach proposed in Doin et al. (2011), Lopez-Quiroz et al. (2009). A color cycle represents 15 cm/yr. (b) zoom on the temporal misclosure error in the area located by the black rectangle in (a). Larger errors correspond to localized phase unwrapping errors. (Yan et al. (2012a)).

Figure 1.5 presents the linear velocity map obtained from the SBAS approach proposed in Doin et al. (2011), Lopez-Quiroz et al. (2009) over the Mexico city with the same data sets as in Figure 1.3. Consistent displacement patterns and velocity amplitude are observed. The SBAS approach provides measurements over areas where no PS points are identified. However, the SBAS velocity map is regularized in space, thus cannot give accurate velocity estimation over individual points that behave differently from its neighbors. Therefore, PS and SBAS approaches have been used jointly to measure the Mexico city subsidence at different scales in (Yan et al. (2012a)).

The SBAS approach constitutes one of the most important early multi-temporal InSAR approaches. Several variants have been developed by different research groups (Berardino et al. (2002), Doin et al. (2011), Lanari et al. (2004), Usai (2003)). The efficiency of these approaches has been proven in numerous applications. However, a recent study of systematic bias in displacement measurement by multi-temporal InSAR approaches indicates that the SBAS approach is more error-prone compared to approaches that use the full coherence matrix of a SAR images time series (Ansari et al. (2021)). They found that the multi-looked interferograms reveal a systematic

signal which cannot be explained by the topographic or atmospheric variations and interfere in the accurate estimation of the displacement. Such signals are short-lived and decay with the temporal baseline. Therefore, phase bias is larger using only short temporal baseline interferograms. The propagation of phase bias in long time series compromises the accuracy of displacement velocity from an achievable sub-millimetric to centimetric per year level.

1.3.3 Phase linking approaches

Phase linking or phase triangulation approaches exploit the full covariance/coherence of SAR images time series. The wrapped interferometric network is constructed according to the all-combination strategy (Figure 1.2 (d)). The redundancy of the wrapped interferometric network is used to retrieve the phase consistency lost due to spatial averaging. The main objective is to use all the $N \times (N - 1)/2$ interferograms generated from a time series of N SAR images to yield the best estimate of $N - 1$ single reference wrapped phase difference. These approaches solve a nonlinear estimation problem either by iterative algorithms or by eigendecomposition of the full coherence/covariance matrix of the SAR images time series.

Maximum likelihood estimator

The maximum likelihood estimator (MLE) based phase linking approaches (namely MLE-PL for the sake of brevity) present a statistically optimal estimator for the parameters of interest (e.g. DEM error, displacement rate). The rationale of MLE-PL is that interferograms are weighted by the coherence through a rigorous mathematical approach. A rich variety of the state-of-the-art MLE-PL can be found in the literature. In Ferretti et al. (2008), a prospective idea is to estimate the DEM error and displacement rate directly from the SAR images time series in one step. This idea, being intrinsically the most robust, results in an overwhelming computational burden if applied to a large set of SAR images (maybe this is why no further publication is found). While in Rocca (2007) and Guarnieri and Tebaldini (2008), the estimation process is split into two steps. In the first step, $N \times (N - 1)/2$ interferograms are formed from N SAR image acquisitions, the full coherence matrix is exploited to derive the optimal estimator (i.e. the maximum likelihood estimator) of the $N - 1$ SR phase differences. Target decorrelation is accounted for by properly weighting each interferogram depending on the coherence. In the second step, the contributions of the atmospheric phase and the decorrelation noise are separated from the displacement phase. After the Extended Invariance Principal (EXIP), under the condition that the covariance of the estimation errors committed in the first step approaches the Cram  o-Rao bound, the splitting of the MLE-PL into two steps does not entail any loss of information compared to the one step estimation in Ferretti et al. (2008).

Besides properly weighting (in a ML sense) all the available interferograms to limit spatial and temporal decorrelation, another advantage of MLE-PL approaches is that the estimates are asymptotically unbiased with a minimum variance by virtue of the properties of the MLE. In general, MLE-PL approaches require a priori reliable knowledge on the target statistics (i.e. the coherence) to drive the estimation algorithm. The performance of MLE-PL approaches thus strongly depends on the reliability of the prior coherence information. In most studies, this information is obtained from the modeling of the temporal decorrelation of targets under observation (not a trivial issue).

In the following, the two-step MLE-PL is presented in detail.

First step Consider a time series of N SAR images, a multi-variate pixel x_i contains a local observation for N dates,

$$x_i = [x_i^1, x_i^2, \dots, x_i^N] \quad (1.9)$$

Under the hypothesis of distributed scattering, x_i follows a zero-mean multivariate circular normal distribution with the probability density function (pdf) as follows

$$f(x) = \frac{1}{\pi^N \text{Det}(\Sigma)} \exp(-x^H \Sigma^{-1} x) \quad (1.10)$$

with H indicates Hermitian conjugation, Σ the covariance of x_i given by

$$\Sigma = \Theta \Upsilon \Theta^H \quad (1.11)$$

with Θ an $N \times N$ diagonal matrix containing the true phase values that we search for.

$$\Theta = \begin{bmatrix} e^{j\theta_1} & 0 & \dots & 0 \\ 0 & e^{j\theta_2} & \dots & 0 \\ \vdots & \vdots & \ddots & \vdots \\ 0 & 0 & \dots & e^{j\theta_N} \end{bmatrix}$$

and Υ an $N \times N$ symmetric real valued matrix whose elements correspond to the coherence values of all the interferograms.

$$\Upsilon = \begin{bmatrix} 1 & \gamma_{1,2} & \dots & \gamma_{1,N} \\ \gamma_{2,1} & 1 & \dots & \gamma_{2,N} \\ \vdots & \vdots & \ddots & \vdots \\ \gamma_{N,1} & \gamma_{N,2} & \dots & 1 \end{bmatrix}$$

On the other hand, the sample covariance of x_i can be expressed as

$$C_i = E(x_i x_i^H) = \frac{1}{L} \sum_{i \in \Omega} x_i x_i^H \quad (1.12)$$

Ω is a neighborhood of statistically homogeneous pixels (i.e. multi-looking window), including L samples.

With x_i normalized such as $E(|x_i|^2) = 1$, the sample covariance matrix becomes the sample coherence matrix. Working on the coherence matrix rather than the covariance matrix can be beneficial to compensate for possible backscattered power unbalances among all the images.

The principal diagonal of the sample coherence matrix is actually a data vector of N spatially averaged intensity value, while the off-diagonal complex elements correspond to spatially multi-looked interferograms. In another way, the sample coherence matrix can be written as a Kronecker product of the interferometric coherence matrix and the interferometric phase matrix.

$$C_i = \begin{bmatrix} 1 & \gamma_{1,2} e^{j\phi_{1,2}} & \dots & \gamma_{1,N} e^{j\phi_{1,N}} \\ \gamma_{2,1} e^{j\phi_{2,1}} & 1 & \dots & \gamma_{2,N} e^{j\phi_{2,N}} \\ \vdots & \vdots & \ddots & \vdots \\ \gamma_{N,1} e^{j\phi_{N,1}} & \gamma_{N,2} e^{j\phi_{N,2}} & \dots & 1 \end{bmatrix} = |\Gamma| \circ \Phi$$

with \circ denoting the Hadamard entry-wise product operator.

Because of the phase consistency loss due to spatial averaging, the sample coherence matrix is indeed not redundant (different from the case of PSI). For this reason, it is necessary to deal with $N \times (N - 1)/2$ interferometric phases to estimate consistent $N - 1$ SR phase differences, denoted

$\theta = [\theta^1, \theta^2, \dots, \theta^N]^T$. For this estimation, we use the corresponding negative log-likelihood expressed as

$$\mathcal{L}(x_i|\Sigma) = -\log\left(\prod_{i=1}^L f(x_i; \Sigma)\right) \quad (1.13)$$

$$\begin{aligned} &= N\log|\Sigma| + \sum_{i=1}^N x_i^H \Sigma^{-1} x_i + \text{const} \\ &= N\log|\Sigma| + N\text{trace}\{\Sigma^{-1}C\} + \text{const} \\ &= N\log|\Sigma| + N\text{trace}\{\Theta\Upsilon^{-1}\Theta^H C\} + \text{const} \end{aligned} \quad (1.14)$$

The maximum likelihood estimate of θ can be obtained by minimising the previous negative log-likelihood function

$$\hat{\Sigma}(\Upsilon, \Theta) = \arg \min \mathcal{L}(x_i|\Sigma) \quad (1.15)$$

To estimate Θ , the true coherence, Υ , is required but unknown. In most cases, we use $|\Gamma|/|C|$ to estimate Υ . In so doing, it is assumed that the estimated interferometric coherence is of high accuracy (that is, in case of highly coherent target and large spatial samples L).

It follows that equation 1.15 becomes

$$\begin{aligned} \Theta_{ML} &= \arg \min N\log|\Sigma| + N\text{trace}\{\Theta|C|^{-1}\Theta^H C\} + \text{const} \\ &= \arg \min \text{trace}\{\Theta|C|^{-1}\Theta^H C\} \end{aligned} \quad (1.16)$$

The algorithm requires the minimization of a nonlinear functional, implying the use of iterative methods, because no closed form solution can be found. A possible solution is the Broyden–Fletcher–Goldfarb–Shanno (BFGS) algorithm, which is a quasi-Newton method for unconstrained nonlinear optimization. Another option to deal with bad conditioned matrices is to rely on the eigen-decomposition of C and use its generalized inverse or pseudo inverse.

Second step We now have the consistent $N - 1$ SR phase differences. Once the 2π ambiguity has been solved by phase unwrapping, denoting the first image as the reference, we can model the phase difference as

$$\Delta\varphi = \varphi_i - \varphi_1 = \varphi_i(\theta) + \alpha_i - \alpha_1 + \varepsilon \quad (1.17)$$

where θ is a vector of parameters that describe the displacement, e.g. linear velocity. $\varphi_i(\theta)$ is a set of known functions of θ such as linear, exponential, periodic, etc., corresponding to different displacement behaviors. α represents the atmospheric phase. In most cases where SAR images are acquired at intervals of several days and the spatial resolution is on the order of a few meters, the atmospheric phase turns out to be highly correlated over space and uncorrelated from one acquisition to the other. ε is the estimation error committed in the first step (i.e. related to the decorrelation noise).

In equation 1.17, the atmospheric phase appears in form of difference, it is thus convenient to directly deal with atmospheric phase difference, denoted $\omega_i = \alpha_i - \alpha_1$. Under the hypothesis of a zero-mean Gaussian model with variance σ_α^2 , the covariance matrix of the atmospheric difference is

$$\begin{aligned} \{V_{\omega\omega}\}_{mn} &= \mathbb{E}[\omega_m \omega_n] \\ &= \mathbb{E}[(\alpha_n - \alpha_1)(\alpha_m - \alpha_1)] \\ &= \mathbb{E}[\alpha_m \alpha_n] + \mathbb{E}[\alpha_1^2] - \mathbb{E}[\alpha_m \alpha_1] - \mathbb{E}[\alpha_n \alpha_1] \\ &= \sigma_\alpha^2(\delta_{n-m} + 1) \end{aligned} \quad (1.18)$$

To quantify the estimation error committed in the first step, given the phase model in equation 1.17, the Hybrid Cramér-Rao Bound (HCRB) is exploited for lower bounding the accuracy of the estimation. HCRB applies in the case where both deterministic and random unknowns are present and unifies the deterministic and Bayesian CRB in such a way as to simultaneously bound the covariance matrix of the unbiased estimate of the random unknowns and the mean square errors on the estimate of the deterministic unknowns. Let $\hat{\theta}$ be an unbiased estimator of the deterministic unknown θ and $\hat{\omega}$ an estimator of the random unknown ω . The HCRB assures

$$\mathbb{E}_{x,\omega} \begin{bmatrix} (\hat{\theta} - \theta)(\hat{\theta} - \theta)^T & (\hat{\theta} - \theta)(\hat{\omega} - \omega)^T \\ (\hat{\omega} - \omega)(\hat{\theta} - \theta)^T & (\hat{\omega} - \omega)(\hat{\omega} - \omega)^T \end{bmatrix} \geq J^{-1} \quad (1.19)$$

where $\mathbb{E}_{x,\omega}$ denotes the expectation with respect to the joint pdf of the data and the atmospheric phase, $f(x, \omega|\theta)$ (see equation 1.10). J is the hybrid information matrix and can be obtained as the sum of the standard Fisher Information Matrix (FIM), F , averaged with respect to ω and the prior information matrix I_ω (since there is no prior information about θ is available, only the prior information of the atmospheric phase is accounted for in the expression).

$$J = \mathbb{E}_\omega(F) + I_\omega \quad (1.20)$$

with

$$F = -\mathbb{E}_{x|\omega} \left\{ \begin{bmatrix} \Delta_\theta^\theta \log f(x|\omega, \theta) & \Delta_\theta^\omega \log f(x|\omega, \theta) \\ \Delta_\omega^\theta \log f(x|\omega, \theta) & \Delta_\omega^\omega \log f(x|\omega, \theta) \end{bmatrix} \right\} \quad (1.21)$$

and

$$I_\omega = -\mathbb{E}_\omega = \left\{ \begin{bmatrix} 0 & 0 \\ 0 & \Delta_\omega^\omega \log f(\omega) \end{bmatrix} \right\} \quad (1.22)$$

where \mathbb{E}_ω denotes expectation with respect to $f(\omega)$. Δ_x^y defines a matrix of the second order partial derivatives with respect to two multidimensional variables (x, y) , $\{\Delta_x^y\}_{m,n} = \frac{\partial^2}{\partial x_m \partial y_n}$.

Given that

$$f(\omega) = \frac{1}{\pi^N \text{Det}(V_\omega)} \exp(-\omega^H V_{\omega\omega}^{-1} \omega) \quad (1.23)$$

Thus,

$$\mathbb{E}_\omega[\Delta_\omega^\omega \log f(\omega)] = V_{\omega\omega}^{-1} \quad (1.24)$$

Representing the standard FIM as

$$F = \begin{bmatrix} \Lambda^T X \Lambda & \Lambda^T X \\ X \Lambda & X \end{bmatrix} \quad (1.25)$$

with $\{\Lambda\}_{m,n} = \frac{\partial \varphi_m(\theta)}{\partial \theta_n}$ and X is an $N \times N$ matrix representing the FIM associated with the estimate of the phase difference $\Delta\varphi$, with $X = 2L(\Upsilon \circ \Upsilon^{-1} - I_N)$.

The hybrid information matrix, J , is thus

$$J = \begin{bmatrix} \Lambda^T X \Lambda & \Lambda^T X \\ X \Lambda & X + V_{\omega\omega}^{-1} \end{bmatrix} \quad (1.26)$$

Computing the inverse of J and extracting the upper left block, we have

$$\mathbb{E}_{x,\omega}[(\hat{\theta} - \theta)(\hat{\theta} - \theta)^T] \geq (\Lambda^T (X^{-1} + V_{\omega\omega})^{-1} \Lambda)^{-1} \quad (1.27)$$

In practice, we substitute X by its perturbation, $X_\epsilon = X + \epsilon I_N$ to ensure that the HCRB exists finite.

The term $X^{-1} + V_{\omega\omega}$ in equation 1.27 represents the covariance matrix of the total phase noise, with X^{-1} accounting for the decorrelation noise and $V_{\omega\omega}$ accounting for the atmospheric noise.

Accordingly, the decorrelation noise, ϵ , can be considered being asymptotically¹ distributed as a zero-mean multivariate normal process, with the same covariance as the one predicted by the CRB.

$$\epsilon \sim N(0, \lim_{\epsilon \rightarrow 0} (X + \epsilon I_N)^{-1}) \quad (1.28)$$

This leads to

$$\Delta\varphi \sim N(\varphi(\theta), \lim_{\epsilon \rightarrow 0} (W_\epsilon)) \quad (1.29)$$

with

$$W_\epsilon = (X + \epsilon I_N)^{-1} + \sigma_\alpha^2 I_N \quad (1.30)$$

To provide a closed form solution for the estimation of θ from $\Delta\varphi$, most literature focused on the case where $\Delta\varphi(\theta)$ is a linear function of θ , i.e. $\varphi(\theta) = A\theta$ (Ansari et al. (2018), Guarnieri and Tebaldini (2008, 2007)). Then, the MLE of θ from $\Delta\varphi$ can be derived by minimising with respect to θ the following quadratic form

$$\mathcal{L}(\theta) = (\Delta\varphi - A\theta)^T W_\epsilon^{-1} (\Delta\varphi - A\theta) \quad (1.31)$$

The solution is given by

$$\hat{\theta} = \lim_{\epsilon \rightarrow 0} (A^T W_\epsilon^{-1} A)^{-1} A^T W_\epsilon^{-1} \Delta\varphi \quad (1.32)$$

According to equation 1.32, the MLE of θ corresponds to a weighted L2 norm fit of the model $\Delta\varphi(\theta)$ and W_ϵ^{-1} can be interpreted as the set of weights which allows taking the target decorrelation and the atmospheric noise into account. The covariance of $\hat{\theta}$ is given by equation 1.33, which is the same as in equation 1.27.

$$\mathbb{E}[(\hat{\theta} - \theta)(\hat{\theta} - \theta)^T] = \lim_{\epsilon \rightarrow 0} (A^T ((X + \epsilon I_N)^{-1} + \sigma_\alpha^2 I_N)^{-1} A)^{-1} \quad (1.33)$$

MLE-PL constitutes one of the most important multi-temporal InSAR approaches. It laid the foundation for many recent developments such as Ansari et al. (2017, 2018), Ferretti et al. (2011), Fornaro et al. (2015). Further improvements include extending the linear displacement model to more complex displacement models such as seasonal, exponential models in the second step.

Eigendecomposition-based phase estimator

CAESAR Based on the MLE-PL, one eigendecomposition-based phase estimator has been proposed in the Component extrAction and sElection SAR (CAESAR) approach to deal with multiple scattering mechanism (Fornaro et al. (2015)) located at different heights, e.g. ground, facades and roofs. This approach allows the tomographic extraction and selection of multiple scattering mechanisms directly at the level of interferogram generation. The key feature is the application of the eigendecomposition to the covariance matrix of the SAR images time series and the latter is approximated by a low rank representation, i.e. only the eigenvector associated with the largest eigenvalue is considered in the phase estimation.

Indeed, the interferometric phase can be assumed to be low rank, or even rank-1 in the case of single scattering mechanism (i.e. PS). However, the decorrelation process is not a low rank nature, it can be a symmetric Toeplitz matrix that requires the entire spectral components. Therefore, the CAESAR approach compromises the optimality in phase estimation, in spite of being advantageous in terms of computational efficiency.

1. either the estimation window is large or there is sufficient number of highly coherent interferometric pairs

EMI Ansari et al. (2018) proposed another eigendecomposition-based phase estimator, namely Eigendecomposition-based Maximum likelihood estimator of Interferometric phase (EMI) approach. This estimator constitutes a bridge between the previously presented MLE-PL and EVD based estimator, keeping the high phase estimation efficiency of MLE-PL and the computational efficiency of EVD. The main contribution of EMI consists of taking the coherence estimation error that affects the performance of MLE-PL into account. For this, they proposed a generalization of the covariance model that accounts for the calibration of the estimated coherence matrix by two dyads (a full rank real valued matrix σ and a scaling parameter α in equation 1.34), at the cost of increasing the computational cost.

$$\Sigma = \alpha^2 \Upsilon \circ \sigma \sigma^T \circ \Theta \Theta^H \quad (1.34)$$

where α and σ are scaling parameters that allow extra freedom for the calibration of $\hat{\Upsilon}$ which is expected to be poorly estimated. Without coherence estimation error, $\alpha^2 = 1$ and $\sigma = I$.

An eigendecomposition-based solver was proposed to increase the computational efficiency. For more computational details, please refer to Ansari et al. (2018). Authors concluded that the generalized covariance model proposed in EMI has been shown to be only marginally successful in improving the performance of the phase estimation. A follow-on research to further generalize the covariance model is necessary to better account for coherence estimation error.

1.3.4 Multi-link InSAR

An alternative heuristic yet effective approach is the multi-link InSAR approach proposed by Pinel-Puysségur et al. (2012). This approach constructs versions of wrapped interferograms using different interferometric paths, then combines them to obtain an estimate of SR wrapped interferograms. The idea behind is to exploit as many as possible interferometric pairs, but to minimise the effect of target decorrelation by forming interferograms from properly selected pairs.

In this approach, the interferometric network is represented by a graph where each node is an acquisition date and each link is an interferogram (Figure 1.6). The principle consists of combining sets of interferograms to form multiple effective interferograms with the same start and end dates, and then aggregating the latter to retrieve the phase consistency in the wrapped interferograms.

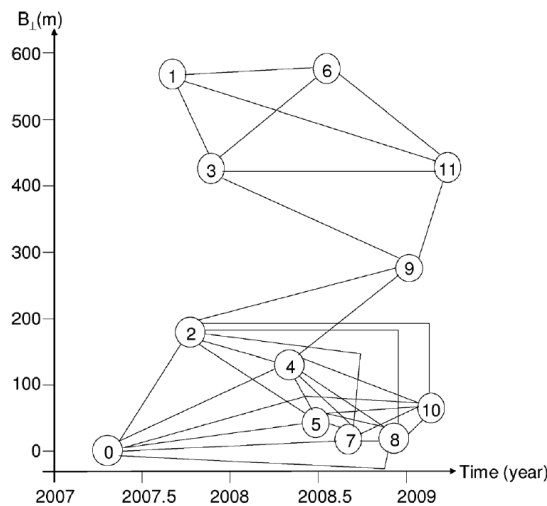


Figure 1.6 – Example of a graph of the interferometric network. For example, between the date 0 and the date 2, we have 0-4, 0-2-4, 0-5-4, 0-7-4, 0-8-4, 0-7-8-4, 0-5-10-4, ... as path. (Pinel-Puysségur et al. (2012))

Between any two acquisitions k and l in an interferometric network, there can be several paths, including the path of the interferogram between dates k and l , I_{kl} , and paths passing by other

intermediate acquisitions, e.g. $I_{km}, I_{m,l}$. In the latter case, the theoretical interferometric phase on each path, ϕ_{kl} , is estimated as the sum of the phases modulo 2π ,

$$\hat{\phi}_{kl} = (\phi_{k,m_1} + \phi_{m_1 m_2} + \dots + \phi_{m_n l}) \mod 2\pi \quad (1.35)$$

For practical reasons, ϕ_{kl} is only computed for path length smaller than some value (e.g. 3, $m_n = m_3$ in equation 1.35) to limit the computational time. A colinearity criterion, C_{kl} , is proposed to indicate the quality of each estimated phase on each path. Indeed, the coherence cannot be estimated directly because no amplitude is associated with $\hat{\phi}_{kl}$. C_{kl} can be considered as a modified estimate of the coherence. Given the fact that for natural scenes, the phase should vary smoothly in space, the colinearity criterion aims to characterize at each pixel of the estimated $\hat{\phi}_{kl}$ the local spatial variability of the phase. For a given pixel P , we define a small square window Ω ($\omega \times \omega$) centered on P but excluding P . The objective is to compare the estimated phase over P , $\hat{\phi}(P)$, and the estimated phase over its neighbours inside the square window, $\hat{\phi}(P')$ with $P' \in \Omega$. One measure of the closeness corresponds to the scalar product between $e^{i\hat{\phi}(P)}$ and $e^{i\hat{\phi}(P')}$, which is equal to $\cos(\hat{\phi}(P') - \hat{\phi}(P))$.

The colinearity is defined as

$$C(P) = \max(\cos(\hat{\phi}(P) - \bar{\phi}_\Omega), 0) \max\left(\frac{\sum_{P' \in \Omega} \cos(\hat{\phi}(P') - \hat{\phi}(P))}{\omega^2 - 1}, 0\right) \quad (1.36)$$

with $\bar{\phi}_\Omega$ the mean phase on Ω computed as follows,

$$\bar{\phi}_\Omega = \arg\left(\sum_{P' \in \Omega} e^{i\hat{\phi}(P')}\right) \quad (1.37)$$

C lies between 0 and 1. It is high if $\hat{\phi}(P)$ is close to $\bar{\phi}_\Omega$ and noise is weak in the neighbourhood Ω .

The estimates, $\hat{\phi}_{kl}$, on all paths are then combined into a single estimate, called the multi-link SAR interferogram.

$$\hat{\phi}_{kl} = \arg\left(\sum_{i=1}^M C_{kl}^i e^{i\hat{\phi}_{kl}^i}\right) \quad (1.38)$$

To further reduce the computational cost, for two acquisitions k and l , if multi-link SAR interferograms have already been computed on one path, it is preferred to consider only this path instead of considering all paths.

According to Pinel-Puysségur et al. (2012), this approach is particularly efficient in high temporal decorrelating area. Despite the good results obtained in the applications, one main drawback of this approach lies in the fact that there is no clear and formal assessment of the criteria which should drive the selection of the image pairs to be used (the selection still remains subjective).

1.3.5 Least-square phase estimator

The least-square phase estimator proposed in Samiei-Esfahany et al. (2016) resolves the SR wrapped phase estimation problem from the all-combination interferogram network (Figure 1.2 (d)) based on the integer least square principle. In this approach, the estimation problem is modeled as a system of linear equations with some integer (integer ambiguity) and real (SR phase difference) unknowns. A bootstrap estimator is used for joint estimation of the SR phase difference and the integer ambiguity. A full error propagation scheme is also proposed by performing a large number of simulations of SLC image samples.

Let ϕ_{mn} be regarded as an observation, ϕ_{om} and ϕ_{on} regarded as unknowns. The linear functional model is given by

$$\mathbb{E}(\phi_{mn}) = \begin{cases} \phi_{om} - \phi_{on} + a_{nm}(2\pi) & \text{if } n, m \neq o \\ \phi_{om} & \text{if } n = o \\ -\phi_{on} & \text{if } m = o \end{cases} \quad (1.39)$$

where a_{mn} is an integer ambiguity term. The value of $\phi_{om} - \phi_{on}$ can only lie between -2π and 2π , because they are wrapped phase. Therefore, $a_{mn} \in \{-1, 0, 1\}$.

In matrix form, we have

$$\mathbb{E} \left\{ \begin{bmatrix} \phi_{o1} \\ \vdots \\ \phi_{o(N-1)} \\ \vdots \\ \phi_{nm} \end{bmatrix} \right\} = \begin{bmatrix} 0 & \dots & 0 \\ \vdots & \ddots & \vdots \\ 0 & \dots & 0 \\ 2\pi & & \\ & \ddots & \\ & & 2\pi \end{bmatrix} \begin{bmatrix} \vdots \\ \vdots \\ \vdots \end{bmatrix} + \begin{bmatrix} 1 & & \\ & \ddots & \\ & & 1 \\ & & & -1 \dots 1 \\ & & & \vdots \end{bmatrix} \begin{bmatrix} \phi_{o1} \\ \vdots \\ \phi_{o(N-1)} \end{bmatrix} \quad (1.40)$$

In equation 1.40, the SR phase difference estimation problem is described in a hybrid system of linear equations with real unknowns ϕ_{on} and integer unknowns a_{mn} . This hybrid system can be synthesized as

$$\mathbb{E}\{y\} = Aa + Bb \quad (1.41)$$

where y is the vector of observations (i.e. phases of all interferometric combinations), a and b are the vectors of integer and real-valued unknown parameters to estimate.

The weighted integer least-square (ILS) solution is given by

$$\hat{a}, \hat{b} = \arg \min_{a \in \mathbb{Z}, b \in \mathbb{R}} \|y - Aa - Bb\|_W^2 \quad (1.42)$$

where W is the weight matrix, e.g. coherence or Fisher information index.

As in most least-square estimation, an error covariance matrix is also estimated to quantify the error propagation from the dispersion of observations to the final SR phase difference estimates. For this, a large number of simulations of SLC image samples are performed, based on the hypothesis that SLC images follow a multivariate circular Gaussian distribution. The observation error covariance is estimated from the set of interferograms samples generated from the SLC image samples in the following way,

$$Q_y = \frac{1}{M} \sum_{i=1}^M (y_i - \mathbb{E}(y))(y_i - \mathbb{E}(y))^T \quad (1.43)$$

The error covariance of the final SR phase difference estimation is given by

$$Q_{\hat{b}} = (B^T W B)^{-1} B^T W Q_y W B (B^T W B)^{-1} \quad (1.44)$$

For more technical details, please refer to Samiei-Esfahany et al. (2016).

The main advantage of this approach lies in the flexibility, i.e. it can be applied to any subset of interferograms. Moreover, the error propagation scheme provides an error representation in case without accurate observation error information. The main drawback of this approach is the high computational cost.

1.3.6 Combination of PSI & DSI

On one hand, PS approaches struggle to extract displacement information for areas characterized by DS. On the other hand, DS approaches cannot provide point-wise displacement measurements. To overcome the limit of both PSI and DSI, a proper combination of PSI and DSI constitutes the key element of several approaches. In this section, an early approach combining PSI and SBAS (i.e. StaMPS) and a recent approach exploiting both PS and DS pixels in a MLE-PL framework (i.e. squeeSAR) are presented.

StaMPS

Hooper (2008) combined both PS and SBAS approaches by processing jointly the PS and pixels that decorrelate little over short time intervals, namely slowly decorrelating filtered phase (SDFP) pixels. PS candidates are selected according to the same criteria presented in Section 1.3.1 and further evaluated according to a phase analysis (i.e. estimate the decorrelation noise for a pixel, then characterize the latter in terms of a measure similar to the coherence and use this measure to verify the phase stability) applied to the SR interferograms (Hooper et al. (2007)). Only PS candidates that present phase stability are considered in the phase estimation. SDFP pixels are also selected in the same way as PS, but further evaluated according to a phase analysis applied to small baseline (SB) interferograms. Note that the difference between SR-interferograms and SB-interferograms lies in the fact the SB interferograms are subject to spatial and spectral filtering, while SR-interferograms are not. In order to combine the selected PS and SDFP pixels, the equivalent SB interferograms are calculated for the PS pixels by recombination of SR interferograms. The SB interferograms from both PS and SDFP pixels is then combined : for a pixel occurs in both data sets, a weighted mean phase is calculated by summing the complex signal from both data sets, with the amplitude of each fixed to an estimate of the signal-to-noise ratio for the pixel in that data set. A 3D phase unwrapping algorithm is then applied to the combined SB interferometric network. The unwrapped phase of the SB interferograms are inverted to derive a SR phase difference for each pixel, as done in the SBAS approach.

This approach was included in the open-access software StaMPS (Stanford Method for Persistent Scatterers) developed by A. Hooper. The problem of phase bias in long time series, due to the utilization of SB interferograms alone, in the SBAS approach also exists in this approach.

SqueeSAR

The squeeSAR approach (Ferretti et al. (2011)) proposed a way to properly combine PS and DS to increase the density of measurement points, at the same time, to preserve the high quality phase estimation. It has been developed under the assumption that radar returns and geophysical parameters of interest (e.g. DEM error, displacement rate) are common to all pixels belonging to a certain area, it is thus desirable to process them jointly. The main idea consists of spatially averaging the DS points over statistically homogeneous areas to increase the signal-to-noise ratio, without compromising the identification of coherent PS point-wise scatterers. For this, a space adaptive filtering is necessary. Ferretti et al. (2011) proposed the DespecKS algorithm, whose key element is a definition of a statistical test capable of discriminating whether two pixels belonging to an interferometric data stack can be considered statistically homogeneous or not. The well-known two-sample Kolmogorov-Smirnov (KS) test has been adopted in the SqueeSAR approach. Since the KS test cannot be applied to complex data, the amplitude is used instead of the complex reflectivity. The MLE-PL approach is applied to the selected statistically homogeneous DS points to obtain the consistent $N - 1$ SR phase difference values by retrieving the phase consistency. The latter allows treating multi-looked interferograms as single-look interferograms and thus provides the bridge between PS and DS and makes it possible to characterize a DS though $N - 1$ consistent SR phase

values as the PSI. Afterwards, the DS and PS points are exploited together using the standard PS processing chain.

Compared to the standard PSI processing chain, the computational cost represents the main drawback of the squeeSAR approach.

1.3.7 Sequential estimator

A recent attempt of near-real-time processing proposes a sequential estimator (Ansari et al. (2017))) that works on mini stacks (far below the total number of images in the time series, e.g. between ten and twenty) of SAR images. It performs data compression by a linear transformation within each mini stack to reduce the amount of data to save and estimate the coherence by formation of artificial interferograms between the compressed mini stack and the mini stack of new data.

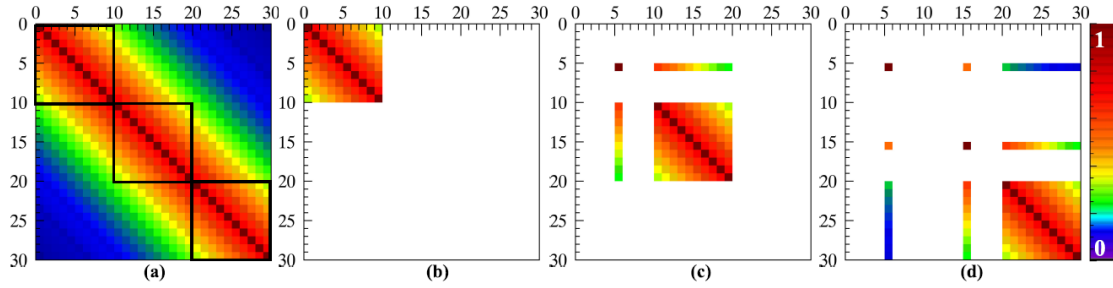


Figure 1.7 – Illustration of the sequential estimator. a) full coherence matrix of a SAR image time series : the Sequential Estimator divides the stack into isolated mini-stacks indicated by the black boxes along the diagonal. At each sequence, one mini-stack is processed and compressed; the mini-stacks are replaced by their compressed components in further sequences. The coherent signals among the mini-stacks are retrieved by generation of artificial interferograms. b) coherence matrix at the initial sequence. c) second sequence : the isolated dot on the diagonal indicates the compressed SLC of the unavailable first mini-stack; the square depicts the acquired mini-stack; and the sparse rectangles represent the generated artificial interferograms between the compressed and the acquired SLCs. d) third sequence : the artificial interferograms are generated with respect to the compressed SLCs of the first and the second mini-stacks. (Ansari et al. (2017))

The sequential estimator begins with the acquisition of a mini-stack of SLCs (\ll the total number of images). The latter undergoes a two-step process : phase estimation and data compression. In the phase estimation step, the phase of each SLC in the mini-stack with respect to a reference SLC is estimated by the MLE-PL approach (section 1.3.3). In the data compression step, the SLCs are compressed by the estimation of a low-rank subspace and a further projection of the data to this subspace.

A linear transformation is chosen for data compression. Indeed, PCA is commonly used to provide a spectral decomposition of the data space, such that the eigenvectors corresponding to the highest eigenvalue represents the underlying most coherent signal. However, PCA cannot provide an accurate estimation to the phase linking (see CAESAR in section 1.3.3). Therefore, the solution provided by MLE is used. A new orthonormal basis is sought with its first component defined as

$$v_{ML} = \frac{\exp(j\hat{\phi}_{ML})}{\|\exp(j\hat{\phi}_{ML})\|} \quad (1.45)$$

The projection matrix corresponding to v_{ML} is given by

$$C_{ML} = v_{ML}v_{ML}^H \quad (1.46)$$

and its orthogonal complement is given as

$$C_{ML}^\perp \oplus C_{ML} = I \quad (1.47)$$

The coherence matrix can then be projected to the residual subspace through the orthogonal complement. The eigendecomposition of the latter provides the complementary vectors of the sought orthonormal basis, denoted $\{v_1; v_2; \dots; v_{N-1}\}$. The transformation matrix is defined as

$$T = \{v_{ML}; v_1; \dots; v_{m-1}\} \quad (1.48)$$

The mini-stack of SLCs (N-dimensional) is compressed by its transformation to a low rank subspace (m-dimensional)

$$\tilde{z} = T^H z \quad (1.49)$$

Ansari et al. (2017) kept the first component, i.e. the ML component, corresponding to the most coherent signal component, the mini-stack compressed to a single SLC is given by

$$\tilde{z}_{ML} = T_1^H z = v_{ML}^H z \quad (1.50)$$

The result of the processing of the first mini-stack is thus archiving the compressed SLCs to a single SLC. For the subsequent mini-stacks, the same two-step processing is performed with minor changes. Prior to the phase estimation, the compressed SLC is pretended to the newly acquired mini-stack. Artificial interferograms are generated between the newly acquired SLCs and the compressed SLC of the mini-stack prior to the current one and are exploited jointly with interferograms generated between newly acquired SLCs in the MLE-PL approach. Indeed, artificial interferograms substitute the lost coherent signal among the isolated mini-stacks.

In each mini-stack, the phase with respect to a reference SLC, i.e. phase difference, is estimated by MLE via phase linking. In order to link the estimated phases of different mini-stacks, a datum connection step is necessary. This is performed through a phase-linking on the \tilde{z}_{ML} component, that is, the compressed SLC inside each mini-stack is treated as a new stack. In this way, the phase differences are temporally integrated to retrieve the phase difference of each mini-stack relative to a new arbitrary but unique reference.

The sequential estimator is proposed as an efficient processing scheme to exploit the unprecedented big data in InSAR. It constitutes an important step towards an near-real-time processing scheme while retaining the optimality of the phase estimation. However, this estimator presents several major drawbacks such as the need for a long time period to form an appropriate mini stack, non-robustness to all kinds of temporal decorrelation mechanisms (rank-1 subspace considered in data compression) and Gaussian hypotheses of SAR image statistics (these hypotheses cannot be justified especially in case of high resolution SAR images).

1.4 Conclusion & perspective

Towards operational monitoring of Earth surface displacement

Despite the recent advances in the development of multi-temporal InSAR approaches and the revolutionary results obtained in displacement measurements by SAR images, perspectives of further improvement or development still exist, that is, towards operational monitoring of displacement by means of adequate multi-temporal InSAR approaches. For an operational purpose, the developed multi-temporal InSAR approaches should be able to timely deliver reliable displacement products. Therefore, on one hand, the developed multi-temporal InSAR approaches should be capable of integrating new arriving SAR images with appropriate computational time; on the other hand, the hypotheses made in these approaches should be as representative as possible of the reality.

Most actual multi-temporal InSAR approaches are mainly retrospective analysis tools and do not allow efficient gradual integration of new SAR images that arrive over time. It is necessary to restart part of or the whole displacement estimation processing chain, which would be prohibitively expensive in practice and does not answer the need for operational monitoring. It is true that the PSI has widely been used for displacement monitoring of urban infrastructures at regional and national scales, including operational monitoring of major public works. The instability of PS candidates with the increase of the number of SAR images and the complexity of the iterative processing chain make an efficient integration of new SAR images extremely challenging. Among DSI approaches, the SBAS approach does not require restarting the processing chain from the very beginning, because only SB interferograms need to be computed between the new arriving and previous SAR images. However, the SB network compromises the phase estimation accuracy, large bias can exist especially for interferograms of large time span. The sequential estimator represents an important development for operational use. However, it presents several shortcomings such as the phase estimation quality inside each mini-stack limited by the number of SAR images used, non-robustness to all kinds of temporal decorrelation mechanisms (only one eigenvector is retained in the data compression step) and Gaussian hypotheses of SAR image statistics that cannot be justified especially in case of high resolution SAR images (Mian et al. (2019)). Indeed, hypotheses of complex Gaussian distributions have often been made for SAR image statistics for the sake of simplicity. The estimation built on a Gaussian hypothesis can give very poor results that will affect the reliability of the displacement information. Preliminary studies about the use of M-estimators for SAR images covariance matrix estimation in case of non Gaussian properties can also be found in Schmitt et al. (2014) and Wang and Zhu (2016). However, these works do not consider the prior knowledge on the structure of the covariance matrix (i.e. Kronecker product), which can lead to poor estimation performance when data used are strongly heterogeneous. Therefore, efforts are still necessary to develop more elaborated recursive and robust multi-temporal InSAR approaches allowing for efficient gradual integration of new arriving SAR images and considering non Gaussianity of data statistics.

Motivated by the above, I want to develop new recursive and robust multi-temporal InSAR approaches for operational use, with the help of colleagues specializing in statistical signal processing, in particular in robust covariance matrix estimation. For this, the baseline method chosen is the MLE-PL approach, because it provides a mathematical framework for obtaining an optimal displacement estimation in the statistical sense. Moreover, this approach allows for a full exploration of all possible combinations of a SAR image stack by formally taking the impact of the temporal decorrelation of the observed phenomenon into account. More importantly, from the formulation of this method, we can interpret interferograms as elements of the full sample covariance matrix of the SAR image time series, which gives perspective to perform robust and recursive displacement estimation by means of advanced statistical tools dedicated for covariance matrix estimation. This work has been initiated in the Master 1st year internship of Ségolène Martin and followed up in the Ph.D thesis of Viet-Hoa Vu Phan, started in October 2020. Moreover, this work, together with missing data imputation in SAR displacement time series presented in Chapter 3, constitute a work package in my ANR young researcher project. Another Ph.D thesis will also be set up in order to strengthen the work force and to ensure the successful completion of this work.

2

Impute missing data in displacement measurement time series

2.1 Introduction

Despite the large volume of available, satellite and in-situ, data for displacement measurement, the missing data problem is still a frequently encountered issue. In case of optical imagery derived displacement time series, cloud cover constitutes one of the main reasons of data incompleteness. While in case of SAR imagery derived displacement time series, data incompleteness is mainly due to surface changes of the observed targets that induce coherence loss. In both cases, technical limitations of the displacement extraction methods (e.g. offset tracking, InSAR) and thresholding according to the reliability of the estimated displacement values also create data gaps.

Missing data can hinder global and accurate observations of the displacement behavior, and further hamper thorough understanding of the underlying physical phenomenon that induces the displacement. Imputation of missing data in SAR/optical displacement time series can be of particular interest to improve the data completeness and reliability, especially for decorrelating targets such as glaciers and vegetated volcanoes, etc.

Indeed, the missing data problem exists since a long time (Preisendorfer (1988), Rubin (1976)) and has been well-documented especially for optical and infrared satellite images where data quality is strongly dependent on cloud coverage (Lin et al. (2014), Melgani (2006), Wu et al. (2018), Zhang et al. (2018)). An important framework of missing data imputation has already been established in ocean-atmosphere, vegetation and hydrology domains (Alvera-Azcarate et al. (2007), Beckers and Rixen (2003), Gerber et al. (2018), Hocke and Kämpfer (2009), Kondrashov and Ghil (2006), Verger et al. (2013)). However, in displacement measurement, previously existing methods to handle missing data, e.g. regression analysis, nearest-neighbor interpolation (NNI), inverse/angular distance weighting (IDW), spline interpolation and kriging (Chang et al. (2018), Gudmundsson et al. (2002), Jolivet et al. (2011), Wu et al. (2013)), mainly use spatial interpolation of missing values from existing values. Most of these methods include limited temporal information, which can be an issue when dealing with time-evolving physical processes. Moreover, no particular attention had been paid to missing data issues especially in SAR-derived products such as interferogram and offset time series before the Ph.D thesis of Alexandre Hippert-Ferrer. The substantial lack of advanced approaches (i.e taking information richness in both spatial and temporal dimensions and complex data statistics into account) to deal with missing data in SAR/optical displacement time series became obvious.

Motivated by this, I aimed to propose new methods, taking both temporal and spatial characteristics of the displacement behavior into account, to impute missing data in displacement time series. These works have been carried out in the Master 1st year internship of Rémi Prébet (04/2017 - 07/2017) and in the Ph.D thesis of Alexandre Hippert-Ferrer (10/2017 - 10/2020). The common principle of the proposed methods relies on the construction of the temporal or spatio-temporal covariance matrix of the displacement time series and the analysis of the latter by eigenvalue decomposition (ED) or singular value decomposition (SVD) in terms of data-based empirical orthogonal functions (EOFs). The interest of the EOF-based analysis lies in the fact that these orthogonal functions can be classified into trends, oscillatory patterns, and noise. Given any displacement field time series, the EOF-based analysis finds a set of orthogonal spatial (temporal) patterns along with a set of associated uncorrelated time (space) series. A few leading EOF modes, corresponding to the dominant oscillatory and/or trend modes, are necessary to optimally reconstruct the initial displacement signal.

In the following, I will present the Principle Modes (PM) method proposed in the internship of Rémi for displacement signal retrieval from noisy interferogram time series (Prébet et al. (2019)), the Expectation-Maximization Empirical Orthogonal Functions (EM-EOF) (Hippert-Ferrer et al. (2020a)) and the extended EM-EOF methods (Hippert-Ferrer et al. (2020b)) proposed in the Ph.D thesis of Alexandre for missing data imputation. For this, I begin with the description of the common theoretical background of the three methods and end up with the perspective of this research direction, that is, towards the development of parametric methods for missing data imputation.

2.2 Common theoretical background - EOF-based analysis

2.2.1 Data organization

Suppose that we have a displacement time series represented by a spatio-temporal field $X(s, t)$ which contains the values of the field X at position s and at time t . The values of the field are noted $(x_{st})_{1 \leq s \leq p, 1 \leq t \leq n}$ and may be missing. In matrix form, the spatio-temporal field can be written as :

$$X = \begin{pmatrix} \mathbf{x}_1 & \mathbf{x}_2 & \dots & \mathbf{x}_n \end{pmatrix} = \begin{pmatrix} x_{11} & x_{12} & \dots & x_{1n} \\ x_{21} & x_{22} & \dots & x_{2n} \\ \vdots & \vdots & \ddots & \vdots \\ x_{p1} & x_{p2} & \dots & x_{pn} \end{pmatrix} \quad (2.1)$$

where each column $\mathbf{x}_t = (x_{1t}, x_{2t}, \dots, x_{pt})^T$ is an observation over p positions at a given time t , and each row is a time series at a given position s . An observation \mathbf{x}_t can be incomplete, initially represented by a 2-D field and reshaped as a column vector of length p .

2.2.2 Sample covariance estimation

For the sample temporal covariance estimation, the spatial mean of the field at each time (i.e. mean of each column) is subtracted to form the *spatial anomaly* X' :

$$X' = X - \mathbf{1}_p \bar{X} \quad (2.2)$$

where $\mathbf{1}_p = (1, \dots, 1)$ is a unit vector of length p and $\bar{X} = (\bar{x}_1, \bar{x}_2, \dots, \bar{x}_n)$ is the line vector containing all observation means with each \bar{x}_t being the spatial mean of observation \mathbf{x}_t computed as :

$$\bar{x}_t = \frac{1}{p} \sum_{s=1}^p x_{st} \quad (2.3)$$

The sample temporal covariance matrix of X is given by :

$$\hat{C} = \frac{1}{p-1} X'^T X' \quad (2.4)$$

Note that p can either be equal to the number of all spatial samples or be a subset of samples representing a target or a particular object in the spatial field. In the latter, the data matrix X represents only the target under consideration.

2.2.3 Eigenvalue decomposition

The eigenvectors, which are the EOFs of matrix \hat{C} , can be found by resolving the following equation :

$$\hat{C}U = U\Lambda \quad (2.5)$$

where U is a $n \times n$ orthogonal matrix and $\Lambda = \text{diag}(\lambda_1, \dots, \lambda_n)$ contains the eigenvalues λ_i of matrix \hat{C} in decreasing order on its diagonal¹. Each column \mathbf{u}_i of U is an eigenvector of \hat{C} and corresponds to each eigenvalue λ_i . U has the property that $U^T U = U U^T = I$, indicating that the eigenvector is orthogonal to each other, hence the name EOF.

Since \hat{C} is a symmetric matrix, it follows from the spectral representation theorem that the eigenvalues and the eigenvectors decompose \hat{C} as :

$$\hat{C} = \lambda_1 \mathbf{u}_1 \mathbf{u}_1^T + \lambda_2 \mathbf{u}_2 \mathbf{u}_2^T + \dots + \lambda_n \mathbf{u}_n \mathbf{u}_n^T \quad (2.6)$$

This decomposition allows a representation of the temporal covariance matrix in terms of EOF modes which describe the temporal variability of the displacement field (Hannachi et al. (2007)), to each eigenvalue corresponding a measure of the fraction of the total variance explained by the considered EOF mode. This fraction is obtained by dividing λ_i by the sum of all eigenvalues. In general, the first EOF modes represent most of the variability, which means that most of the information about the displacement behavior observed in the spatio-temporal field X can be explained by just a few leading EOF modes.

2.2.4 Data reconstruction

The spatial anomaly, X' , can be reconstructed by summing the principal components (PCs) a_i multiplied by the eigenvectors :

$$\hat{X}' = \sum_{i=1}^n a_i \mathbf{u}_i^T \quad (2.7)$$

with the i th PC $a_i = X' \mathbf{u}_i$ corresponding to the projection of X' on the i th eigenvector, i.e. a spatial pattern map on the orthonormal space engendered by the eigenvector \mathbf{u}_i . In other words, the eigenvectors, \mathbf{u}_i , can be considered as function of time, whereas the PCs, a_i , can be considered

1. Note that since $U^{-1} = U^T$, equation (2.5) is equivalent to performing a SVD on matrix \hat{C} and can be noted $\hat{C} = U\Lambda U^T$.

as functions of space. The former represents the variability modes of all the positions over time and the latter is there to modulate this variability according to the position in space.

By truncating the summation of (2.7) at some $R \ll n$, we will keep the first EOF modes corresponding to the largest eigenvalues. To decide the optimal number of EOF modes to retain in a given decomposition, it is common to use the fraction of the variance explained by the first R EOF modes (Beckers and Rixen (2003), Hannachi et al. (2007)). A typical choice is to retain those modes that, when summed up, explain 95% of the signal. In case of known data uncertainty, the number of modes to retain can be determined such that the misfits between the reconstruction and the noisy data are, on average, of the order of magnitude of the data uncertainty (Kositsky and Avouac (2010)). Moreover, when the statistical characteristics of the noise present in the data are known, a Monte Carlo method that generates random matrices of noise having the same statistical characteristics can help decide when pure noise is likely to be interpreted as a displacement signal if an EOF mode is retained (Björnsson and Venegas (1997), Overland and W. Preisendorfer (1982)). Despite the existing methods and criteria available in the literature, finding an optimal number of EOF modes remains a challenge, especially in case where noise is spatially or spatio-temporally correlated as the displacement signal, it is thus difficult to efficiently separate the noise from the displacement signal.

To get the reconstructed field \hat{X} , we finally add the spatial mean back to the anomaly :

$$\hat{X} = \hat{X}' + \mathbf{1}_p \bar{X} \quad (2.8)$$

In the case where a displacement field is composed of multiple objects each with a different temporal behavior, the reconstruction of the displacement field can be performed object by object. The sample temporal covariance should be estimated using only spatial samples related to each object and the reconstruction of the spatial field can be obtained from the mosaic of the reconstruction of each object.

2.3 Principal modes method

The principal modes (PM) method was proposed to retrieve displacement signal from both wrapped and unwrapped noisy interferogram time series. The main objective was to capture a coherent displacement behavior in a displacement time series with the presence of large coherence loss areas, not to directly fill in data gaps in interferogram time series. However, it laid the foundation for the development of the EM-EOF and extended EM-EOF methods, both latter dedicated to missing data imputation. If we consider coherence loss areas as data gaps, the PM method can indeed be considered as a missing data imputation method.

2.3.1 Methodology

The methodology of the PM method is simple. It relies on an EOF-analysis of the temporal covariance of an interferogram time series (technical details in Section 2.2).

Interpretation of the temporal covariance

Here, we give a detailed insight into the content of the temporal covariance.

On each interferogram, the total signal includes the displacement signal and perturbations. Decorrelation noise and atmospheric perturbations are considered as main error sources on wrapped and unwrapped interferograms respectively (Ansari et al. (2017), Guarnieri and Tebaldini (2008)).

Therefore, spatially correlated noise (atmospheric-like) and random noise are considered as perturbations in case of unwrapped interferograms; while decorrelation noise is considered in case of wrapped interferograms.

In order to facilitate the interpretation, we represent the temporal covariance C in the following way :

$$C = \mathbb{E}[x_m'^t x_n'] \quad (2.9)$$

where x_n' is a column of the data anomaly matrix, and m and n correspond to two different times (columns). \mathbb{E} is the mathematical expectation.

Taken different contributions in X into account, in case of unwrapped interferograms, C becomes

$$C = \mathbb{E}[(x_m'^d + x_m'^a + x_m'^b)^t (x_n'^d + x_n'^a + x_n'^b)] \quad (2.10)$$

$$= \mathbb{E}[x_m'^d x_n'^d + x_m'^a x_n'^a + x_m'^b x_n'^b + x_m'^d x_n'^a + x_m'^a x_n'^d + x_m'^b x_n'^a + x_m'^d x_n'^b + x_m'^a x_n'^b + x_m'^b x_n'^d] \quad (2.11)$$

where d denotes displacement, a spatially correlated noise and b random noise.

The displacement can be assumed independent of other perturbations, thus $\mathbb{E}[x_m'^a x_n'^d] = 0$ and $\mathbb{E}[x_m'^b x_n'^d] = 0$. For atmospheric-like spatially correlated noise, in general, they do not present temporal correlation. However, in the case of displacement measurement from consecutive SAR acquisitions, a common image is shared by the consecutive displacement measurements, therefore, there is a correlation between consecutive times. In what follows,

$$C = \begin{cases} \mathbb{E}[x_m'^d x_n'^d] & |m - n| > 1 \\ \mathbb{E}[x_m'^d x_n'^d + x_m'^a x_n'^a] & |m - n| = 1 \end{cases} \quad (2.12)$$

In case of wrapped interferograms time series, C becomes

$$C = \mathbb{E}[e^{j(x_n'^d - x_m'^d + x_n'^b - x_m'^b)}] \quad (2.13)$$

$$= \mathbb{E}[e^{j(x_n'^d - x_m'^d)}] \mathbb{E}[e^{j(x_n'^b - x_m'^b)}] \quad (2.14)$$

If m and n are consecutive, similarly, as there is a common image in the formation of the interferogram, strong temporal correlation can exist in the decorrelation noise; otherwise, the decorrelation noise follows the temporal decorrelating mechanism of the phenomenon under observation and $\mathbb{E}[e^{j(\phi_n'^b - \phi_m'^b)}] = \gamma_m \gamma_n$ with γ_m the interferometric coherence at time m and γ_n the interferometric coherence at time n . Thus,

$$C = \begin{cases} \gamma_m \gamma_n \mathbb{E}[e^{j(x_n'^d - x_m'^d)}] & |m - n| > 1 \\ \mathbb{E}[e^{j(x_n'^d - x_m'^d)}] \mathbb{E}[e^{j(x_n'^b - x_m'^b)}] & |m - n| = 1 \end{cases} \quad (2.15)$$

According to equations 2.12 and 2.15, in the temporal covariance C , the information is the temporal covariance between displacements at times n and m and that of spatially correlated noise in case of unwrapped interferograms or that of decorrelation noise in case of wrapped interferograms between consecutive times. The temporal covariance between displacements is continuous (i.e. between all times), whereas that of the perturbations is not (i.e. only between consecutive times). Since the temporal variation of the displacement and that of the perturbations do not have the same correlation length (i.e. frequency in spectral analysis), it is possible to separate them through a spectral analysis of the temporal covariance (Rocca (2007)).

Determination of the optimal number of EOF modes

To determine the optimal number of EOF modes to retain in the reconstruction, we proposed the root mean square deviation (RMSD) and the error reduction rate as metrics.

The RMSD can be calculated as follows :

$$\text{RMSD} = \frac{1}{\bar{\sigma}_x} \sqrt{\frac{\sum_{i=1}^N \|\hat{x}_i - x_i\|^2}{np}} \quad (2.16)$$

where $\bar{\sigma}_x$ denotes the temporal mean standard deviation, \hat{x}_i and x_i denote respectively the estimated and the observed (or true) values at each time instant i . In case of complex data, $\bar{\sigma}_x$ is replaced by $\bar{\sigma}_{e^{jx}}$, \hat{x} and x are replaced by $e^{j\hat{x}}$ and e^{jx} respectively.

The RMSD is a measure of accuracy and frequently used to measure the difference between values predicted by a model or an estimator and the values actually observed. The RMSD serves to aggregate the magnitudes of the errors in estimation for various time instants into a single measure of estimative power. Note that the RMSD is different from the average error, because the former mixes information concerning average error with information concerning variation in the errors. The effect of each error on the RMSD is proportional to the size of the squared error thus larger errors have a disproportionately large effect on the RMSD (Willmott and Matsuura (2006)).

The number of EOF modes that minimises the RMSD is denoted by $imin$ with the associated RMSD_{min} . The RMSD of the noisy data (or original data) is denoted by RMSD_{max} . The error reduction rate, τ_{err} , is defined as

$$\tau_{err} = 1 - \frac{\text{RMSD}_{min}}{\text{RMSD}_{max}} \quad (2.17)$$

The error reduction rate varies between 0 (no improvement) and 1 (perfect reconstruction). It measures the gain of accuracy with the application of a method, thus indicates the efficiency of the method.

2.3.2 Case study

Real data applications

The PM method was applied to time series of 30 interferograms constructed from consecutive Sentinel-1 A/B acquisitions between October 2016 and April 2017 over the Gorner glacier situated at the frontier between Italy and Switzerland. In this interferogram time series, low coherence is present over large area in some interferograms. Only 18 interferograms can be considered of good (fringe patterns clearly visible over the whole glacier) and moderate quality (fringe patterns are visible over part of the glacier).

The results obtained in case of unwrapped interferogram time series are shown in Figure 2.1 with several representative examples. These results, as well as those not shown here, confirm the ability of the PM method to retrieve coherent displacement patterns in real valued interferogram time series.

The results obtained in case of wrapped interferogram time series are shown in Figure 2.2 with the same examples as shown in Figure 2.1. The ability of the PM method to retrieve fringe patterns in wrapped interferogram time series is also highlighted according to these results and those not shown. In case of wrapped interferograms, besides the conclusions consistent with those obtained in case of unwrapped interferograms, two other observations need to be stressed. The first one concerns the interferogram with total coherence loss (2017/03/05 - 2017/03/11), fringe patterns have been retrieved successfully by the PM method, which seems very promising. Of course, the question arises, if the retrieved interferogram is correct. A validation with averaged offset tracking measurements confirmed this result (Figure 2.3), but the accuracy of the result cannot be validated on the order of centimeters with offset tracking measurements. The second observation concerns

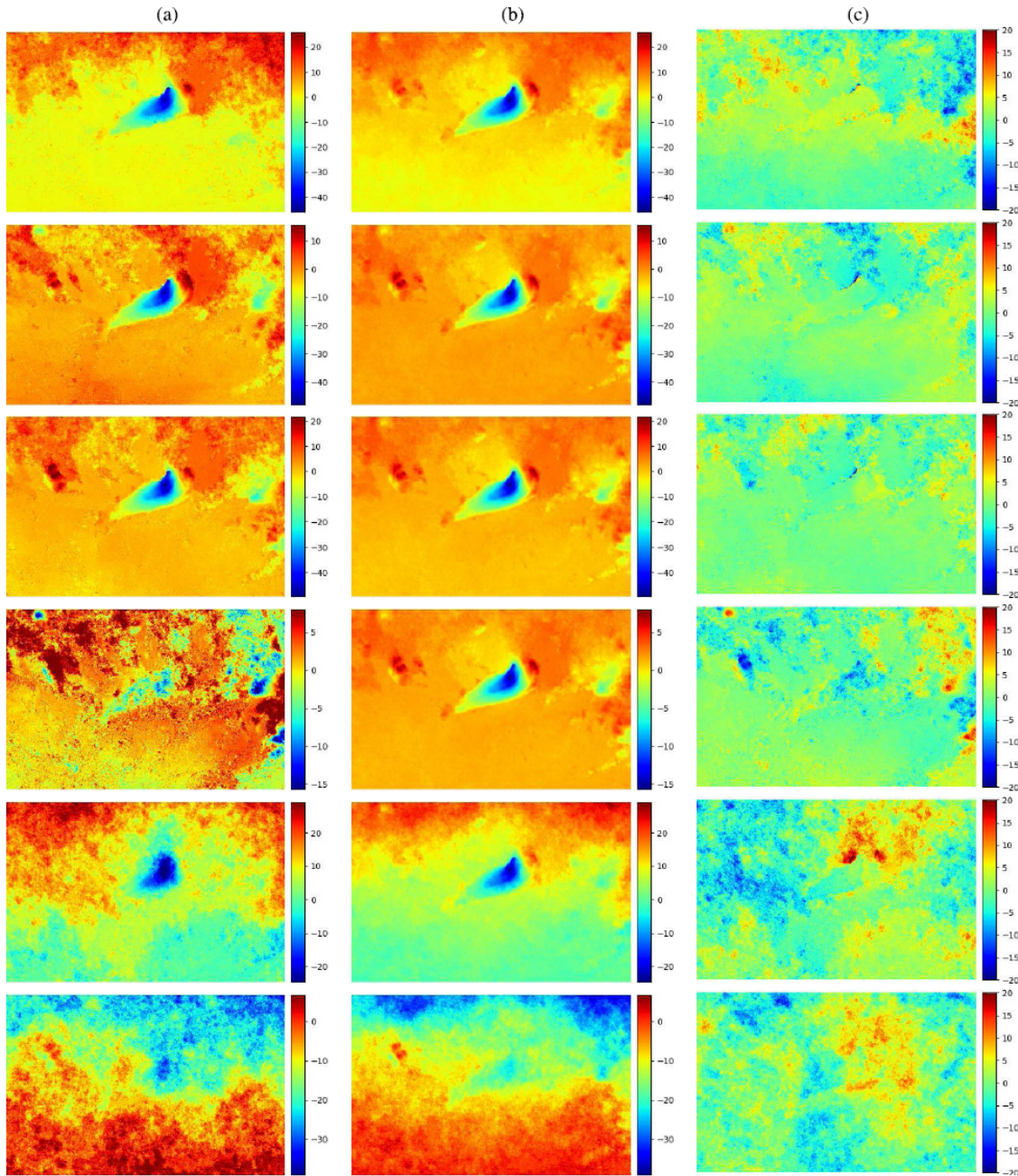


Figure 2.1 – (a) original and (b) reconstructed unwrapped interferograms (c) residual (reconstruction - original) at time spans (from top to bottom) 2016/12/17 - 2016/12/23, 2016/12/29 - 2017/01/04, 2017/02/15 - 2017/02/21, 2017/03/11 - 2017/03/17, 2017/02/03 - 2017/02/09, 2017/03/05 - 2017/03/11). The PM method does not degrade the interferograms of good quality (first three lines in Figure 2.1), the reconstructed interferograms can be considered as a filtered version of the original interferograms, with the displacement pattern over the glacier smoothed and most spatially correlated (at small scales) noise in stable areas filtered out. Larger residuals are only observed at the upper edge of the glacier where localised phase unwrapping errors exist in the original interferograms due to the transition between the fast moving glacier and the stable areas. The PM method provides an important improvement of the displacement pattern in interferograms of moderate quality (4th and 5th lines in Figure 2.1), the original interferograms are sufficiently noisy, the displacement patterns are visible but significantly deformed. For interferograms of total coherence loss (last line in Figure 2.1) where only noise is observed in the interferogram, the PM method fails to retrieve the displacement pattern. (Prébet et al. (2019)).

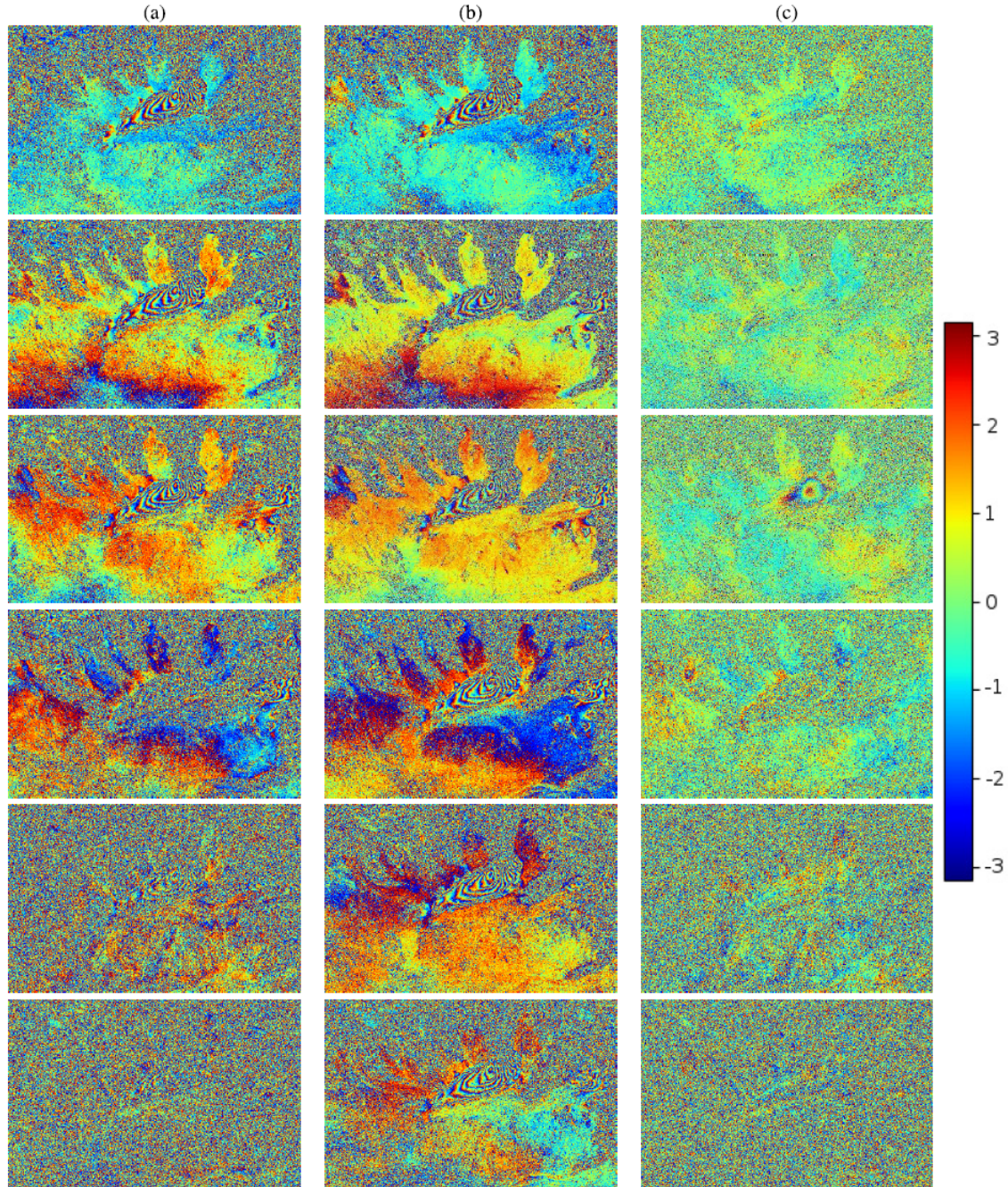


Figure 2.2 – (a) original (b) reconstructed wrapped interferograms (c) residual (reconstruction - original) modulo 2π at time spans (from top to bottom) 2016/12/17 - 2016/12/23, 2016/12/29 - 2017/01/04, 2017/02/15 - 2017/02/21, 2017/03/11 - 2017/03/17, 2017/02/03 - 2017/02/09, 2017/03/05 - 2017/03/11) (Prébet et al. (2019)).

the interferogram of good quality (2017/02/15 - 2017/02/21), displacement signal is observed in the residual, which implies that the reconstructed fringe pattern is different from that in the original interferogram. This is due to a unique event produced on the interferogram (2017/02/15 - 2017/02/21) and not observed in other interferograms in the time series. This observation showcased a limitation of the PM method against unique events present in the displacement time series. To remedy, more modes are necessary in the reconstruction to keep this part of information, at the expense of keeping more noise at the same time. Another solution consists of a further analysis of the residual.

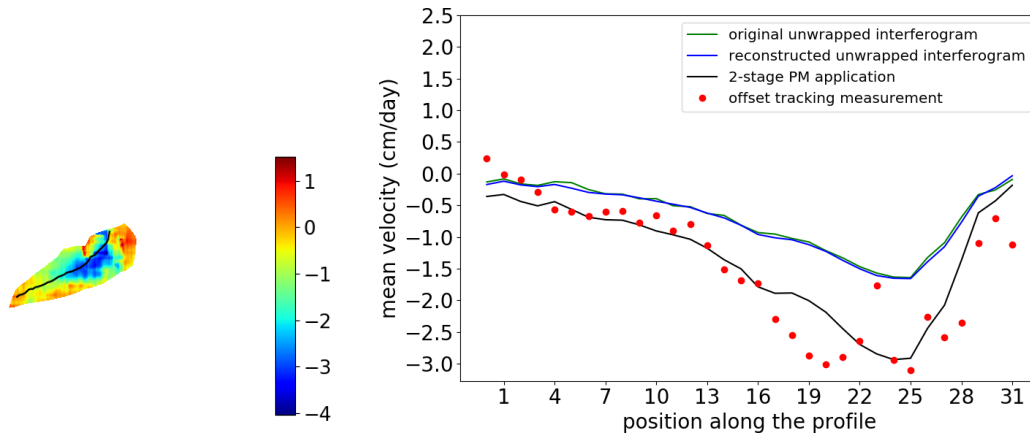


Figure 2.3 – (a) Mean velocity (cm/day) over the Gorner glacier obtained from 7 offset tracking measurements (from Sentinel-1 image pairs of 12-days interval) of good quality between 2016/11/29 and 2017/02/27 (b) Mean velocities on the profile indicated by a black line in (a) obtained from all original interferograms, reconstructed unwrapped interferograms, reconstructions of the two-stage application of the PM method and 7 offset tracking measurements of good quality (Prébet et al. (2019)).

Given the ability of the PM method to retrieve fringe patterns in the case of wrapped interferogram time series, a two-stage application of the PM method was implemented, that is, the PM method was first applied to the wrapped interferogram time series, phase unwrapping was performed on the reconstructed wrapped interferogram time series, then the PM method was applied a second time to the unwrapped interferogram time series. The results are shown in Figure 2.4 and a comparison with the mean velocity obtained from offset tracking measurements on a profile along the glacier is shown in Figure 2.3. The displacement pattern over the glacier is highlighted and regularised and most perturbations (both at small and large scales) in stable areas are filtered out on the reconstructed interferograms after the two-stage application of the PM method. Important displacement signals have been retrieved successfully on almost useless original interferograms and perturbations correlated at large scales have been filtered out efficiently, thanks to the application of the PM method to the wrapped interferogram time series. Then a second application of the PM method to the unwrapped interferogram time series further removes the artefacts, which results of uniform but not identical displacement fields.

Synthetic simulations

Besides the real data applications, the impact of some key parameters such as the displacement type, the time series size, the noise type, the signal to noise ratio (SNR) and the presence of unique events on the performance of the PM method have been investigated by means of synthetic simulations. The conclusions are reported in the following.

The PM method can retrieve most commonly observed displacement behaviors, including linear trend, acceleration/deceleration, intra-annual and inter-annual oscillations. In case of linear displacement, one EOF mode is sufficient to represent all the displacement information. Small time

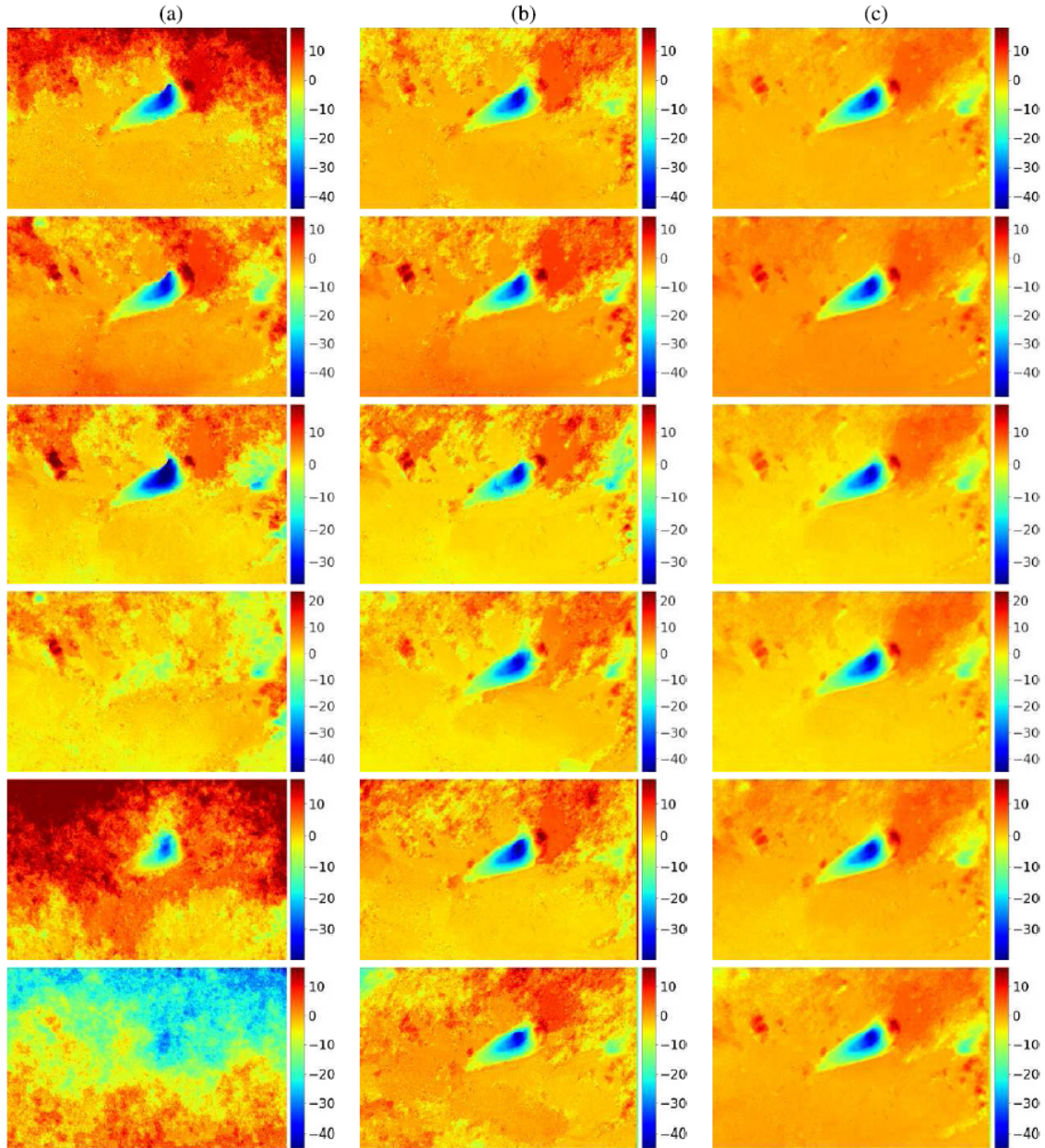


Figure 2.4 – (a) Original unwrapped interferograms (b) unwrapped interferogram of the PM wrapped reconstruction (c) reconstruction of the 2-stage PM method at time spans (from top to bottom) 2016/12/17 - 2016/12/23, 2016/12/29 - 2017/01/04, 2017/02/15 - 2017/02/21, 2017/03/11 - 2017/03/17, 2017/02/03 - 2017/02/09, 2017/03/05 - 2017/03/11) (Prébet et al. (2019)).

series is sufficient to correctly retrieve the displacement information. Whereas in case of oscillatory displacement, the displacement information is distributed over more EOF modes, with the number depending on the complexity of the displacement behavior. The appropriate time series size is the one that include all the oscillatory cycles. Longer time series does not degrade the quality of the retrieved displacement signal, but the error reduction rate is smaller.

The impact of the noise type on the performance of the PM method is significant. Random noise is uniformly distributed on the eigenvalue spectrum. Taking only the first EOF modes that represent the displacement can eliminate most random noise. Spatially correlated noise can be difficult to remove, because its distribution on the eigenvalue spectrum can be similar to that of the displacement. Taking the first EOF modes will also keep a large quantity of noise.

In the case of unwrapped interferograms, the error reduction is more significant in case of lower SNR; on the other hand, in the case of wrapped interferograms, the error reduction is more efficient in case of higher SNR. However, the benefit of the PM method is more important in the case of low and moderate SNR because the gain in accuracy in these cases is crucial to make useless data sets exploitable.

The impact of unique events on the performance of the PM method depends on the displacement type and the interferogram type. The impact is very small in the case of unwrapped interferograms of linear displacement. Compared to the case without unique events, the RMS errors are only increased for interferograms with unique events, even in case of as many as 50% of interferograms with unique events. In the case of either unwrapped interferograms of oscillatory displacement or wrapped interferograms of trend displacement, when the proportion of interferograms with unique events reaches as many as 25%, the RMS errors of other interferograms begin to increase, whereas in the case of wrapped interferograms of oscillatory displacement, the critical proportion of interferograms with unique events is 15%. Therefore, given a limited number of both unwrapped and wrapped interferograms with unique events, the reconstructions of other interferograms cannot be contaminated, and the efficiency of the PM method can, thus, be maintained.

2.3.3 Discussions

The PM method is a data-adaptive method that identifies the spatial patterns that vary together following a specific time function. Thereby, it can separate the coherent displacement signal and other perturbations in a displacement measurement time series, without any a priori information. For high SNR data sets, it behaves like a filter that denoises the displacement patterns, while for low SNR data sets, it can be considered as a gap filler that replaces the noise by coherent displacement signal based on the spatial and temporal correlation of the displacement.

It can be applied to both real valued unwrapped and complex valued wrapped interferogram time series. In case of unwrapped interferogram, the good performance of the PM method is obtained for interferograms with a minimum sufficient SNR. In case of wrapped interferogram, the PM method can even restore completely decorrelating fringe patterns. This difference in efficiency can be explained by the fact that, in the latter case, random decorrelating noise dominates the displacement signal in case of low SNR. Due to the randomness, the decorrelation noise does not introduce new variation directions in the ED/SVD analysis of the temporal covariance matrix. While in case of unwrapped interferogram time series, the spectrum of the spatially correlated noise is similar to that of the displacement signal, which can perturb the true variation directions in the ED/SVD analysis.

The PM method also presents some limitations. It is particularly suitable for measurement of continuous displacement over time (linear, with acceleration/deceleration, periodic, etc). In other words, primary variation modes must exist in the ED/SVD analysis of the temporal covariance. For significantly irregular displacement (e.g. intermittent or random displacement), the PM method may fail, due to lack of dominant variability in the time series. Moreover, in case of regular displacement, if high frequency displacement related to unique events exists in the time series, it

can be lost in the reconstruction. Further analysis on the residual will be necessary to retrieve this part of displacement.

Further development of the PM method consists of investigating the independent component analysis, which outperforms the principal component analysis in separating independent sources.

2.4 EM-EOF method

The EM-EOF method was proposed for missing data imputation in real valued displacement time series. It can be considered as a follow-up of the PM method presented previously.

2.4.1 Methodology

The EM-EOF method integrates the EOF-based analysis of the temporal covariance (presented in Section 2.2) into an EM-type resolution scheme, in order to gain more performance. The principle can be summarized in two steps (Figure 2.5). With an appropriate initialisation of missing values, the first step consists in estimating the optimal number of EOF modes for the reconstruction (denoted by R in the following) by minimizing the error between the validation data and the reconstructed time series. The second step updates the missing values iteratively following an EM algorithm, based on both the previous estimation of missing values and a new estimation of the optimal number of EOF modes according to the EOF analysis of the updated temporal covariance. In the EM algorithm, at step E, the missing data are fulfilled by the values obtained at the previous iteration and the temporal covariance is computed. At step M, the temporal covariance is decomposed in EOF modes and missing values are estimated with the optimal number of EOF modes determined according to the predefined criteria.

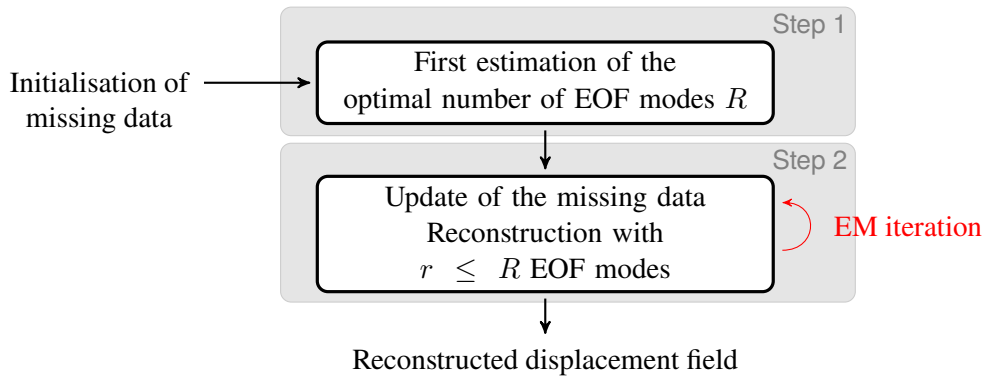


Figure 2.5 – Diagram of the two-step procedure of the EM-EOF method (according to Hippert-Ferrer (2020)).

Initialization of missing values

Initialization of missing values is essential, because it impacts the estimation of the temporal covariance matrix \hat{C} and thus the computation of the EOFs. As the initialization value is considered as a first estimate of the missing values, it is clear that it should be set in accordance to the distribution of the observed values. We can find several suggestions in the literature. For example, (Alvera-Azcarate et al. (2007), Schneider (2001)) proposed to use the spatial mean as initial values of the missing data to avoid any bias in the anomaly matrix (corresponding to zero in the anomaly). However, Beckers and Rixen (2003) have shown that an initial filling of missing values by the

spatial mean tends to decrease the variance of higher order modes by inversely increasing the variance of the dominant modes. Such an initial value tends to overwrite small scale information because it smooths the displacement field around missing data points. According to experiments performed in Hippert-Ferrer (2020), including the spatial mean, the spatial mean plus a random noise following a Gaussian distribution and the spatial mean plus a spatially correlated noise, no difference is observed in the final reconstruction and the selection of the optimal number of EOF modes. What changes with these initialization values is the computation time. Therefore, we propose to use the spatial mean as initial values of the missing data, since it is not always easy to characterize the noise present in the data.

Estimation of the optimal number of EOF modes

Similarly to Pr  bet et al. (2019), a cross validation error and the error reduction rate have been used as metrics to determine the optimal number of EOF modes. Note that the RMSD proposed in Pr  bet et al. (2019) is not used here, because the strategy of independent cross validation is adopted here and the RMS error is more intuitive compared to RMSD (at least for Alexandre).

The cross validation error, denoted by cross-RMSE, is the root mean square error of the reconstruction compared to the cross validation data. The cross validation data subset contains a predefined number of points randomly chosen in space and time among the existing data. These points are set as artificial missing data with their values put aside. After each reconstruction with a certain number, k , of EOF modes, the cross validation data set is compared to the new reconstruction. The number of cross validation points must be neither too small nor too large : a small number will not provide a good statistical representation of the data whereas a large number can affect the reconstruction error since the quantity of missing data is increased. Cross-RMSE is particularly useful when no ground truth or other source of information is available for validation of the results, the latter is often the case in displacement measurement.

In the case of a displacement signal perturbed by strongly correlated noise, the optimal number of EOF modes can be over-estimated. To deal with this issue, we use the error reduction rate defined as in equation 2.18, which gives a measure of the variation of the cross-RMSE when adding one more EOF mode.

$$\Lambda = 1 - \frac{\text{cross-RMSE}(k+1)}{\text{cross-RMSE}(k)} \quad (2.18)$$

A small variation (for example less than a value β) implies that only little information is added to the new reconstructed field. In this case, the added EOF mode is not considered in the reconstruction. If the data uncertainty is known, β can be determined such that the reconstruction uncertainty is consistent with the data uncertainty. If the uncertainty is unknown, β is determined empirically. According to repeated experiments in Hippert-Ferrer (2020), a value of 0.1 is often sufficient to select an optimal number of EOF modes.

2.4.2 Case study

Real data applications

The EM-EOF method was applied to the displacement time series obtained from consecutive Sentinel-1 A/B SAR images over the Gorner and Miage glaciers in the Mont-Blanc massif. For the Gorner glacier, 16 interferograms covering the period between November 2016 and March 2017 are used. Data gaps are spatially correlated, with quantities per interferogram varying from 11.8 % to 27.4 %. The time series also contains four missing interferograms due to total coherence loss. For the Miage glacier, there are 13 interferograms covering the period between December 2016 and March 2017. The quantity of data gaps varies from 11.4 % to 23.1 % and many interferograms are concerned with data gaps in the central part of the glacier. There are also three missing interferograms in this time series. Note that the long and narrow shape of the Miage glacier,

in addition to discontinuities due to coherence loss, make the phase unwrapping challenging : 5 interferograms out of 13 are concerned with phase jumps after the phase unwrapping. The correction of such phase jumps is difficult since no other data set with similar spatial coverage and measurement accuracy is available.

Examples of the reconstructed interferograms for the Gorner and Miage glaciers are shown in Figure 2.6 and Figure 2.7 respectively. The reconstructed displacement patterns are consistent with those observed in the original interferograms. In both cases, localised phase unwrapping errors present in the original interferogram have been corrected in the reconstruction. In Figure 2.6, the reconstruction of a missing interferogram is presented. This reconstructed interferogram is in agreement with other interferograms in terms of displacement pattern and global displacement magnitude, but further quantitative validation is impossible because of lack of other source of information. According to synthetic simulations performed to imitate this situation, the reconstructed missing interferograms are credible as long as they are not consecutive.

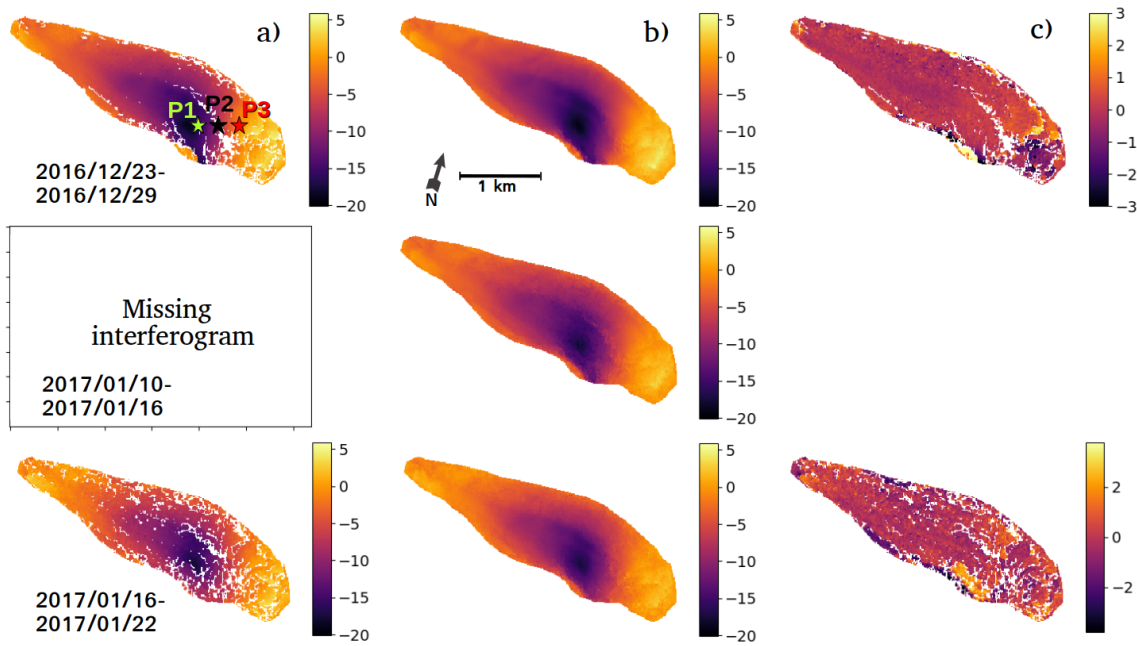


Figure 2.6 – Examples of (a) initial interferogram (b) reconstructed interferogram (c) residual (reconstruction - initial) over the Gorner glacier. Displacement values are in centimeters in the LOS direction (Hippert-Ferrer et al. (2020a)).

Examples of time series on arbitrarily chosen points over the Gorner glacier is shown in Figure 2.8 and those over the Miage glacier is shown in Figure 2.9. Similar observations are obtained with Figure 2.6 and Figure 2.7, which proves the efficiency of the EM-EOF method in both temporal and spatial dimensions.

For all these results, no absolute validation of the reconstruction was further realized, on one hand because of lack of other source of information, on the other hand because independent cross validation was performed in the method.

Synthetic simulations

Since there is no means to evaluate the accuracy of the EM-EOF method with real data, the first objective of synthetic simulations consists in assessing the accuracy of the EM-EOF method. Obviously, it depends on a lot of parameters such as SNR, quantity of data gaps, etc. A large number of experiments show that the accuracy of the EM-EOF method is comparable with the nominal uncertainty of the data set. For instance, for interferogram time series whose nominal uncertainty

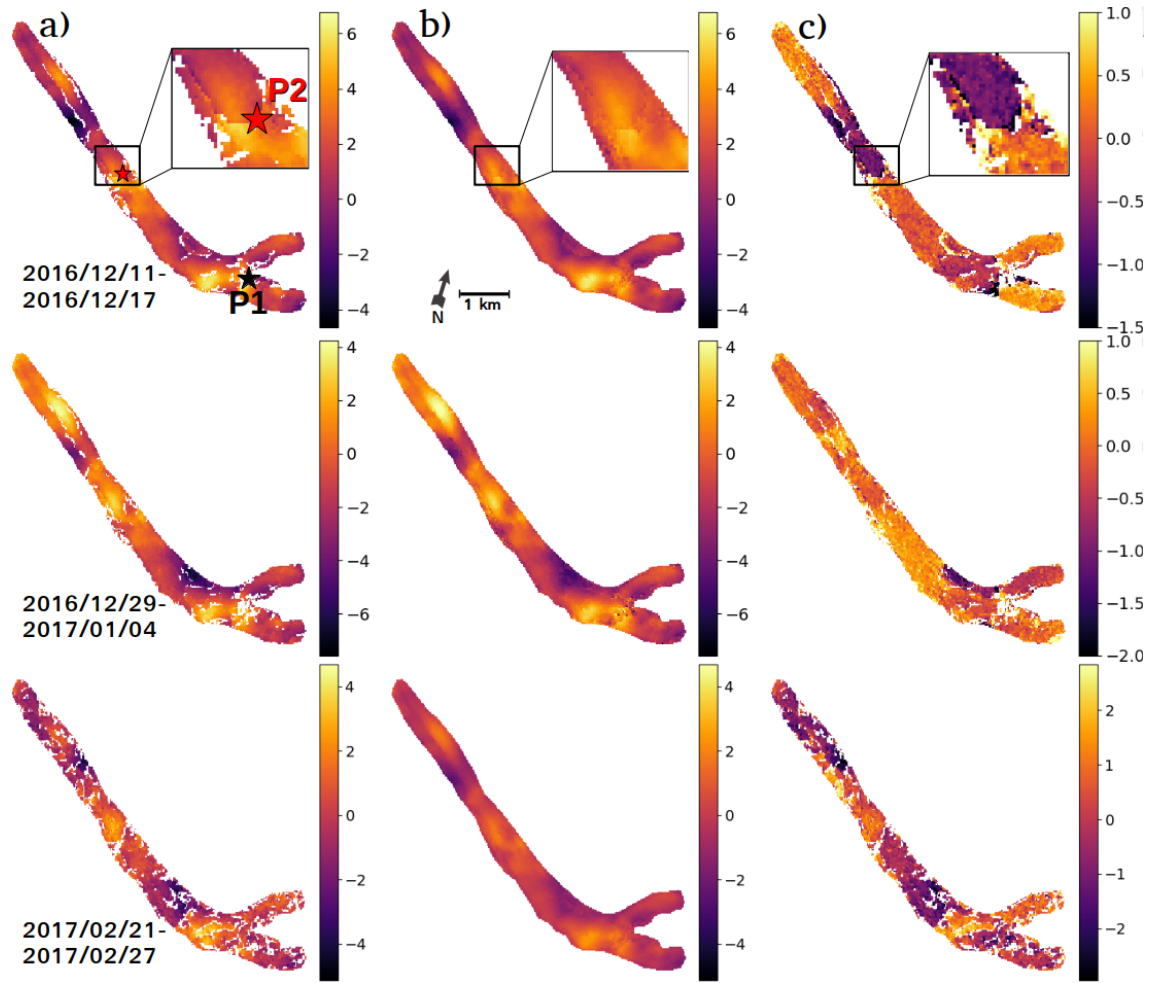


Figure 2.7 – Examples of (a) initial interferogram (b) reconstructed interferogram (c) residual (reconstruction - initial) over the Miage glacier. Displacement values are in centimeters in the LOS direction (Hippert-Ferrer et al. (2020a)).

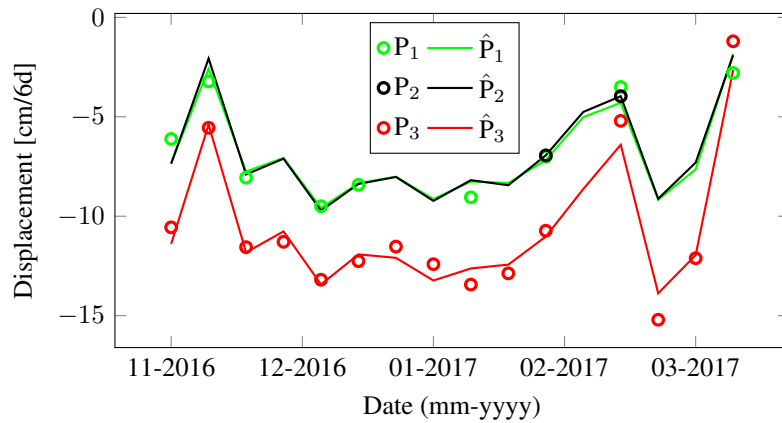


Figure 2.8 – Time series over locations P_1 , P_2 and P_3 (figure 2.6). Circles represent the original value and the lines represent the reconstructed value. The reconstructions follow the observations, even the abrupt fluctuations for example in mid-February 2017. The reconstruction over P_2 can be validated by the observations over P_1 which is located nearby (Hippert-Ferrer (2020)).

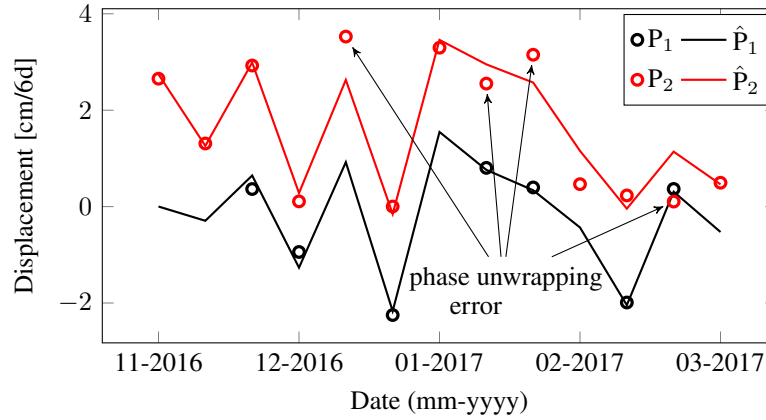


Figure 2.9 – Time series over locations P_1 , P_2 and P_3 (figure 2.7). Circles represent the original value and the lines represent the reconstructed value. Over the location P_2 , the discrepancy between the original values and the reconstructed values is mainly due to phase unwrapping errors in the original interferograms. (Hippert-Ferrer (2020)).

is on the order of centimeters, the accuracy of the EM-EOF method is centimeters, even better in numerous cases.

The sensitivity of the EM-EOF method to the type of displacement (linear, oscillatory, exponential, etc.), the SNR, the type of gaps (random and seasonal) and the type of noise (random, spatially correlated and spatio-temporally correlated, localized errors due to processing such as phase unwrapping) was also analyzed through synthetic simulations. The conclusions are in the following.

The EM-EOF method is robust against the type of displacement and the type of gaps. Displacement signal is observed in the residual only for displacement as complex as a combination of a linear trend and five oscillations with different frequencies. In most cases of Earth deformation, the displacement behavior is much less complex, there is thus no doubt on the efficiency of the EM-EOF method. No noteworthy difference in performance is observed between the random gaps and the seasonal gaps, except in case of large gaps ($> 70\%$) where the quality of the reconstruction with seasonal gaps is better than that with random gaps. This can be explained by the fact that large random gaps imply a high probability that missing data appear over the same point in successive measurements in the time series. Note also that in the case of exponential displacement behavior, the method is slightly less sensitive to large quantities of random gaps compared to correlated seasonal gaps.

Regarding the impact of the type of noise, similar to the observations for the PM method, it is sometimes difficult to separate the displacement signal and the correlated noise on the eigenvalue spectrum. Therefore, with the presence of correlated noise, the efficiency of the noise reduction of the EM-EOF method is degraded. In case of low SNR, it is possible that the estimation of the missing value is biased due to the high contribution of the correlated noise. In case of moderate SNR, as long as the displacement behavior is not biased, even if the reconstruction of missing data is still contaminated by correlated noise, it does not matter because the objective is to reconstruct the missing data in agreement with observed data that are subject to correlated noise. Notice also that, the minimum necessary SNR to guarantee the performance of the EM-EOF method is lower in case of random noise.

The impact of the SNR is obvious, if the displacement signal is buried in the noise, it is impossible to obtain a correct estimation of the displacement behavior. It has been observed that the performance of the EM-EOF method is more affected by SNR than by the quantity of gaps, except for large quantities ($> 60\%$). With 30% of data gaps for example, the quality of the reconstruction only depends on the SNR. Therefore, the EM-EOF method is robust against the

quantity of data gaps. Even in case of 50% data gaps, satisfactory results can still be obtained. However, note that in case of missing data in successive measurements in the time series, the reconstruction will follow the tendency of other points, which can provide good or biased result.

The ability of the EM-EOF method in filling in gaps in displacement fields with multiple objects, each presenting different behavior, was also investigated. A comparison between one reconstruction of the whole field and multiple reconstructions for each object has been performed. The one reconstruction strategy gave satisfactory results compared to the true field. Transitions between patterns are preserved, but it is possible that small displacement signal is found in the residual for some objects. Multiple independent reconstructions for each displacement pattern with different optimal number of EOF modes gave slightly better results : the displacement characteristics of each pattern are more preserved. Indeed, when the discontinuities between displacement patterns are relatively sharp, it is preferred to perform the reconstruction separately, particularly in case where displacement patterns are very different from one to another, which implies different number of optimal EOF modes for the reconstruction. When transition zones cannot be clearly identified (as in most cases of ground displacement fields), one reconstruction of the whole field is recommended to avoid possible discontinuities between displacement patterns.

2.4.3 Discussions

The EM-EOF constitutes the first missing data imputation method for displacement time series issued from optical or SAR images. Its ability in filling in gaps in displacement time series has been proven by both synthetic simulations and real data applications. It can deal with large data gaps, low or moderate SNR, multiple noise types and complex displacement behaviors.

The EM-EOF method works at 2 steps. Its first step indeed corresponds to the application of the PM method, with the main objective to get a first estimation of the optimal number of EOF modes to represent the data. At the second step, the PM method is applied iteratively to update the estimation of missing values, based on the previous estimation and a new EOF analysis of the updated temporal covariance matrix. The idea behind is to approach progressively to the true temporal covariance, starting from the initialisation more or less far away from the true value. With the improvement of the temporal covariance estimation step by step, the optimal number of EOF mode is also re-estimated at the second step. Therefore, compared to the PM method, the refinement proposed in the EM-EOF method provides a better estimation of the displacement behavior. The gain of iterative scheme proposed in the EM-EOF method with respect to a single EOF analysis proposed in the PM method deserves a quantification. Moreover, a cross validation strategy was proposed in order to ensure that the reconstructed missing values are in agreement with the observed values, which is very meaningful when the ground truth or other source of information is unavailable.

The EM-EOF method cannot reconstruct two successive missing interferograms : the reconstructions are the same for the two interferograms. On the other hand, all the interferograms reconstructed by the PM method are different, including those of successive acquisitions. That is why only a subset of the interferogram time series over the Gorner glacier used for the PM method was chosen for the application of the EM-EOF method. This difference is mainly related to the initialisation of missing data. On one hand, the same initialisation (i.e. temporal mean) is given to the two successive missing interferograms in the case of the EM-EOF method ; on the other hand, in the case of the PM method, coherence loss areas can be considered as data gaps because no useful information can be obtained, but there are indeed realistic noise values and possible displacement signals buried in the noise. It should be preferred to initialize missing values by the spatial or temporal mean plus a realistic noise in case of successive missing interferograms. This point has not been investigated thoroughly in the Ph.D thesis of Alexandre Hippert-Ferrer.

Finally, the EM-EOF method is an iterative method, but its implementation is not heavy at all. The computation time is case dependent, but the dimension of the temporal covariance depends

on the time series size which is small in most cases. In case of a time series of 40 displacement fields of dimension 5000×5000 , the execution time is 8 min on a classical laptop (Intel Xeon E5-2650 v3 à 2.3 GHz). As a result, the EM-EOF method can be considered as a processing step in an operational processing chain.

2.5 Extended EM-EOF method

The extended EM-EOF method constitutes an extension of the previously presented EM-EOF method. The methodological increment consists of the utilization of the spatio-temporal covariance, instead of the temporal covariance of the displacement time series. Compared to the EM-EOF method, this method is capable of dealing with cases when 1) the spatial correlation dominates the temporal correlation 2) only small time series (e.g. around 10 interferograms in the time series) is available 3) same missing areas exist in successive displacement field in the time series.

2.5.1 Methodology

The extended EM-EOF method follows the principal of the EM-EOF method, i.e. integrating the EOF-based analysis of the spatio-temporal covariance into an EM-type resolution scheme. Similarly, after the initialisation of missing values, it works at two steps. At the first step, we get a first estimation of the optimal number of EOF modes. The missing data are estimated and updated in an iterative way following an EM algorithm at the second step. At the end of the second step, a refinement of the optimal number of EOF mode is realized, based on a confidence index estimated from the uncertainty of eigenvalues.

Estimation of spatio-temporal covariance

Let \mathbf{X}_t be a spatial grid of size $P_x \times P_y$ observed at time $t = 1, \dots, N$, where each element at position (i, j) is noted $x_{ij}(t)$, $1 \leq i \leq P_x$, $1 \leq j \leq P_y$. All observations of \mathbf{X}_t are stacked into a spatio-temporal data matrix $\mathbf{Y} = (\mathbf{X}_1, \mathbf{X}_2, \dots, \mathbf{X}_N)$. Note that in practice each \mathbf{X}_t has zero mean, i.e. its spatial mean is removed.

Each \mathbf{X}_t is augmented into a Hankel-block Hankel (HbH) matrix \mathbf{D}_t of size $K_x K_y \times M_x M_y$, with $K_x = (P_x - M_x + 1)$, $K_y = (P_y - M_y + 1)$ and where (M_x, M_y) is a two-dimensional window sliding through each \mathbf{X}_t (see Figure 2.10) :

$$\mathbf{D}_t = \begin{pmatrix} \mathbf{H}_{1,t} & \mathbf{H}_{2,t} & \dots & \mathbf{H}_{M_x,t} \\ \mathbf{H}_{2,t} & \mathbf{H}_{3,t} & \ddots & \vdots \\ \vdots & \ddots & \ddots & \vdots \\ \mathbf{H}_{K_x,t} & \dots & \dots & \mathbf{H}_{P_x,t} \end{pmatrix} \quad (2.19)$$

Each matrix $\mathbf{H}_{i,t}$ is a $K_y \times M_y$ Hankel matrix defined as :

$$\mathbf{H}_{i,t} = \begin{pmatrix} x_{i1}(t) & x_{i2}(t) & \dots & x_{i,M_y}(t) \\ x_{i2}(t) & x_{i3}(t) & \ddots & \vdots \\ \vdots & \ddots & \ddots & \vdots \\ x_{i,K_y}(t) & \dots & \dots & x_{i,P_y}(t) \end{pmatrix} \quad (2.20)$$

In the following, we note $K = K_x K_y$, $M = M_x M_y$ and $P = P_x P_y$ for the sake of convenience. Similarly to \mathbf{Y} , each matrix \mathbf{D}_t is stacked into a spatio-temporal matrix \mathcal{D} of size $(K \times NM)$, that is $\mathcal{D} = (\mathbf{D}_1, \mathbf{D}_2, \dots, \mathbf{D}_N)$.

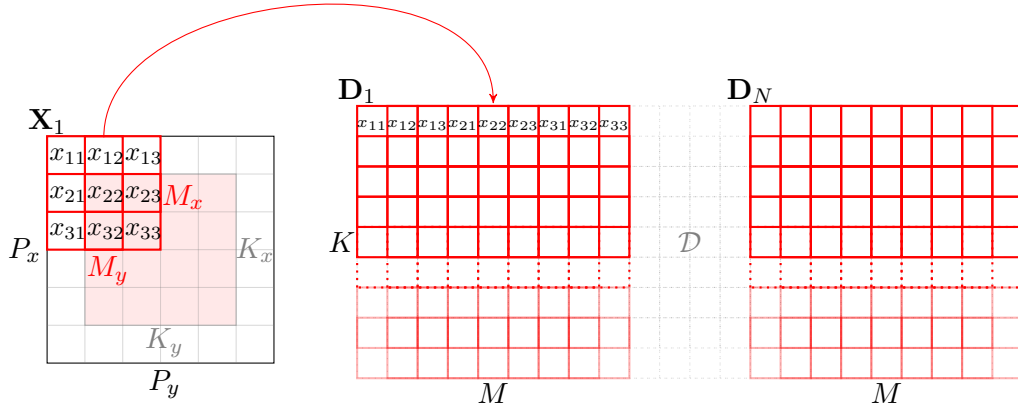


Figure 2.10 – Illustration of the estimation of the spatio-temporal covariance with help of a sliding window $M_x \times M_y$. The field \mathbf{X}_1 is augmented to a matrix \mathbf{D}_1 of dimension $K_x K_y \times M_x M_y$, which is stocked in a large spatio-temporal matrix \mathcal{D} . Each \mathbf{D}_t corresponding to \mathbf{X}_t is then ordered in line, which results of a matrix of dimension $(K \times NM)$ (Hippert-Ferrer (2020)).

With reference to the literature in Multivariate Singular Spectral analysis (M-SSA) (Broomhead and King (1986), Ghil et al. (2002)), \mathcal{D} is called an augmented data matrix. The difference here is that each \mathbf{X}_t is augmented spatially and not temporally. The one-dimensional window of size M used in M-SSA to augment a time series is now a two-dimensional window of size $M_x \times M_y$ as in Golyandina and Usevich (2010). The augmented matrix is therefore spatio-temporal in the sense that its structure is an alternation of temporal blocks within which augmented spatial blocks are nested.

In the following, the sample covariance of the augmented data matrix, \mathcal{D} , is formed by

$$\hat{C} = \frac{1}{K} \mathcal{D}^T \mathcal{D} \quad (2.21)$$

where \hat{C} is a symmetrical and positive definite matrix of size $NM \times NM$.

Determination of the spatial lag

The choice of the spatial lag, M , is generally determined by a trade-off between the amount of information extracted in the window (M should be large) and the number of repetitions of the window within each image (M should be small) (Groth and Ghil (2015)). Instead of a single value, a range of M can provide satisfactory results. We explored two metrics to determine the range of M . The first metric is based on the covariance estimation theory, that is, the number of independent samples should be at least twice the number of variables. Thus, the maximum value of M can be determined by solving $K > 2M$. Simple calculations lead approximately to $M < P/6$. The

second metric is based on the spatial auto-correlation property of the displacement field. Let τ be the spatial decorrelation decay defined as $\tau = -\frac{\Delta P}{\log r}$, where r is the lag-one auto-correlation and ΔP is the spatial sampling rate, here 1 pixel. Following Ghil et al. (2002), M can be approximated by $M \simeq P/\tau$. In most cases, r is supposed to be smaller than 0.95, which gives $M > P/20$.

Estimation of the optimal number of EOF modes

Because of the complex structure of the spatio-temporal covariance matrix, the structure of the eigenvalue spectrum can be complicated, which makes the determination of the optimal number of EOF modes more difficult. Besides the cross-RMSE and the error reduction rate proposed previously (which can be limited in the case of degenerate eigenvalues), we proposed furthermore a confidence index associated with the eigenvalue uncertainty.

Degeneracy (close eigenvalues) and/or separation (distant eigenvalues) in the eigenvalue spectrum provides useful information on both signal frequencies distribution and spatio-temporal variability. Degeneracy of eigenvalues makes the interpretation of the corresponding EOFs difficult. Two or multiple consecutive eigenvalues (called multiplet thereafter) are degenerate when the uncertainty of an eigenvalue is comparable with or larger than the spacing between this eigenvalue and its closest neighbor. Therefore, to investigate multiplet degeneracy, the uncertainty of eigenvalues must be first estimated. North et al. (1982) proposed a "rule of thumb" to approximate the eigenvalue uncertainty :

$$\Delta\lambda_k \approx \sqrt{\frac{2}{L^*}} \lambda_k \quad \Delta\mathbf{u}_k \approx \frac{\Delta\lambda_k}{\lambda_j - \lambda_k} \mathbf{u}_j \quad (2.22)$$

where λ_j is the closest eigenvalue from λ_k , \mathbf{u}_j , \mathbf{u}_k are the corresponding eigenvectors, L^* is the number of independent observations in the spatio-temporal samples also called effective sample size (named ESS hereafter). The interpretation of equation (2.22) is the following : if the uncertainty of eigenvalue λ_k is close to the difference between this eigenvalue and its closest neighbor, then the corresponding eigenvectors are likely to be contaminated one by each other. This contamination exists when, for example, two eigenvectors describe together the same spatio-temporal pattern or if the signal is perturbed by correlated noise, which has the effect of "spreading" the variance over the spectrum. To estimate the spatio-temporal ESS L^* , we separate it into two distinct parts such that $L^* = N^*M^*$. N^* corresponds to the temporal ESS and M^* to the spatial ESS. Thiébaux and Zwiers (1984) have given an estimation of N^* by $N[1 + 2\sum_{k=1}^{N-1}(1 - \frac{k}{N})\rho(k)]^{-1}$, where $\rho(k)$ is the auto-correlation of the time series and N is the number of observations in time. This definition holds for a univariate time series of N observations, e.g. a pixel value varying over time. Following this definition, we estimate the spatial ESS M^* within each spatial window of size M by

$$M^* = M \left(1 + 2\nu \sum_{k=1}^M \left(1 - \frac{k}{M} \right) \right)^{-1} \quad (2.23)$$

where $\nu = \frac{1}{N} \sum_{t=1}^N I_t$ is the average spatial auto-correlation and I_t is the Moran's I statistics of spatial field \mathbf{X}_t .

Based on the estimated uncertainty of eigenvalues given in equation (2.22), a measure of confidence \mathcal{C}_k associated with each eigenvalue λ_k can be computed in the $[0, 1]$ interval :

$$\mathcal{C}_k = \frac{\max(\Gamma_k) - \Gamma_k}{\max(\Gamma_k) - \min(\Gamma_k)} \quad k = 1, \dots, NM \quad (2.24)$$

with $\Gamma_k = \log \left(\frac{\Delta\lambda_k}{\lambda_j - \lambda_k} \right)$.

\mathcal{C}_k allows to detect degeneracy and/or separation of the eigenvalues in the spectrum of \mathcal{D} , which respectively corresponds to lower and higher values of \mathcal{C}_k . That is, the peak in \mathcal{C}_k corresponds to

a separation between two eigenvalue multiplets whereas lower "sidepeak" values correspond to degeneracy of a multiplet or close eigenvalues.

To refine the optimal number of EOF modes R previously determined using the cross-RMSE and the error reduction rate, \mathcal{C}_k is computed for $k = 1, \dots, MN$. Then, the peaks in \mathcal{C}_k corresponding to the separations in the eigenvalue spectrum are detected. If R corresponds to a peak of \mathcal{C}_k , the algorithm stops here. Otherwise, if the subsequent \mathcal{C}_k is high enough (e.g. $\mathcal{C}_k \geq 0.8$), the optimal number is updated so that it matches the subsequent index k .

Reconstruction of the displacement time series

Different from the EM-EOF method, the direct reconstruction after the eigenvalue decomposition gives the augmented data matrix \mathcal{D} in which redundancy of the original displacement points exists. In order to obtain the reconstructed displacement time series, an average on the diagonals called hankelization, is applied on each matrix $\mathbf{H}_{i,t}$ and \mathbf{D}_t ,

$$x_{ik}(t) = \frac{1}{\#\mathcal{A}_k} \sum_{(l,l') \in \mathcal{A}_k} x_{ll'}(t) \quad (2.25)$$

$$\mathbf{H}_{k,t} = \frac{1}{\#\mathcal{B}_k} \sum_{(l,l') \in \mathcal{B}_k} \mathbf{H}_{ll',t} \quad (2.26)$$

where $\mathcal{A}_k = \{(l, l') : 1 \leq l \leq K_y, 1 \leq l' \leq M_y, l + l' = k + 1\}$ et $\mathcal{B}_k = \{(l, l') : 1 \leq l \leq K_x, 1 \leq l' \leq M_x, l + l' = k + 1\}$. This implies that the average is performed on each block of $\mathbf{H}_{i,t}$, then entirely on $\mathbf{H}_{i,t}$ (Golyandina and Usevich (2010)), which is consistent with the Hankel's bloch structure.

Therefore, compared to the EM-EOF method, an averaging in the final reconstruction of the displacement time series exists, and this averaging behaves as a low-pass filter.

2.5.2 Case study

Real data application

The extended EM-EOF method is applied to surface velocity data obtained from offset tracking of Sentinel-2 images over the Fox glacier in New Zealand (Millan et al. (2019)). The data set consists of a time series of 12 velocity fields covering the period from February to mid-September in 2018. The dimension of each velocity field is 100×150 pixels. All velocity fields contain missing data, with quantity varying from 10% to 60%. Data gaps correspond to discarded values due to low correlation or outliers. The number of cross-validation points, which are randomly chosen, is set to 1% of the observed points per velocity field. The spatial lag is fixed to $M = 225$ (window of size 15×15), which, considering the quantity of points over the glacier, roughly corresponds to the lower limit of the lag.

In the original displacement time series, data gaps are significant especially in the lower part of the glacier (left upper part on the Figure 2.11). A seasonal variation of the velocity has been identified over some locations (e.g. P1) where velocity measurement is available most of the time in a previous study (Millan et al. (2019)). In the upper part of the glacier (right lower part on the Figure 2.11), spike velocity values can still be observed even after the thresholding and this kind of values is common in offset tracking measurements. Obviously, the large data gaps hinder the full understanding of the displacement behavior over the whole glacier, in which case gap filling is of particular importance. The reconstructed velocity fields (Figure 2.12) present smooth displacement patterns, but with the seasonal variation retrieved. The maximal velocity value reaches 1500 m/year in the lower part of the glacier, a narrow and hanging area where acceleration is observed. This observation is consistent with Herman et al. (2011) and Kääb et al. (2016)). A detailed inspection

over selected locations (P1, P2 and P3 in Figure 2.11) further confirms the efficiency of the extended EM-EOF method. Similar evolution tendency has been reconstructed over P1, P2 and P3 and this observation remains over the whole glacier, including both observed areas and missing data areas. A comparison with the EM-EOF method demonstrates an accuracy gain on the order of 15 m/year on average over these locations.

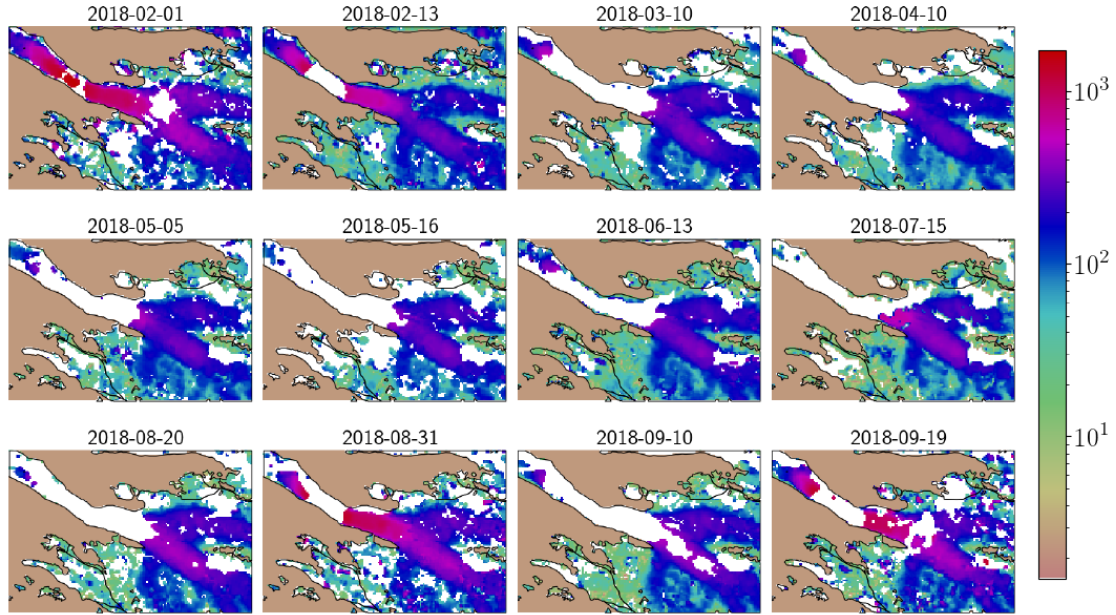


Figure 2.11 – Original velocity (m/yr) time series between February and September 2018 over the Fox glacier, obtained by offset tracking of Sentinel-2 optical images (Hippert-Ferrer et al. (2020b)).

Synthetic simulations

Synthetic simulations have been performed to assess the efficiency of the extended EM-EOF method compared to the EM-EOF method in case of small time series, as well as to highlight the sensitivity of the extended EM-EOF method to key parameters such as SNR, noise type, quantity of data gaps. The conclusions are reported in the following.

In case of small time series (~ 10), the displacement patterns can be retrieved correctly by both methods, but the extended EM-EOF method generally gives smoother displacement field and smaller RMS errors compared to the EM-EOF method. This smoothness is mainly due to the average step in the final reconstruction of the displacement time series from the augmented data matrix. However, in most synthetic experiments, it is observed that the residual of the EM-EOF reconstruction is more similar than that of the extended EM-EOF reconstruction to the spatially or spatio-temporally correlated noise added to the displacement signal. This implies that more correlated noise, whether spatially or spatio-temporally, is kept in the reconstruction of the extended EM-EOF method. The average step in the latter method is not sufficient to reduce the correlated noise. Indeed, because of the complex structure of the spatio-temporal covariance in the case of the extended EM-EOF, much more EOF modes are retained in the reconstruction, which results of more correlated noise in the reconstruction. Consequently, the simpler the displacement behavior is, the less EOF modes are retained, thus the less correlated noise is present in the extended EM-EOF reconstruction.

The sensitivity to SNR, data gaps and noise of the extended EM-EOF is similar to that of the EM-EOF method. Its efficiency degrades with increasing data gaps and decreasing SNR. The impact of the SNR is more important than that of the data gaps. The benefit, in other words the

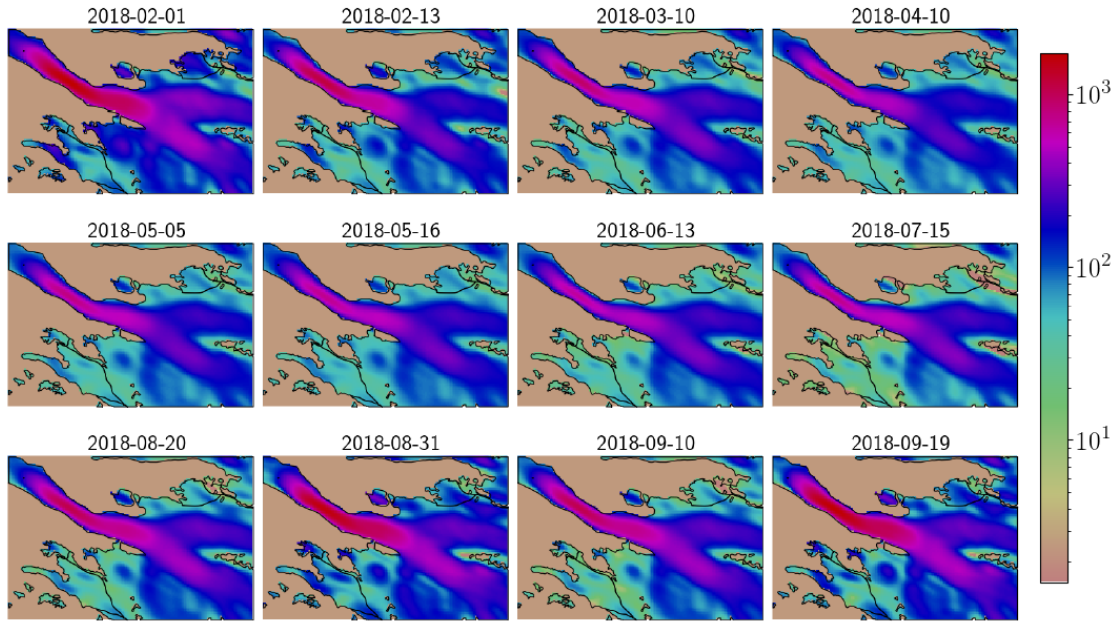


Figure 2.12 – Reconstructed velocity (m/yr) time series in Figure 2.11 by the extended EM-EOF method (Hippert-Ferrer et al. (2020b)).

error reduction rate, is particularly significant in case of low to moderate SNR (0.7 - 2) and large data gaps (30% - 70%).

2.5.3 Discussions

The extended EM-EOF method is capable of filling in gaps in small time series with large quantity of data gaps. Besides the temporal correlation, taking the spatial correlation into account by creating small subset of spatial samples allows for better reconstructions according to both synthetic simulations and real data applications. The benefit is three-fold : 1) the spatio-temporal correlation provides a better constraint to the reconstruction than the temporal correlation. 2) the spatial window used in the augmentation of the data matrix reduces the analysis to a relatively homogeneous subset rather than an entire displacement field, thus avoids potential bias in the estimation of the covariance matrix. 3) The averaging step in the final reconstruction allows for a further gain in accuracy. However, note that in case of spatially or spatio-temporally correlated noise, more noise is kept in the reconstruction by the extended EM-EOF method. The averaging step cannot always be efficient to remove this noise. Remind also that the gain in accuracy compared to the EM-EOF method is case dependent. In many cases, the gain is comparable with the nominal accuracy of the original displacement measurement.

Despite the slightly higher performance of the extended EM-EOF method, one drawback consists of the computational burden. The complexity of the algorithm is much increased, which results of longer computation time and larger requirement of memory. According to the experiments in the Ph.D thesis of Alexandre Hippert-Ferrer, in case of long time series or moderate SNR or intermediate data gaps, the EM-EOF method is sufficient to provide satisfactory results, because the gain in accuracy of the extended EM-EOF method in these cases is limited. While in case of small time series, especially with low SNR and large data gaps, it is preferred to apply the extended EM-EOF method, in spite of the heavy computational load.

2.6 Conclusions & perspective

Towards parametric methods for missing data imputation

Indeed, the development of the EM-EOF method and the extended EM-EOF method was more application driven than method driven. In other words, the emphasis was on the resolution of the interpolation problem encountered in displacement time series, no particular focus was made on data distributions and the hypotheses behind the statistical theory. For example, the sample covariance matrix is considered as an estimator of the true covariance in both EM-EOF method and its extension without considering the data distribution, whereas this is only appropriate for data following a Gaussian distribution. Although promising results have been obtained, it is clear that these methods can give sub-optimal results for some data sets and more importantly this way does not allow for further methodological development. Therefore, we intend to propose a new paradigm that aims to tackle the problem of missing data in the broad sense from a statistical point of view, independent of the application. This paradigm requires modeling the data statistic by means of a probability distribution function, formulating hypotheses on the statistical model and estimating the statistical parameters on which the distribution depends. Since we can use the estimated statistical parameters to describe, analyze and predict the variability of the data under consideration, it is possible to deal with any type of data with this kind of approaches.

Therefore, instead of a direct estimation of missing data as in EM-EOF and extended EM-EOF methods, the main objective is to estimate one or several parameters (e.g. mean, covariance or higher order statistics) of the statistical model that describes the data distribution. The missing data can then be retrieved from the estimated parameters. The methods to further develop, namely parametric approaches, consist of estimating the covariance matrix directly from the observed data without initialisation of missing data. The estimator of the covariance, which depends on the data distribution, can be approached in an EM scheme. For data following a Gaussian distribution, maximum likelihood estimator for covariance estimation has been widely reported in statistical signal processing (Little and Rubin (2002), Liu (1999)). A few works can also be found either to deal with non Gaussian distributions (Frahm and Jaekel (2010), Liu and Palomar (2019)) or to take a low rank structure of the covariance matrix into account (Chen et al. (2009)). To the best of our knowledge, no work has so far been published to deal with non Gaussian distributions and constraints on the structure of the covariance matrix at the same time. Given the fact that it is really infrequent that SAR/optic derived displacement time series follow a Gaussian distribution, a particular focus will be set to non Gaussian statistics, considering the inherent structure of the covariance matrix (e.g. low rank, toeplitz, etc.) of SAR displacement time series.

Alexandre has already started to work on this subject at the end of his Ph.D thesis, preliminary results obtained confirmed the consistency between the previously developed EM-EOF and extended EM-EOF methods and the parametric approach in case of Gaussian distributions. The retrieval of missing data from the estimated covariance matrix still remains an open question in his Ph.D thesis. Future works of robust estimation of the covariance matrix for non Gaussian data distribution and its recursive implementation constitute the subject of a task in my ANR young research project.

3

Explore displacement measurements time series

3.1 Introduction

With the increasing availability of satellite SAR and optical images, in particular, the launching of Sentinel 1 and 2 satellites that provide regular and free access acquisitions over the whole world, the quantity of displacement measurements produced by multi-temporal InSAR and offset tracking approaches reach an unprecedented volume. Displacement measurements time series are often further exploited for detection and classification purposes in order to give detailed insights into the displacement behaviors at different scales. The vast data stream thus requires enhanced processing techniques that are accurate, robust and fast. The questions, how to efficiently explore these large displacement data sets for timely displacement information delivery, or how to appropriately combine these large displacement data sets in order to further improve the reliability and to facilitate the interpretation by end users, arise.

In case of small displacement measured by multi-temporal InSAR approaches, as shown in Chapter 1, whatever is the interferometric network exploited, a single reference (SR) displacement time series is often estimated (by retrieving the phase consistency in the temporal dimension) as the final product, with the latter keeping the essential displacement information provided by the whole SAR image stack, but being much easily interpretable. The major shortcoming of these approaches is that they are applied on a pixel-by-pixel basis and ignore the known spatial correlation in the displacement observations. Therefore, further improvement concerns the synergistic exploitation of both spatial and temporal relationships of displacement instead of dealing with individual spatial points separately through a temporal model as done in most multi-temporal InSAR approaches. Moreover, efficient integration of newly arriving displacement measurements in a dynamical framework constitutes another research direction in line with the operational monitoring of displacement measurements.

In case of large displacement measured by offset tracking of optical or SAR images, depending on the SAR/optical image network formed, a large amount of displacement measurements of diverse temporal baselines, of different quality in terms of uncertainty and incompleteness, providing both redundant and complementary displacement information can be obtained in most cases. Of course, we can estimate a SR offset time series as the final product, as done in multi-temporal InSAR approaches. For example, Casu et al. (2011) proposed a namely PO-SBAS approach to estimate a SR offset time series from small baselines offset measurements, following the idea of the SBAS approach. However, it is not always appropriate, in this case, to follow the multi-temporal InSAR processing because of different data characteristics. Large data gaps can exist in individual offset

measurement (due to the inefficiency of the offset tracking algorithm or thresholding according to the reliability of the estimated displacement values) and the quality of each offset measurement can be significantly different from one to the others. For instance, the signal-to-noise ratio (SNR) of offset measurement of small temporal baselines (smaller displacement) is generally weaker than that of longer temporal baselines (larger displacement), because of the moderate accuracy of the offset tracking technique. Moreover, data inconsistency often occurs due to lack of efficient quality indicator of the offset tracking results. Therefore, methodological development (in the sens of data fusion) still seems necessary to extract displacement information of better quality and easily interpretable from a large amount of offset measurements of different characteristics.

Indeed, displacement data fusion problem exists since a long time, even before the expansion of the time series. In Yan et al. (2016), a review was given to present early displacement measurements fusion approaches to improve the measurement accuracy, to increase the spatial extension and to estimate displacement information at a higher level (e.g. 3D displacement, geophysical parameters, etc.). Obviously, the previously proposed approaches seem partly or completely out of date. In this chapter, I will present the actual state-of-the-art approaches for displacement time series analysis, with more focus on displacement fusion approaches and make a comment on these approaches. I will also give my personal insights into the possibility of application and further development of these state-of-the-art approaches in an operational context.

In the following, I begin with the standard least-square inversion approach. Open issues related to this approach such as the choice of weighting functions, the consideration of correlation in measurements and the choice of temporal baselines are discussed. Then, the multi-scale InSAR time series analysis approach, the spatio-temporal random effect model, the Kalman Filter based InSAR time series analysis, the Median of Multiple Common Master Series approach, and machine learning approaches are presented in order. Besides the essential technical details, the potentials and drawbacks of each approach are also discussed.

3.2 Least-square inversion

3.2.1 3D displacement estimation

The 3D displacement estimation constitutes an important subject in SAR displacement measurements exploration (Hu et al. (2017), Liu et al. (2018), Wright et al. (2001), Yan et al. (2013)). As is known, InSAR and offset tracking techniques provide displacement measurements in the geometry of SAR image acquisition, this increases the difficulty in displacement interpretation and comparison with other sources of information for non experts who are not familiar with SAR geometries. The common approach is thus to estimate the 3D displacement from displacement measurements in different directions (i.e. range and azimuth directions, different incidence angles) issued from InSAR and offset tracking. The problem is resolved through a linear geometrical model expressed as follows,

$$r = Pu \quad (3.1)$$

where r denotes the vector of displacement measurements from InSAR and offset tracking, u is the vector of 3D displacement to estimate, P is the projection matrix depending on the incidence angle (θ) and the heading angle (ϕ , the angle between the direction of the satellite trajectory and the North, e.g. -167° in descending pass and -13° in ascending pass for Sentinel-1 data), with

$$P_{LOS} = \begin{pmatrix} -\cos\phi\sin\theta & \sin\phi\sin\theta & -\cos\theta \end{pmatrix} \quad (3.2)$$

$$P_{az} = \begin{pmatrix} \sin\phi & \cos\phi & 0 \end{pmatrix} \quad (3.3)$$

The least-square solution is given by

$$u = (P^T \Sigma_r^{-1} P)^{-1} P^T \Sigma_r^{-1} r \quad (3.4)$$

with Σ_r the error covariance of displacement measurements r . In many cases, a diagonal matrix is used for the sake of simplicity, assuming independence of each displacement measurement. In case of measurements sharing the same reference/secondary images, the latter assumption cannot be verified any more, but there is no clear correlation quantification that can be found in the literature.

Since u is a vector with three components, there should be displacement measurements in at least three directions in r . In case of InSAR displacement measurements with different incidence angles, only two components, i.e. East-West and vertical components, can be estimated.

Through equation 3.4, a large number of displacement measurements are transformed to a single 3D displacement measurement. Besides the ease of interpretation and comparison, another main interest lies on the reduction of the uncertainty. The uncertainty of the 3D displacement obtained is smaller than that of any displacement measurement in r . In case of random uncertainty, the more the number of displacement measurements used, the smaller the uncertainty of the 3D displacement. Therefore, the use of all available displacement measurements (namely joint inversion hereafter) is preferred in this case. However, in case of systematic uncertainty (e.g. a ramp, a constant shift, etc.), the relationship between the uncertainty of the 3D displacement and the number of displacement measurements used is not so linear any more. Other fusion strategy should be considered.

In Yan (2011), two fundamental fusion strategies, joint inversion and pre-selection (use just part of the available displacement measurements, e.g. those of the best quality), have been explored with two kinds of uncertainty modeling, probability distribution and possibility distribution (i.e. triangular distribution) (Yan et al. (2012b)). The probability distribution is most appropriate for modelling random uncertainties, while the possibility distribution provides a unified representation of both random uncertainty and systematic uncertainty, without any hypothesis about the uncertainty characteristics and independence. In the latter case, instead of a vector of three components to estimate, three possibility distributions are estimated through fuzzy algorithms

$$u = (P^T \Sigma_r^{-1} P)^{-1} P^T \Sigma_r^{-1} \otimes r \quad (3.5)$$

with \otimes represents the fuzzy multiplication matrix operator in which the sum and scalar product operators are replaced by corresponding fuzzy operators.

The results obtained in the case of the Kashmir 2005 earthquake (Figure 3.1) show that the choice of the fusion strategy depends on the type of uncertainty to reduce and the data quality. In the conventional approach with probabilistic modeling of uncertainty, joint inversion can reduce to the maximum the uncertainty, except in the case where few displacement measurements of good quality are available. In the latter case, pre-selection and joint inversion give similar results but pre-selection is less computational expensive. In the approach with possibilistic modeling of uncertainty, adding more displacement measurements cannot reduce the uncertainty, sometimes, even increase it, the strategy of pre-selection is thus preferred. Indeed, the probabilistic modeling is somehow optimistic while the possibilistic modeling is pessimistic. In most real cases where both random and systematic uncertainty are present, the uncertainty of 3D displacement estimation provided by the probabilistic modelling can be considered as a lower bound, while that provided by the possibilistic modeling as a higher bound. The real uncertainty should be situated in between. The more the hypothesis of randomness and independence is justified, the closer to the uncertainty provided by the probabilistic modeling; otherwise, the closer to the uncertainty provided by the possibilistic modeling.

3.2.2 Displacement time series fusion

Theoretically, from N SAR or optical images, $N(N - 1)/2$ displacement measurements can be obtained, considering the all combination network presented in Chapter 1 (Figure 1.2 (d)). The

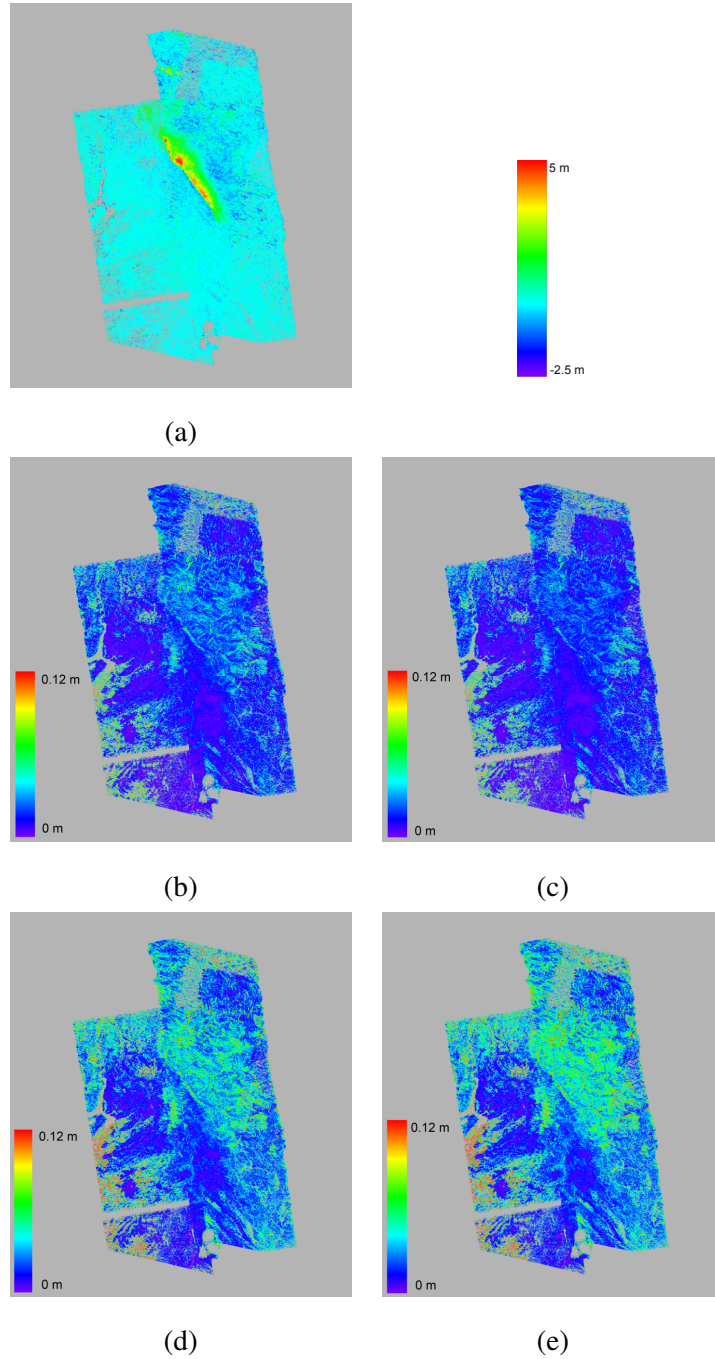


Figure 3.1 – (a) Vertical component of the 3D displacement induced by the Kashmir 2005 earthquake obtained from a least square inversion of InSAR and offset tracking displacement measurements. Probabilistic uncertainty in (b) pre-fusion and (c) joint inversion. Possibilistic uncertainty in (d) pre-fusion and (e) joint inversion (Yan (2011)).

first method, simple but efficient, consists of estimating a SR displacement time series through a linear equation system (equation 3.6) by retrieving the temporal closure (equivalent to the phase consistency presented in Chapter 1).

$$Ax = y \quad (3.6)$$

where x is the vector containing the SR displacement measurements, y is the vector containing all available displacement measurements. A is a design matrix, with 0 and 1 as values.

The least square solution is given by

$$x = (A^T \Sigma_y^{-1} A)^{-1} A^T \Sigma_y^{-1} y \quad (3.7)$$

where Σ_y is the error covariance of y , from which different measurements in the vector y are weighted in the inversion. A diagonal matrix is often considered for Σ_y , assuming independence between different measurements, which can be true in most cases. This matrix can also be replaced by other types of weighting matrix.

In case of disconnected subsets, $A^T \Sigma_y^{-1} A$ has a rank deficiency, the inverse problem is thus ill-posed. The common solution consists of using a SVD pseudo-inversion. Indeed, without connectivity, it is impossible to reconstruct a common temporal displacement history between disconnected subsets. Various methods propose to derive a temporally parametrized model of the displacement evolution, either assuming constant velocity between disconnected subsets (Berardino et al. (2002)) or more complex ad-hoc models (Jolivet and Simons (2018), Lopez-Quiroz et al. (2009)). A linear displacement model can simply be

$$d_k = a(t_k - t_1) + c \quad (3.8)$$

and a quadratic displacement model to take the acceleration or deceleration into account,

$$d_k = a(t_k - t_1) + b(t_k - t_1)^2 + c \quad (3.9)$$

with k index of time, a , b and c three unknown coefficients to estimate.

In case of a periodic or seasonal behavior in time, the displacement model can be

$$d_k = a(t_k - t_1) + b(t_k - t_1)^2 + c + d \cos \frac{2\pi(t_k - t_1)}{T} + f \sin \frac{2\pi(t_k - t_1)}{T} \quad (3.10)$$

with a , b , c , d , f and T six unknown coefficients to estimate.

Compared to a laplacian regularization term or a constant velocity assumption, these ad-hoc displacement models provide more physically meaningful solutions. The benefit is important especially when the number of disconnected subsets is significant.

Take the quadratic displacement model (equation 3.9) as an example for illustration, the equation system to resolve becomes

$$\begin{bmatrix} y_1 \\ \vdots \\ y_k \\ \vdots \\ d_n \\ 0 \\ \vdots \\ 0 \end{bmatrix} = \left\{ \begin{bmatrix} A_t \\ \gamma \begin{bmatrix} 0 & \dots & 0 & \dots & 0 \\ 1 & \ddots & & & \vdots \\ \vdots & \ddots & 0 & & 0 \\ \vdots & & \ddots & \ddots & \vdots \\ 1 & \dots & \dots & 1 & 0 \end{bmatrix} \begin{bmatrix} 0 & 0 & 0 \\ \vdots & \vdots & \vdots \\ 0 & 0 & 0 \end{bmatrix} \begin{bmatrix} 0 & 0 & 0 \\ -(t_2 - t_1) & -(t_2 - t_1)^2 & -1 \\ \vdots & \vdots & \vdots \\ \vdots & \vdots & \vdots \\ -(t_m - t_1) & -(t_m - t_1)^2 & -1 \end{bmatrix} \right\} \begin{bmatrix} x_1 \\ \vdots \\ x_m \\ a \\ b \\ c \end{bmatrix} \quad (3.11)$$

where γ is a scaling parameter of the additional constraint to the displacement. Its value is sufficiently small to ensure that if the inverse problem is well-posed, the additional constraint is neglected, if not, the additional constraint only sets the relative displacement between disconnected subsets. A_t corresponds to the design matrix mentioned in equation 3.6, with 0 and 1 as values.

The least-square solution to equation 3.11 provides a SR displacement time series, easy to interpret and an estimation of the unknown coefficients of the displacement model. In practice, the displacement behavior can be more complex than a linear, quadratic or periodic variation in time. An analysis of the residual of the inversion (e.g. visualization of the residual map, computation of the standard deviation, etc.) seems necessary to see the areas with displacement behaviors not taken into account by the model. When necessary, the least-square inversion can also be performed in an iterative way, with or without change to the weighting matrix.

The least-square inversion method has been applied in lots of studies (Bontemps et al. (2018), Casu et al. (2011), Hadhri et al. (2019), Jolivet and Simons (2018), Jolivet et al. (2012), Lopez-Quiroz et al. (2009)), where its efficiency has been proven. However, there are still some open questions such as how to take into account the data quality in case where data uncertainty is not available? How to deal with correlated displacement measurements? How to select the displacement measurements, in particular in terms of temporal baselines, to retrieve displacement at different scales (e.g. trend, inter-annual variation, intra-annual variation, etc.)? These open questions are discussed in the following.

Choice of weighting function

It is frequently encountered in displacement measurement that there is no displacement uncertainty associated with the displacement measurement. In case of InSAR measurements where all measurements can be considered as being of high quality, an equal weight for all measurements seems reasonable. However, in case of offset tracking measurements, sub-optimal or even erroneous estimation can be obtained, if displacement measurements of different quality are not used in an appropriate way.

In many early studies, the standard deviation of displacement values obtained in stable areas was used as a proxy of the uncertainty value associated with the displacement measurement. The rationale to do so is that the displacement value should be null in stable areas and this standard deviation measures the uncertainty related to the algorithm of the used displacement computation method. The drawback of this approach is obvious : on one hand, only one uncertainty value is available for all pixels in a displacement field, regardless of the different measurement quality over different pixels. On the other hand, the uncertainty in stable areas can be different from that in moving areas (e.g. in areas with rich textures in a pair of SAR images, offset tracking works better). In Bontemps et al. (2018), a first weighting matrix computed from the standard deviation in stable areas was used, but later replaced by a weighting matrix estimated from the residual (in the form $1/R^2$, with R denoting the residual, to assign less or even zero weight to those observations with large residual).

The deployment of the residual to determine the relative contribution of displacement measurements is useful whenever data uncertainty is not available. However, it is worth seeking for more advanced formulation than $1/R^2$ to better calibrate the residual values to weighting factors. A sophisticated way can be found in Liang et al. (2021), a recent paper dedicated for improving InSAR coherence estimation. In this paper, a down-weighting factor is computed from the residual and expressed as a bi-weight function as

$$g = \begin{cases} [1 - (\frac{u}{c})^2]^2, & |u| \leq c \\ 0, & |u| > c \end{cases} \quad (3.12)$$

with u the normalized residual expressed as

$$u = \frac{R}{s\sqrt{1-h}} \quad (3.13)$$

where h is the hat value and can be derived from the diagonal element of $A(A^T A)^{-1} A^T$ (A the design matrix in equation 3.6). s is the median absolute deviation and c is a tuning constant which is usually set as 4, 685, producing 95% efficiency at normal distribution.

In case of combination with another weighting information (e.g. quality indicator issued from the displacement estimation method or prior knowledge), the final weighting matrix can be

$$W_f = W \circ G \quad (3.14)$$

with G a diagonal matrix of the down-weighting factor obtained in equation 3.12, W a diagonal matrix of other weighting information and \circ the Hadamard entry-wise product operator. In case of iterative least-square inversions, both G and W_f can be updated iteratively.

In the Ph.D thesis of Laurane Charrier, a two-step least-square inversion strategy is adopted to estimate SR and AR (auto-regressive network, Figure 1.2 (b)) displacement time series from a large number of offset tracking measurements of Sentinel-2 image data over the Fox glacier and offset tracking measurements of Sentinel-1 image data over the Kyagar glacier. At the first step, all displacement measurements are given the same weight, with the reason that it is better to give no weight than to give erroneous weight. At the second step, the weighting matrix is computed from the residual issued from the first step according to equation 3.12. The obtained results show that this weighting strategy is efficient to remove outliers.

Choice of temporal baselines

As previously mentioned, from a time series of N images, $N(N-1)/2$ displacement measurements, including all possible temporal baselines, can be obtained. However, in practice, the quantity of displacement measurements is limited by the decorrelating characteristic of the phenomenon under observation, the availability of computing and storage facilities and the research objective. For example, for decorrelating targets such as the Alpine glaciers, long temporal baselines displacement measurements are not possible due to rapid surface changes. Therefore, small temporal baseline displacement measurements are mainly considered in the related applications (Hadhri et al. (2019), Marsy et al. (2021)). Indeed, small baseline displacement measurements are also widely computed for many other long-term correlating targets (Dalaison and Jolivet (2020)), because of the simplicity of the image network that does not require many computing and storage resources.

Actually, few studies have been carried out to investigate how to select displacement measurements with different temporal baselines in order to meet a specific need, e.g. to estimate a seasonal variation or a general trend of the displacement under consideration. Both InSAR and offset tracking measurements (from SAR, optical images and digital camera photos) provide displacement information between the two dates of image acquisitions. Therefore, in general, long temporal baseline displacement measurements bring out the averaged low frequency behavior over the period of observation, while small baseline displacement measurements highlight more the velocity and can bring out detailed high frequency displacement behavior depending on the period of observation. The smaller the temporal baseline is, the higher frequency behavior can be captured. As a result, the choice of temporal baselines strongly depends on the displacement behavior (in case we have the choice). In case of a linear displacement, a selection of temporal baselines or not can only impact the final estimation accuracy, but does not impact the retrieved displacement behavior due to the regularity of the displacement. In this case, the main concern is the measurement uncertainty that can vary depending on the temporal baselines. In case of more complex displacement behaviors, a selection of data sets with appropriate temporal baselines is

necessary to be able to get the displacement component we are interested in. For instance, to follow a moving target with a seasonal variation, small baseline displacement measurements are preferred, because long temporal baselines tend to degrade the high frequency oscillations.

The problem of the temporal baselines also concerns the output displacement time series in case that an AR (Figure 1.2 (b)) displacement time series is estimated. For example, with the acquisition cycle of Sentinel-1, 6 days, what is the appropriate temporal baseline of the AR displacement time series to generate? every 6 days or 12 days or even more? What is the impact of the input temporal baselines on the output temporal baselines, for a given displacement behavior? These problems are tackled in the Ph.D thesis of Laurane Charrier, for which two previously mentioned data sets from offset tracking of Sentinel-2 images for the Fox glacier (seasonal variation) and of Sentinel-1 images for the Kyagar glacier (abrupt acceleration and oscillations) are available. Related works performed by Laurane constitute the subject of a journal paper in preparation.

Consideration of correlated measurements

As previously shown, independence between displacement measurements is assumed in most cases for the sake of simplicity. To this effect, the uncertainty associated with the inversion result is underestimated when the independence hypothesis cannot be verified. The correlation between displacement measurements exist especially when common images are used in the displacement estimation, whereas it is extremely difficult, even impossible to quantify this correlation. Therefore, in displacement measurement, to my knowledge, no effort has been made to deal with this problem and no works can be found in the literature. On the other hand, this kind of problem also exists in the atmosphere-ocean community and more elaborated approaches have been proposed, which can be deployed for displacement measurements.

The most simple way to consider the data observation correlation is to artificially increase the data uncertainty in the data error covariance matrix, keeping the diagonal structure. This approach does not directly take the correlation into account, but tries to avoid the problem of underestimating the uncertainty associated with the inversion result. Despite the over-simplicity, a diagonal weighting matrix presents advantages in terms of computational cost. In case of a large data observation vector, algorithmic optimizations are only possible with a diagonal weighting matrix.

Another advanced alternative consists of transforming the observation vector by a regular linear transformation operator $\Gamma : y^+ = \Gamma y$ (Brankart et al. (2009), Ruggiero et al. (2016)). Each new data observation is a linear combination of all original observations. The data error covariance matrix is also transformed according to

$$\Sigma_y^{-1} = \Gamma^T \Sigma_y^{+1} \Gamma \quad (3.15)$$

It follows that any data error covariance matrix Σ_y can be simulated by a diagonal matrix Σ_y^+ in a transformed observation space. An immediate solution is to choose Σ_y^+ as the matrix of eigenvalues of Σ_y and Γ as the matrix with the corresponding normalized eigenvectors, so that $\Sigma_y = \Gamma^T \Sigma_y^+ \Gamma$, with Γ unitary and Σ_y^+ diagonal. The drawback of this solution is that it does not decrease the computational burden.

Brankart et al. (2009) and Ruggiero et al. (2016) further proposed to add the first- and second-order spatial derivatives of the data observations in the observation vector in order to deal with spatial correlation. This can be easily transferred to the temporal dimension. The addition of gradient observations to the observation vector can be equivalent to assuming a specific form of the observation error covariance matrix. In this way, the transformed observation error covariance matrix has a block diagonal form. Compared to a linear transformation, this approach is much computationally efficient. For detailed explanations, please refer to Brankart et al. (2009).

Multi-sensors displacement time series fusion

The least-square inversion approach is also able to deal with multi-sensor displacement time series fusion. Compared to the mono-sensor case, more heterogeneity is present in the data. Besides the heterogeneous data quality, the temporal baselines are not regular any more. Two more questions thus arise when we aim to estimate a homogeneous SR displacement time series. The first one is about the relative weight of displacement measurements from different sensors. Without ground truth, it is impossible to evaluate each data set in an absolute way. Moreover, it is difficult to compare displacement measurements covering different periods, with different initial spatial resolution obtained from different sensors. Even though we know that one data set is generally noisier than the other, it is not always easy to quantify the relative uncertainty. Therefore, an intuitively safe method is to give equal weight to displacement measurements of different sensors. Further refinement can be performed according the result of a first inversion. The second question is about how to deal with irregular temporal baselines. More precisely, how to decide the output temporal baselines, especially in the case of an AR displacement time series, in order to correctly retrieve the displacement behavior and to make use of as many as possible available displacement measurements. In the Ph.D thesis of Laurane, the latter problem is resolved by formulating the inverse problem in the following way,

$$Ax = By \quad (3.16)$$

Compared to the standard formulation in equation 3.6, a design matrix B is added to the data observation matrix. The main role of B is to split or combine the temporal baselines of displacement measurements in y in order to form as many as possible available measurements corresponding to the temporal baselines defined in x .

Note that the least-square inversion approach requires that the multi-sensor displacement measurements should be relatively homogeneous, that is, of the same spatial resolution, covering the same area, measuring the displacement in the same direction, etc. In case of significant heterogeneity (e.g. different areas and/or directions), it is more relevant to combine multi-sensors displacement measurements with help of a statistical or physical model. This refers to physical models inversions and data assimilation presented in Chapter 4.

3.3 Multiscale InSAR time series analysis

Hetland et al. (2012) proposed to extract spatially and temporally continuous displacement field from unwrapped interferograms stack, based on a wavelet decomposition in space and a general parametrization in time. This approach is referred to as Multiscale InSAR time series.

Parametrization of time dependent displacement For a given location s and time t , we represent the displacement (in LOS direction) as

$$d(s, t) = d_0(s) + F_d(s, t) \quad (3.17)$$

where d_0 is a location specific constant and $F_d(s, t)$ can be any time-dependent function.

For example,

$$F_d(s, t) = v(s)t \quad (3.18)$$

$$= \sum \Delta_i(s) \mathcal{H}(t - T_i) \quad (3.19)$$

$$= \sum \alpha_i^L(s) \mathcal{H}(t - T_i^L) \ln(1 + \frac{t}{\tau_i^L}) \quad (3.20)$$

$$= \sum \alpha_i^E(s) \mathcal{H}(t - T_i^E) \ln(1 - e^{\frac{-t}{\tau_i^E}}) \quad (3.21)$$

$$= \sum s_i(s) \sin(\omega_i t) + c_i(s) \cos(\omega_i t) \quad (3.22)$$

$$= \sum \kappa_i(s) B_n(t - t_i^b) + \sum \kappa_i'(s) B_n^f(t - t_i^b) + \sum \kappa_i''(s) B_{ni}(t - t_i^\#) \quad (3.23)$$

where $\mathcal{H}(t - T_i)$ is a Heaviside function centered at T_i , $B_n(t - t_i^b)$ are B-splines of order n centered on the uniformly spaced knots t_i^b , $B_n^f(t - t_i^b) = \int B_n(t' - t_i^b) dt'$ and $B_{ni}(t - t_i^\#)$ are B-splines of order n located at the non-uniformly spaced knots $t_i^\#$. The spatially dependent coefficients Δ_i , α_i^L , α_i^E , s_i , c_i , κ_i , κ_i' and κ_i'' are unknown parameters to estimate from the InSAR stack.

Equation 3.18 corresponds to linear rate displacement. Equation 3.19 describes offsets at specific times, e.g. those due to an earthquake. Equations 3.20 and 3.21 are often used to represent post-seismic displacement (sharp onsets and steady decay) (Figure 3.2). Equation 3.22 describes periodically repeating displacement (e.g. annual or seasonal variations). Equation 3.23 does not carry any assumption of the underlying component of the displacement signal and the three terms are used to describe signals that are not well described by previous components (Figure 3.2).

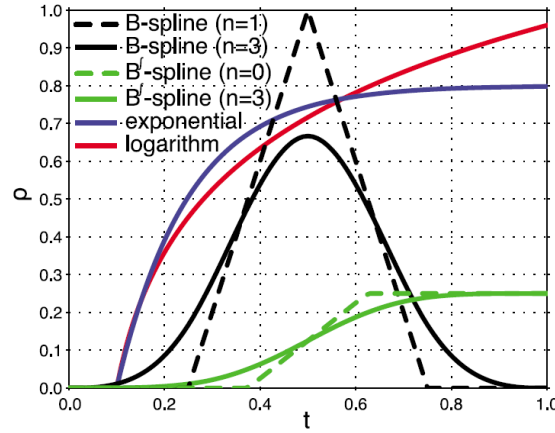


Figure 3.2 – Examples of basis functions used in the time-dependent parametrization of displacement (Hetland et al. (2012)).

Multiscale spatial decomposition The 2D spatial discrete wavelet decomposition of a given unwrapped interferogram can be represented as

$$\Delta d(s) = \sum_{a,b} r_{a,b} \varphi_{a,b}(s) \quad (3.24)$$

with $\varphi_{a,b}(s)$ 2D spatial wavelets of scale a and position b , $r_{a,b}$ are the corresponding wavelet coefficients.

Similarly, we can represent $F_d(s, t)$ as

$$F(s, t) = \sum_{a,b} \mathcal{F}_{a,b} \varphi_{a,b}(s) \quad (3.25)$$

with $\mathcal{F}_{a,b}$ the time-dependent wavelet coefficients in the parametrization of the time-dependent displacement.

Least-square inversion The temporal behavior of a given wavelet is estimated in a least-square inversion by minimising

$$\psi = \|Gm_{a,b} - y_{a,b}\|_2^2 + \lambda^2 \|Hm_{a,b}\|_2^2 \quad (3.26)$$

where $y_{a,b}$ represents the wavelet coefficients at a given scale a and location b in all interferograms, $m_{a,b}$ represents the wavelet coefficients of the parameters of the time-dependent displacement in $\mathcal{F}_{a,b}(t)$, G is the design matrix, H is a regularization matrix (e.g. to enhance a smoothness constraint or to damp the B^J -splines amplitude) and λ is the regularization penalty parameter chosen using a n -fold cross validation.

To determine $F(s, t)$, the inverse discrete wavelet transform is applied to each of the model wavelet coefficients, which results in the spatial fields of the amplitude in the time-dependent function $F(s, t)$.

The wavelet coefficients include information about the underlying spatial data covariance at any given spatial scale. The benefit of the 2D Meyer wavelet transform used in Hetland et al. (2012) lies in the fact that the covariance between wavelet coefficients in a single interferogram is neglected, we can thus determine the time-dependence of each wavelet coefficient independently. For more technical details, please refer to Hetland et al. (2012).

The interest of this method compared to the standard pixel-by-pixel least-square method is obvious : the estimation of displacement information is done in the wavelet-domain at each location and scale independently, thanks to which different displacement behaviors such as coseismic, post-seismic and seasonal loading mixed in displacement measurement time series can be separated. Moreover, this approach provides an efficient way for interpolating across regions of low interferometric coherence, giving a constrained estimation of the continuous spatio-temporal displacement field. Without experience in wavelet decomposition of displacement fields, it is difficult for me to judge the effective contribution of this method. I just wonder the efficiency of this approach in case no prior displacement information is available, because it seems that the temporal evolution of the displacement is imposed. Notice that no further development of this method can be found in the literature, but the idea of the parametric least square regression has widely been adopted later in Dalaison and Jolivet (2020), Daout et al. (2019), Maubant et al. (2020).

3.4 Spatio-temporal random effect model

Displacement measurements time series have spatial and temporal information and nearby observations in space or time generally results in higher statistical correlation. This dependence can be described through specification of a spatio-temporal covariance function or explained through a dynamical model that gives either a statistical or physical mechanism for the evolution of the present from the past. Displacement measurements fusion by means of a physical model will be discussed in Chapter 4. Here, I only focus on the statistical model, i.e. the spatio-temporal random effect model (STRE) referred to as a standard state-space model in the time series literature.

Let $s = s_1, s_2, \dots, s_n$ denote location points and $t = 1, 2, \dots, T$ denote time instant, the observations $Y(s, t)$ can be decomposed into true value $Y^r(s, t)$ and noise $\epsilon(s, t)$

$$Y(s, t) = Y^r(s, t) + \epsilon(s, t) \quad (3.27)$$

where $\epsilon(s_i, t) \sim \mathcal{N}(0, \sigma_t^2 v_i)$, $i = 1, 2, \dots, n$. v_i is the accuracy ratio of different measurements. n is the number of pixels in a displacement field. For the sake of computational efficiency, $\epsilon(s, t)$

is assumed uncorrelated spatially and temporally, which implies that correlated noise should be removed beforehand.

$Y^r(s, t)$ can be further decomposed into deterministic global spatio-temporal trends $\mu_t(s)$, local spatial variations $\nu(s, t)$ and fine-scale spatial variations $\xi(s, t)$

$$Y^r(s, t) = \mu_t(s) + \nu(s, t) + \xi(s, t) \quad (3.28)$$

The global spatio-temporal trend, $\mu_t(s)$, is correlated at large scale. It can be removed by polynomial fitting, e.g. $\mu_t(s) = X_t^T(s)\beta_t$ with $X_t^T(s) = (X_{1,t}(s), \dots, X_{p,t}(s))^T$ being the chosen trend field. Polynomial function of coordinate dimensions is a commonly used trend field. $\beta_t = (\beta_{1,t}(s), \dots, \beta_{p,t}(s))$ is the corresponding polynomial coefficients. The local spatial variations, $\nu(s, t)$, represent spatial variations locally correlated in the spatial domain and strongly temporally dependent. They can be expressed as

$$\nu(s, t) = S_t^T(s)\eta_t \quad (3.29)$$

where spatial basis $S_t(s) = (S_{1,t}(s), \dots, S_{r,t}(s))^T$ is the basis function with a fixed rank r (often low rank). Wavelet basis functions, smoothing spline basis functions and radial basis functions are often used as spatial basis (Liu et al. (2018)). In general, $S_t(s)$ is often set at different space scales and is often assumed to be consistent in time, which results in a temporal stable $\nu(s, t)$. η_t is a coefficient vector assumed to follow a vector-auto-regressive process of order one and evolves in the temporal domain according to the state transition equation

$$\eta_t = H\eta_{t-1} + \zeta_t \quad (3.30)$$

with H the state transition (or propagator) matrix and ζ_t an error term.

The fine-scale spatial variations $\xi(s, t)$ are assumed to be uncorrelated across time and space and independent of η_t , with $\xi(s_i, t) \sim \mathcal{N}(0, \sigma_{\xi,t}^2 v_{\xi,i})$. It can be modeled by the stochastic volatility model (Liu et al. (2018)) or considered as $v_{\xi,i} \equiv 1$ for simplicity.

A key feature of the STRE model is the dimension reduction that makes it possible to deal with a very large number of observations at each time instant. The use of a vector-auto-regressive model of order one (equation 3.30) allows for fast sequential processing via the Kalman Filter or the Kalman smoother.

The unknown parameters of the STRE model, including error covariance and propagator matrices that describe the spatial and temporal dependence structure in the reduced-dimensional process, can be obtained from a maximum likelihood estimator via an EM algorithm (Katzfuss and Cressie (2011)). As shown in Chapter 2, EM is particularly useful when the estimated parameters are unknown or imprecise. Once estimated, the aforementioned parameters can then be substituted into the Kalman filter or smoother equations to obtain empirical spatio-temporal predictions.

Despite the complexity of estimating a parametric model, the interest of the STRE model lies in 1) taking both the temporal and spatial dependence into account 2) providing a generic model able to characterize most encountered displacement behaviors 3) being capable of interpolating any interested spatio-temporal points, even on unmonitored areas and days.

In displacement measurement, a pioneering work exploring the STRE model (Liu et al. (2018)) was for the combination of InSAR and GNSS displacement time series in a unified framework. Satisfactory results obtained confirmed the efficiency of the STRE model.

3.5 Kalman filter based time series analysis

Dalaison and Jolivet (2020) proposed a Kalman Filter based InSAR time series analysis method, with the objective to sequentially update pre-existing displacement time series considering only

the latest data observations. Indeed, the idea comes from the data assimilation technique that will be presented in detail in Chapter 4. A parametric function of time, i.e. the linear combination of a set of user-defined functions f_n of time modulated by coefficients a_n , to describe the evolution of the interferometric phase was considered as the displacement model. The interferometric phase ϕ_i at a time t_i , relative to the phase ϕ_0 at time t_0 , thus writes

$$\phi_i = \sum_{n=1}^N a_n f_n(t_i) + \gamma_i \quad (3.31)$$

where f_n can be polynomial terms, Heaviside functions or periodic functions describing the temporal history of the interferometric phase. γ_i is the error accounting for the mismodeling of the interferometric phase at time t_i and the decorrelation noise. I think it is more appropriate to mention that γ_i is the model error accounting for the uncertainty due to mismodeling. Decorrelation noise is only related to the data observations. In Dalaison and Jolivet (2020), γ_i is assumed normally distributed with zero mean and standard deviation σ_γ . It is also assumed constant with time for the sake of simplicity, which is a strong hypothesis that does not represent the reality. What really matters is that assuming a constant model error, we cannot make full use of the data assimilation technique.

An example of the functional model (due to interseismic loading along a fault) is given as follows,

$$\phi_k = a_0 + a_1 t_k + a_2 \sin\left(t_k \frac{2\pi}{T}\right) + a_3 \cos\left(t_k \frac{2\pi}{T}\right) + a_4 S_{sse}(t_k) + a_5 H_{eq}(t_k) + \gamma_k \quad (3.32)$$

where T is a 1 year period, S_{sse} is an integrated spline function centered on Day 210 with a width of 100 to model a slow transient slip event, H_{eq} is a Heaviside function on day 500 to model an earthquake occurred on day 500 of the time series.

The unwrapped phase of the interferogram between the dates t_i and t_j is expressed as

$$\varphi_{ij} = \phi_j - \phi_i + \epsilon_{ij} \quad (3.33)$$

where ϕ_j is the unwrapped phase at time t_j relative to the phase ϕ_0 at time t_0 . ϵ is an error term potentially associated with inaccurate phase unwrapping or spatial filtering and multi-looking that break the phase consistency (Chapter 1). This error term can be related to the temporal misclosure (section 1.3.2). Its standard deviation σ_ϵ is assumed common to all interferograms for the sake of simplicity in Dalaison and Jolivet (2020).

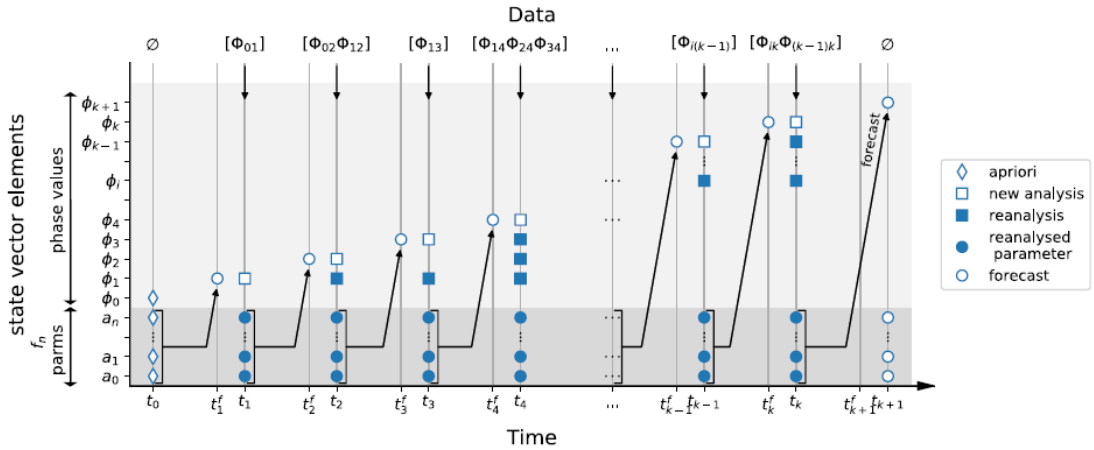


Figure 3.3 – Illustration of the state vector and data observation as a function of time (Dalaison and Jolivet (2020)).

For a given time instant t_k , the vector of parameters to estimate or re-estimate, namely state vector, is denoted $m_k = [a_0, a_1, \dots, a_L, \phi_0, \phi_1, \dots, \phi_k]$.

The value of m_k at time t_k can be obtained from its value at time t_{k-1} ,

$$m_k = A_k m_{k-1} \quad (3.34)$$

Each time a new SAR image is acquired, the interferograms connecting this last acquisition with the four previous ones are computed (i.e. small baseline interferograms). These interferograms can be related to the state vector through the observation operator H at each time instant, as

$$d_k = H_k m_k \quad (3.35)$$

The objective is to solve equations 3.31, 3.33 3.34 and 3.35 sequentially via the Kalman Filter, whenever a new acquisition is available. A SR interferogram time series is estimated as in many other multi-temporal InSAR approaches. Details of the implementation of the Kalman Filter is not presented here but in Chapter 4.

Indeed, the formulations of equations 3.34 and 3.35 are ad-hoc in order to approach the standard formulation in data assimilation. In case of earthquake and volcano displacement measurements as in Dalaison and Jolivet (2020) where advanced physical models are available, it is clearly more relevant to use a physical model and whole interferograms (i.e. spatial fields) to do data assimilation, instead of using a temporal functional model and individual points measurements.

In Bekaert et al. (2016), a similar Kalman Filter based idea was adopted, but for the estimation of geophysical parameters of a tectonic slip model. The main interest of the Kalman Filter based approach lies in the sequential integration of new acquisitions. However, appropriate formulation of the problem and adequate specification of model errors and observation errors are necessary to ensure the reliability of the final results.

3.6 Median of Multiple Common Master Series

The Median of Multiple Common Master Series (MMCMS) approach was proposed to deal with digital camera photos time series (Marsy et al. (2021)), but it can easily be extended to InSAR or offset tracking displacement time series. The principle is explained in the following.

Given a time series of N images, consider any two SR displacement time series, with r_i and r_j as reference date respectively ($i, j \in [0, N - 1]$). According to the temporal closure of the displacement, we have

$$d_{r_i r_j} = d_{r_i k} - d_{r_j k} \quad (3.36)$$

It is thus possible to estimate $d_{r_i r_j}$ with a simple mean difference between two time series

$$\tilde{d}_{r_i r_j} = \frac{1}{N} \sum_{i=0}^{N-1} d_{r_i i} - d_{r_j i} \quad (3.37)$$

Not mentioned in Marsy et al. (2021), but equation 3.36 is not respected in general cases because of uncertainty (e.g. spatial filtering or multi-looking in InSAR). Assuming a random uncertainty, N should be sufficiently large in order that $\tilde{d}_{r_i r_j}$ represents the real offset between the two time series.

Given the offset between two SR displacement time series, we can align them to a single SR displacement time series. Therefore, for each point, two versions of SR displacement time series can be obtained, one from the direct computation with respect to the reference date and the

other from the offset correction to another SR displacement time series referred to a different date (equation 3.38).

$$d_{r_i i}^{r_j} = d_{r_j i} - \tilde{d}_{r_i r_j} \quad (3.38)$$

This process is repeated for all possible reference dates (N) and one final reference date, r_{ref} , is chosen to align all the SR displacement time series using equation 3.38.

To determine the final reference date, all reference dates are tested and the one minimising the following error is chosen as the final reference date,

$$\epsilon = \frac{\sum_i \sum_j \|d_{0i}^{r_{ref}} - d_{0i}^{r_j}\|}{N^2} \quad (3.39)$$

Thus, we get N measures for each term in the SR displacement time series referred to the final reference date,

$$\begin{aligned} D_{01}^{r_{ref}} &= \{d_{01}^{r_0}, d_{01}^{r_1}, \dots, d_{01}^{r_{N-1}}\} \\ D_{02}^{r_{ref}} &= \{d_{02}^{r_0}, d_{02}^{r_1}, \dots, d_{02}^{r_{N-1}}\} \\ &\dots \\ D_{0N-1}^{r_{ref}} &= \{d_{0N-1}^{r_0}, d_{0N-1}^{r_1}, \dots, d_{0N-1}^{r_{N-1}}\} \end{aligned}$$

The median and the median absolute deviation (MAD) are computed for each term in the final SR displacement time series. Further processing consists of thresholding on the median and MAD values to remove outliers. The procedure can be performed iteratively with outliers removed at each iteration in order to refine the final SR displacement time series estimation.

For large and very large temporal baselines, the displacement cannot be computed directly because of significant surface change. Marsy et al. (2021) proposed to construct the SR displacement time series in an incremental way by applying the MMCMS approach to subsets time series. The offset between subsets time series is estimated and a connection between subsets time series is performed to obtain the complete time series. This implementation allows for gradual integration of new arriving images and displacement measurements.

Marsy et al. (2021) compared the MMCMS approach with the standard least-square inversion approach and in situ GPS measurements in the displacement measurement of the Argenti re glacier. They concluded that the MMCMS approach slightly outperforms the least-square inversion in their application. However, notice that, the computational load of the MMCMS approach is more significant than that of the least-square inversion.

3.7 Machine learning based approaches

One of the most important recent advances in displacement time series analysis consists of using machine learning methods. Different from the previously presented multi-temporal approaches whose purpose is to reduce the dimension of displacement data sets and to estimate consistent and easily understandable displacement information, actual machine learning methods aim to automatically detect displacement signals of interest in large displacement measurement data sets without any estimation, in other words, to separate displacement signals from other perturbations (e.g. atmospheric signals).

The first works deploying neural networks based methods have been performed with seismic data (Magrini et al. (2020), Mosser et al. (2018), Titos et al. (2019)) and further development continues. For instance, Titos et al. (2019) used recurrent neural networks (RNN), long short term

memory (LSTM) and gated recurrent unit (GRU) to detect and classify continuous sequences of volcanic-seismic events. Regarding the exploitation of SAR displacement time series, pioneering works to automatically detect displacement signals have mainly been proposed by the UK COMET group with applications to volcanic deformation. Two categories of works can be outlined, one with traditional machine learning techniques such as PCA, ICA and Nonnegative Matrix Factorization (NMF) (Ebmeier (2016), Gaddes et al. (2018, 2019), Maubant et al. (2020)); the other with convolutional neural networks (CNN) techniques (Anantrasirichai et al. (2018, 2019a,b)).

3.7.1 Traditional ML approaches

PCA, ICA and NMF have been deployed to separate the displacement signal from other components in SR and AR time series of interferograms (Ebmeier (2016), Gaddes et al. (2018), Maubant et al. (2020)). The displacement signal separation problem is formulated as a blind source separation (BSS) problem, and the observed mixed signals are assumed to be generated using the following mixing model :

$$X = AS \quad (3.40)$$

where X contains the mixtures as row vectors, S contains the unknown sources as row vectors and A is the unknown mixing matrix that combines varying amounts of the sources to create each mixture. The rows of A are coefficients that describe the relative contribution of each source to a particular mixed signal.

The sources S can be recovered if we could calculate the unmixing matrix W ,

$$S = WX \quad (3.41)$$

with

$$A = W^{-1} \quad (3.42)$$

The preceding description of linear mixing can also be expressed in terms of Euclidean geometry (Figure 3.4). The goal of the BSS is to find the basis vectors required to recover each source from the mixture. PCA, ICA and NMF have been investigated to implement BSS. A summary is given in the following.

PCA finds a unique solution to the decomposition of a mixed signal by maximizing signal variance, with the assumption that sources are uncorrelated. The PCs are routinely found by calculating the eigenvectors and eigenvalues of the mean-centered data covariance matrix. The change of basis can be achieved as follows,

$$S_r = E^T X \quad (3.43)$$

where S_r is the reconstructions of the sources, E is a matrix of eigenvectors.

This is closely related to the work of (Prébet et al. (2019)) in which PCA is used to retrieve coherent displacement signal from AR displacement time series (section 2.3). According to Prébet et al. (2019), the separation of displacement signal from spatially correlated atmosphere-like noise by PCA is not always efficient.

ICA is a classical method for BSS. It aims to describe random variables as a linear combination of statistically independent components. This is achieved by the decomposition of a mixed signal using the assumption that each constituent component has a non-Gaussian probability distribution. ICA retrieves sources by maximizing statistical independence. Each independent component is estimated by choosing unmixing vectors that maximize the non-Gaussianity of its product with the data, assessed by using a property such as kurtosis or negentropy. Many specialized ICA tools can be found in the literature. The FastICA algorithm (research.ics.aalto.fi/ica/software.shtml) constitutes one of the most used tools (Ebmeier (2016), Gaddes et al. (2018), Maubant et al. (2020)).

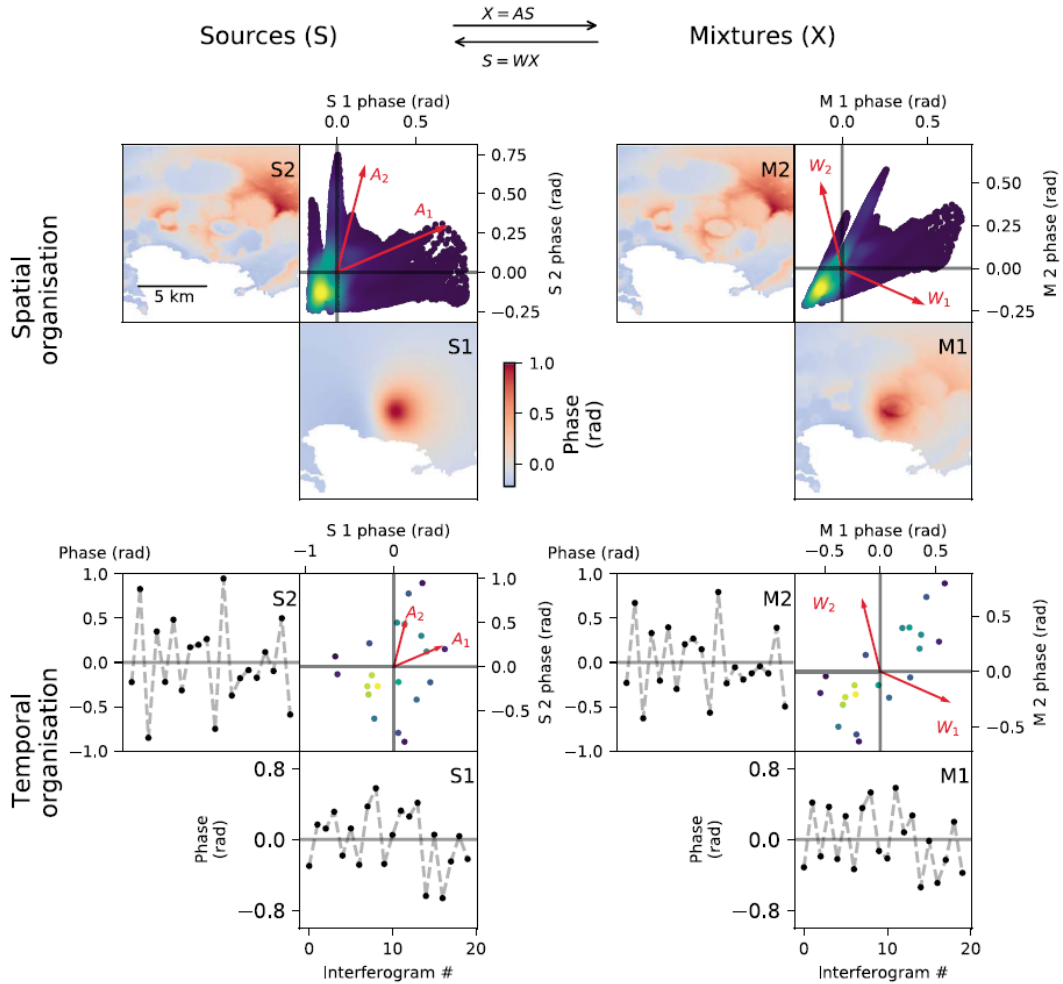


Figure 3.4 – Linear mixing for spatial and temporal data. Spatial organization : a deformation signal (S1) is mixed with a topographically correlated signal (S2) through reprojecting the data in the directions A_1 and A_2 , to produce two mixtures, M1 and M2. The sources can be recovered from the mixtures by reprojecting the data in the directions W_1 and W_2 . In this case, the mixture space has as many dimensions as the number of interferograms and as many points in the space as the number of pixels in the interferograms. Temporal organization : the displacement evolution on one pixel over 20 epochs (S1) is mixed with the evolution of a topographically correlated atmospheric signal on the same pixel (S2) in a similar manner to the spatial case to produce two mixtures, M1 and M2. In this case, the mixture space has as many dimensions as the number of pixels the interferograms have and as many points in this space as the number of interferograms. Progression from blue to yellow is used to indicate areas of high point density in the scatter plots (Gaddes et al. (2018)).

NMF factorizes a non-negative data matrix of mixture, X , into two non-negative matrices, A and S . It cannot be used on data that contains negative values. In Gaddes et al. (2018), it is only applied to a SR displacement time series in order to keep positive displacement values.

Gaddes et al. (2018) concluded that ICA is the best suited for most applications with InSAR data. Cohen-Waeber et al. (2018) used ICA to identify precipitation-modulated landslide spatio-temporal patterns from a SR InSAR time series. Gaddes et al. (2019) further used ICA to identify deformation that departs from the background rate/pattern and may not be clear in single interferograms.

ICA has the advantage over the PCA to decompose the signal in a set of statistically independent components, which are more likely to represent independent sources. However, the ideal number of ICs and their order of importance are not defined. Selecting too few ICs may mix different sources together and selecting too many will split the sources of interest over many components with large errors. In Maubant et al. (2020), PCA and GPS data have been proposed to aid the determination of the appropriate number of ICs. Note further that ICA is successful when constituent sources are very non Gaussian. Gaussian sources will not be extracted as ICs and the presence of correlations between constituent sources results in signals related to different sources being captured in the same ICs.

3.7.2 Neural networks approaches

Anantrasirichai et al. (2018) proposed, for the first time, to use CNNs to detect large and rapid volcanic deformation signals in wrapped interferograms. The main idea is to distinguish fringe patterns related to displacement from atmospheric artifacts, the latter can also generate concentric fringes around volcanoes, particularly those with steep topography. The proposed CNN framework, including training and prediction processes, is illustrated in Figure 3.5. This study showcased the ability of CNNs to detect rapid displacement that generate multiple fringes in wrapped interferograms, but could not reliably distinguish between displacement signals and atmospheric artefacts in case of small displacement. Anantrasirichai et al. (2019a,b) further improved the previously developed approach to be able to detect slow, sustained deformation (i.e. lower rate and smaller spatial scale) in urban environments, by rewrapping the displacement map to increase the number of fringes.

These proof-of-concept studies demonstrate the ability of neural networks based approaches in automatically analyzing large displacement measurement data sets. For example, in Anantrasirichai et al. (2018), the global data set used in the study consists of 30,249 Sentinel-1 interferograms covering 900 volcanoes in 2016–2017. The proof-of-concept algorithm reduces the number of interferograms that require manual inspection from more than 30,000 to 104, which makes it possible to timely deliver the results to the appropriate authorities. However, it is also worth mentioning that the supervised learning of DNN models generally relies on the availability of large annotated data collections that cannot always be available. To provide ground-truth information for training and verification of supervised classification systems, it is necessary to manually identify a selection of interferograms where several fringes can be attributed to volcanic deformation. Identifying a sufficient number of positive images in this vast data set is challenging. Anantrasirichai et al. (2018) used an older ENVISAT archive to initialize their classification model for the sake of convenience. On the other hand, even with the efficient automatic detection of displacement signals in large InSAR data sets, expert analysis is still required to distinguish deformation from some types of atmospheric artifacts and to interpret the deformation patterns in terms of source processes. Actually, the development of neural networks based approaches in InSAR community is still at a very early stage. A lot of efforts are still necessary before they can be considered as completely operational approaches.

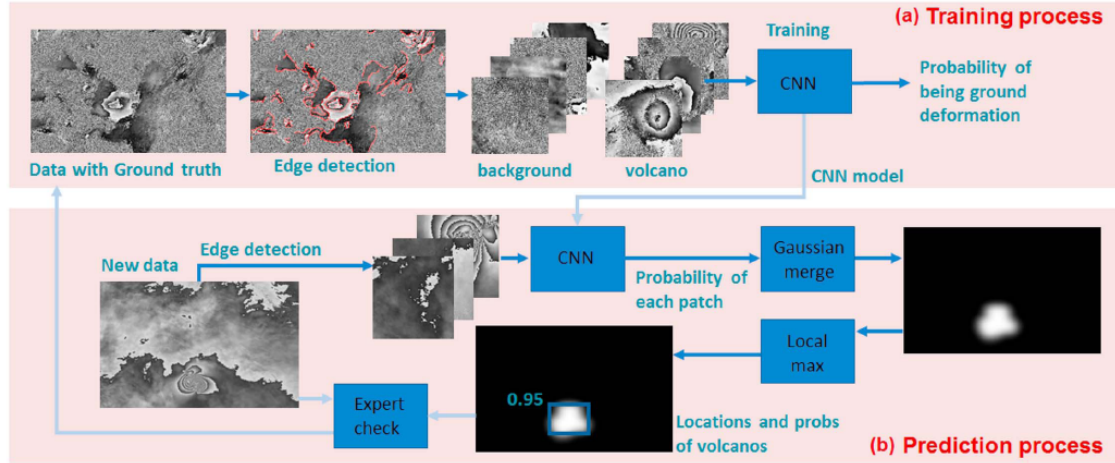


Figure 3.5 – Diagram of the CNN framework for volcano signal detection. The training process starts with data with ground truth (labeled as 1 or positive, where deformation is present; and 0 or negative in other areas). Then, edge detection is applied so that only the areas with large phase changes are considered. These areas are subsequently divided into two classes of patches and fed to the CNN for training. For the prediction process, the new interferogram is divided into overlapping patches, and the patches with strong edges are tested with the trained CNN model, giving the probability P of being ground deformation. The probabilities of all patches are merged with Gaussian weights. The highest probability P_{max} and its location are provided for the development of an alert system. Finally, the expert checks the result, and the positives are employed to retrain the CNN for better performance (Anantrasirichai et al. (2018)).

3.8 Conclusions & Perspectives

A non-exhaustive list of approaches for displacement time series analysis is presented in this chapter. Each approach has its own advantages and shortcomings. In particular, each approach can respond to a specific need (e.g. reduce the dimension of the data set, separate the displacement signal from other perturbations. etc.). It is impossible to conclude on the relative performance of all the aforementioned approaches. Indeed, there has not been benchmark studies that aim to compare all the state-of-the-art displacement time series analysis approaches. In certain ways, this kind of benchmark studies do not really make sense in my opinion. We can choose the appropriate approach(es) depending on the data sets to deal with (i.e. dimension, uncertainty, completeness, consistency, etc.), the scientific objective to reach and the available resources.

Personally, I consider the standard pixel-by-pixel least-square inversion as a first choice, because of its ease of implementation and almost universal applicability. More importantly, in most cases, it can give satisfactory results, sufficiently accurate for further interpretation. According to the results obtained in the Ph.D thesis of Laurane Charrier, this approach is not only efficient for linear displacement behavior, but also for other complex displacement behaviors such as seasonal oscillations and mixed exponential trend and seasonal oscillations (provided that the choice of temporal baselines is appropriate). Moreover, despite a pixel-by-pixel strategy, no spatial discontinuities have been observed in the final retrieved displacement fields time series. For its efficiency in terms of both computational time and result quality, it constitutes an important step of the SBAS approach and the offset tracking operational processing adopted in the online service of ground deformation monitoring (GDM) developed by ForM@Ter in France (<https://www.poletterresolide.fr/projets/en-cours/gdm-epos/>). The multi-scale InSAR time series analysis approach is also based on a least-square inversion, but displacement values are replaced by the wavelet coefficients of spatial displacement fields as input in order to take the spatial correlation into account. This approach is especially helpful when the displacement measured is composed of mixed behaviors such as coseismic, post-seismic and other transient deformations and when we want to separately quantify these behaviors. The STRE model provides unified modeling of dis-

placement fields time series, with realistic assumptions of error statistics. However, the estimation of the model parameters involves sophisticated statistical methods. Its usefulness is particularly highlighted while dealing with heterogeneous displacement measurement time series, e.g. obtained from different sensors and when the physical model is not available. A statistical spatio-temporal displacement model thus allows for efficient integration of different displacement measurements and is able to produce regular and homogeneous displacement products, even for unobserved areas and dates. The MMCMS approach was initially developed for digital camera photo time series. One important difference between digital camera photo time series and InSAR/offset tracking displacement time series lies on the temporal miscore error. It appears that the temporal miscore error of digital camera photo time series is inherently small (according to communications with colleagues who work on digital camera photos). Therefore, the efficiency of this approach for InSAR/offset tracking displacement time series still needs to be proven. ICA based approaches are useful for separating displacement signals from other sources of perturbations (e.g. atmospheric perturbations). These approaches are rather applied to SR or AR displacement time series. I cannot see the point of applying these approaches to a large data set including interferograms or offsets of all temporal baselines. Neural networks based methods outperform the others in case of very large data set automatically produced (in a blind way) such as that used in Anantrasirichai et al. (2018). Even though lots of time consuming preparation works are necessary for neural networks to work properly, as soon as the training procedure is finished, results can be delivered timely.

To meet the need for operational processing, besides the ability to provide reliable results, the appropriate approaches should be fast and preferably be able to handle new displacement measurements in a gradual way. From this point of view, on one hand, the standard least-square inversion can always be considered as a candidate approach, because it can be applied to any subset of a displacement time series. Of course, elaborated adaptations will be necessary to merge the results obtained from isolated or connected subsets. On the other hand, approaches allowing gradual integration of displacement measurements such as the STRE model and the kalman filter based approach and approaches allowing working on subsets such as the MMCMS approach (if its efficiency can be proven) seem promising. Finally, with further development of neural networks based approaches, we can also rely on future neural networks based approaches.

4

Estimate and predict geophysical parameters by inversion and data assimilation

4.1 Introduction

Besides direct Earth deformation monitoring, the main objective of displacement estimation is to infer the subsurface geological structure and to predict natural hazards. Subsurface modelling studies often rely on inversion methodologies to derive subsurface properties that are consistent with both available prior information and displacement observed at the Earth's surface. However, predictions based on physical models alone are often far from reliable so that they cannot be considered as operational tools. SAR derived displacement time series have been proven effective and have always provided meaningful insights into what is going on beneath the Earth's surface through physical model based inversion. They begin to be used as major sources for subsurface deformation sources characterization, thanks to the regular and free Sentinel-1 A/B acquisitions. Despite being very successful, such model-driven approaches require sufficiently accurate modelling of the phenomenon under observation and cannot be deployed as a universal approach.

Hazard prediction is one of the most challenging tasks in geophysics, because of the complex nonlinear behaviors, intrinsic unpredictability of natural phenomena and lack of direct observations on what is exactly happening underground. Current practices that lead to successful prediction are mostly based on empirical pattern recognition that relies on present observations, geological and historical information from global monitoring databases and scientific insights of experts (Bato (2018)). For an operational prediction purpose, data assimilation, combining a dynamical model and data observations in the past and at present based on error statistics, has been proposed recently to predict the pressurization and rupture of magmatic reservoirs (Bato et al. (2017, 2018)). Promising results obtained confirmed the predictive capability of the proposed data assimilation method. However, the success of data assimilation depends strongly on the knowledge about the physical model error and data observation error statistics that are often poorly known. Moreover, non-Gaussian properties of errors, highly nonlinear models and implicit relationships between physical model parameters and data observations can significantly degrade the predictive ability of most operational data assimilation methods

The recent advent of neural networks based machine learning paradigms enables the development of new solutions to tackle the previous shortcomings of model-driven inversions and predictions. Generative deep neural network (DNN) models such as Generative Adversarial Networks (GAN), being able to generate very realistic stochastic representations, have been deployed

with success in seismic and hydrological inversions (Laloy et al. (2018, 2019), Mosser et al. (2018), Zhang and Lin (2020)). Also, DNNs capable of integrating temporal information such as Recurrent Neural Networks (RNN), have been deployed to predict earthquake trend and structural seismic response from historical data (Vardaan et al. (2019), Zhang et al. (2019)). Other attempts make use of Convolutional Neural Networks (CNN) and RNN to investigate glacier evolution modelling (Bolibar et al. (2020)). These proof-of-concept studies highlight the interest of neural networks based methods compared to the traditional physics based methods : free of statistical hypotheses made on model parameters, capable of dealing with data/model complexity (e.g. high dimensional nonlinear model, implicit relationship between data and model parameters, partial knowledge on the physical model, etc.) and data adaptive. Therefore, neural networks based methods are worth investigating in Earth deformation inversion and prediction with SAR displacement time series, complementary to physics/statistics based methods.

In the following, I first present the conventional model driven inversion methodologies to estimate geophysical parameters from SAR, optical and GNSS displacement measurements. Results obtained in the cases of the 2005 Kashmir earthquake and the 2011 post-eruptive event of the Grímsvotn volcano are used for illustration. Second, I introduce in detail the methodology of data assimilation, in particular, the Ensemble Kalman Filter to predict the temporal evolution of key geophysical parameters by sequentially assimilating data observations. Works carried out in the Ph.D thesis of Mary Grace Bato, a pioneering investigation of data assimilation in volcanology, will be showcased. Finally, I will talk about data driven inversion and prediction methodologies, i.e. neural networks based inversion and predictions to estimate and to predict geophysical parameters by means of SAR displacement time series. The latter constitutes the future work that I want to develop in the coming years.

4.2 Model driven approaches

4.2.1 Inversion

SAR derived displacement fields constitute one of the major sources to explore the subsurface feature of the Earth by means of inversion. The latter involves modeling the deformation source and physical mechanism at depth that explain the displacement fields observed at the Earth's surface. Solving such an inverse problem means finding a set of model parameters that best fit the observations.

The classical inverse problem is of the following form ¹

$$y = G(m) + \epsilon \quad (4.1)$$

y represents data observations, m is a vector of model parameters we aim to estimate, both y and m are elements in appropriate function spaces, G represents the forward model operator that describes how the model parameters give rise to data observations in the absence of noise and measurement errors, ϵ is an error term including the observational error and the modelling error, often assumed random.

Indeed, most inversions in geophysical applications are ill-posed, that is, small errors in data may lead to large errors in the model parameters or several sets of model parameters may match the same data observations. This is mainly due to noise and incompleteness presented in data observations and uncertainties associated with modeling. Addressing ill-posedness is critical in

1. There is no formal mathematical definition of an inverse problem, but from an application point of view, it is common to formalize it as solving an operator equation - determine causes from observed effects.

all research and applications where decision making is based on the recovered model parameters (e.g. risk assessment, operational monitoring, etc.). For this, on one hand, we formulate the knowledge about possible or impossible model parameters (based on natural experience and/or previous studies) as a prior probability density function (pdf) of model parameters. The choice of an appropriate prior pdf of model parameters is essential but challenging to ensure posterior consistency and global convergence. On the other hand, ill-posedness has also been counteracted by means of regularization, a scheme providing a well defined parameterized mapping between model parameters and data observations to guarantee properties such as existence, stability and convergence.

Two main state-of-the-art approaches are functional analytic inversion and Bayesian inversion, both derived from the knowledge we have about the data, the model parameters and their relationship (Arridge et al. (2019)).

Functional analytic inversion

Functional analytic inversion makes no statistical assumptions on the model parameters and only single model parameters values, i.e. approximations of the true values, are estimated.

The first solution consists of approximating analytic inversions based on stabilizing a closed-form expression of G^{-1} . These approaches are, however, highly problem-specific. A large body of literature addressing iterative methods based on gradient descent for the data misfit $\|G(m) - y\|^2$ can also be found. A well known example is the maximum likelihood expectation - maximization (EM) algorithm (Dempster et al. (1977)). Besides iterative methods, another common framework corresponds to variational methods, whose idea is to minimize a measure of data misfit penalized using a regularizer (equation 4.2). A well known example is the classical Tikhonov regularization.

$$m = \arg \max_{m \in X} \{\mathcal{L}(G(m), y) + \lambda \Gamma(m)\} \quad (4.2)$$

where \mathcal{L} is the data discrepancy measure (i.e. misfit function), Γ is a regularization functional. λ is a weighting factor.

A statistical model for data description is mostly used to justify the choice of data discrepancy in a variational method and for selecting an appropriate regularization parameter.

Indeed, the deployment of the functional analytical inversion requires a precise description of the forward model operator, G . However, analytic expressions do not always exist to describe the often complex but partially observed physical process with reasonable accuracy. Therefore, functional analytical inversion cannot see a widespread application in geophysical inversions.

Bayesian inversion

Bayesian inversion considers both data observations and model parameters as realisations of random variables and phrases the inverse problem as a statistical inference question, that is, from a prior pdf of model parameters, $P(m)$, approximating a posterior pdf of model parameters conditioned on data observations, $P(m|y)$ (Tarantola (2005)).

$$P(m|y) = \frac{P(y|m)P(m)}{P(y)} \quad (4.3)$$

with $P(y)$ corresponds to the data likelihood, which can be considered as a constant, since it does not depend on the model parameters.

In this way, the posterior pdf of model parameters writes as

$$P(m|y) \propto P(y|m)P(m) \quad (4.4)$$

where $P(y|m)$ is the likelihood, which represents the probability to obtain the data observations y , given the model parameters m .

Equation 4.4 demonstrates how the data observation is involved in the retrieval of the posterior pdf of model parameters from their prior pdf. The likelihood, $P(y|m)$, follows the direct problem and relates the model parameters and the data observations. It is a measure of the degree of fit between the observed data and the model predicted "data". Typically, this is done through the introduction of a misfit function $\mathcal{L}(y|m)$, connected to $P(y|m)$ through an expression like $P(y|m) = k \exp(-\mathcal{L}(y|m))$ with k an appropriate normalization constant. The common form of the likelihood is the Gaussian likelihood (equation 4.5) when the error term, ϵ in Equation 4.1 follows a Gaussian distribution.

$$P(y|m) = \frac{1}{\sqrt{(2\pi)^{N_y} |\Sigma_y|}} \exp\left[-\frac{1}{2}(y - G(m))^T \Sigma_y^{-1} (y - G(m))\right] \quad (4.5)$$

where Σ_y denotes the error covariance of data observations and $|\Sigma_y|$ its determinant.

The Gaussian likelihood (coupled with a L2 norm of the misfit function) is widely used, but it is not robust against outliers included in the data (Gesrt (2021)). In this case, other likelihood models such as the Laplace distribution (equation 4.6) should be considered.

$$P(y|m) = k \exp\left(-\sum_i \frac{|G_i(m) - y_i|}{\sigma_i}\right) \quad (4.6)$$

where σ is the estimated data uncertainty.

In general, the choice of the likelihood depends on the quality of the data observations (i.e. statistical properties of data uncertainty). For example, if the data observations are contaminated by statistically independent random errors given by a double Gaussian probability density function like

$$f(\epsilon) = k \left[a \exp\left(-\frac{\epsilon^2}{2\sigma_1^2}\right) + b \exp\left(-\frac{\epsilon^2}{2\sigma_2^2}\right) \right] \quad (4.7)$$

then

$$P(y|m) = k \Pi_i \left[a \exp\left(-\frac{(G_i(m) - y_i)^2}{2\sigma_1^2}\right) + b \exp\left(-\frac{(G_i(m) - y_i)^2}{2\sigma_2^2}\right) \right] \quad (4.8)$$

with a, b two constants.

However, in practice, realistically describing data uncertainty constitutes a difficult topic.

The prior pdf of model parameters, $P(m)$, is also usually considered following a Gaussian distribution. In case without clear prior information on the model parameters, it is appropriate to use a uniform distribution.

With the prior pdf and the likelihood defined, we can obtain either the most likely model parameters by maximising the posterior pdf (to solve an optimization problem) or a complete solution including all possible model parameters given the data observations (to solve a sampling problem). In the former case, when we estimate the uncertainty associated with the most likely model parameters, we make Gaussian hypothesis on the posterior pdf, whereas it is often more complex than a Gaussian distribution. On the other hand, the sampling of the complete distribution in the latter case allows an unbiased estimate of the uncertainties of the model parameters. Therefore, the latter solution seems more relevant and gains in popularity in most recent geophysical inversions. A well known example is the Markov Chain Monte Carlo (MCMC), whose main idea consists in generating models sampled with a frequency distribution equal to the prior probability distribution in the model space by means of a random walk and comparing model based predictions to the data observations, with models accepted or rejected depending on the models ability to reproduce observations and according to the Metropolis-Hastings rule (Mosegaard and Tarantola (1995), Sambridge and Mosegaard (2002), Segall (2013)). This kind of methods often requires high computational load, in particular, long computational time. Designing an appropriate prior and to have a computational feasibility for exploring the posterior is essential for implementing Bayesian inversion.

Case studies

My early experience in physical model inversion was to estimate the geometrical parameters and the slip (i.e. displacement) distribution of the fault rupture model (i.e. Okada model, a homogeneous linear elastic halfspace model assuming that the fault dislocation is a rectangular plane reaching the surface) in the case of the 2005 Kashmir earthquake in my Ph.D thesis, using displacement fields obtained from InSAR and offset tracking of ENVISAT images. Due to the complexity of the inverse problem (i.e. number of model parameters to estimate and the non-linearity of the forward model operator), the problem was solved at two steps. At the first step, a nonlinear inversion was performed to estimate the geometrical parameters of the fault rupture, assuming fixed slip on the fault plan. Monte Carlo type inversion (with 100 realizations) was performed, starting from a Gaussian prior pdf of model parameters obtained from a previous study. The posterior distribution of the estimated geometrical parameters is shown in Figure 4.1. At the second step, the slip distribution was estimated with the geometrical parameters obtained previously. A linear functional analytical inversion was performed, the solution was given by a variational method with a Laplacian regularizer (equation 4.2) to avoid non physical solutions. The result obtained is shown in Figure 4.2.

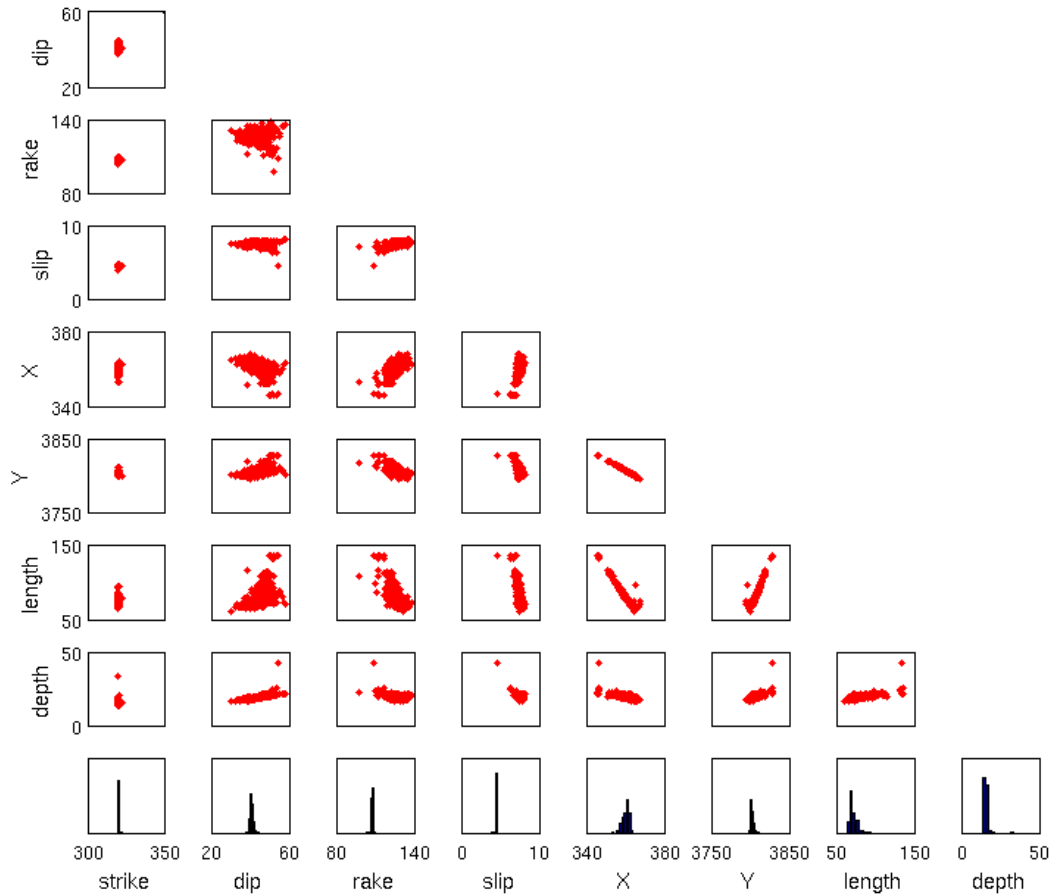


Figure 4.1 – Posterior pdf of geometrical parameters of the fault rupture model of the 2005 Kashmir earthquake obtained from InSAR and offset tracking measurements. The marginal pdf for each parameter is shown in the blue histogram plots on the bottom. The red scatter plots indicate the correlation between parameters. depth and length correspond to the depth and the length of the fault plane. (X, Y) is the coordinate of the center of the fault trace at the surface. strike is the angle between the North and the line representing the intersection of the fault plane with a horizontal plane. dip is the angle between the fault plane and a horizontal plane. rake is the slip direction in the fault plane. (Yan et al. (2013)).

In the Ph.D thesis of Mary Grace Bato, she deployed MCMC (in the PyMC2 python mo-

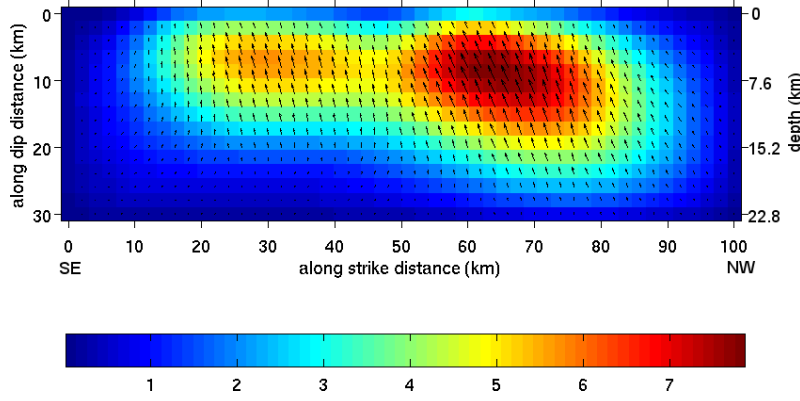


Figure 4.2 – Slip distribution of the fault rupture model of the 2005 Kashmir earthquake obtained from InSAR and offset tracking measurements. Arrows indicate the slip directions on the fault plane. (Yan et al. (2013)).

dule) to estimate some unknown parameters of a two chamber magma model (Figure 4.5), $m = [a_d, H_d, C, \Delta\rho, \Delta P_{d_{t0}}, Q_{in}]$, using GNSS displacement measurements in the case of the 2011 post-eruptive event of the Grímsvotn volcano. Details of the two-chamber magma model are given in section 4.2.2 where the model is fully exploited in data assimilation. The prior distributions are obtained from previous studies and expert’s knowledge. The posterior pdf of the estimated parameters is shown in Figure 4.3.

From Figures 4.1 and 4.3, we can see that geophysical parameters to estimate can be more or less correlated. Trade-off occurs between correlated parameters in the inversion. In order to avoid this, Bato (2018), Bato et al. (2018) adopted the adaptive metropolis (AM) step method that fits the parameters by block updating them using multivariate jump distribution.

4.2.2 Data assimilation

Data assimilation refers to a set of statistical methods (e.g. Ensemble Kalman Filter, Particle filter, 4D-VAR, etc.) that use all the available information including data observations in the past and at present and a priori information in order to improve the knowledge about the future state of a dynamical system. It takes advantage of the complementary information provided by the physical model and the data observations, with the objective to provide an estimate with improved accuracy. It is widely used as operational tools in climate-weather forecasting and has gained a lot of development in the atmosphere-ocean science community. It has recently been introduced to solid Earth geophysics such as geomagnetism (Fournier et al. (2007a,b)) and volcanology (Bato et al. (2017, 2018), Gregg and Pettijohn (2016), Zhan and Gregg (2017), Zhan et al. (2017)).

Basic concept

The principle of data assimilation consists of an appropriate combination of the model prediction and data observations, based on their error statistics, in order to predict the future state of the dynamical model. The latter is represented by the model state vector which is composed of a set of model state variables (i.e. prognostic variables that reveal the state governed by the physical process) and sometimes a set of model parameter variables (i.e. variables that govern the physical process). The main idea of data assimilation is thus to update the model state vector over time, in other words, to gradually correct the trajectory of the model state by data observations in order that the model would provide reliable short-term and/or long-term predictions of the model state variables.

Consider a model state vector \mathbf{x} , the dynamical model can predict the value of \mathbf{x} at instant n

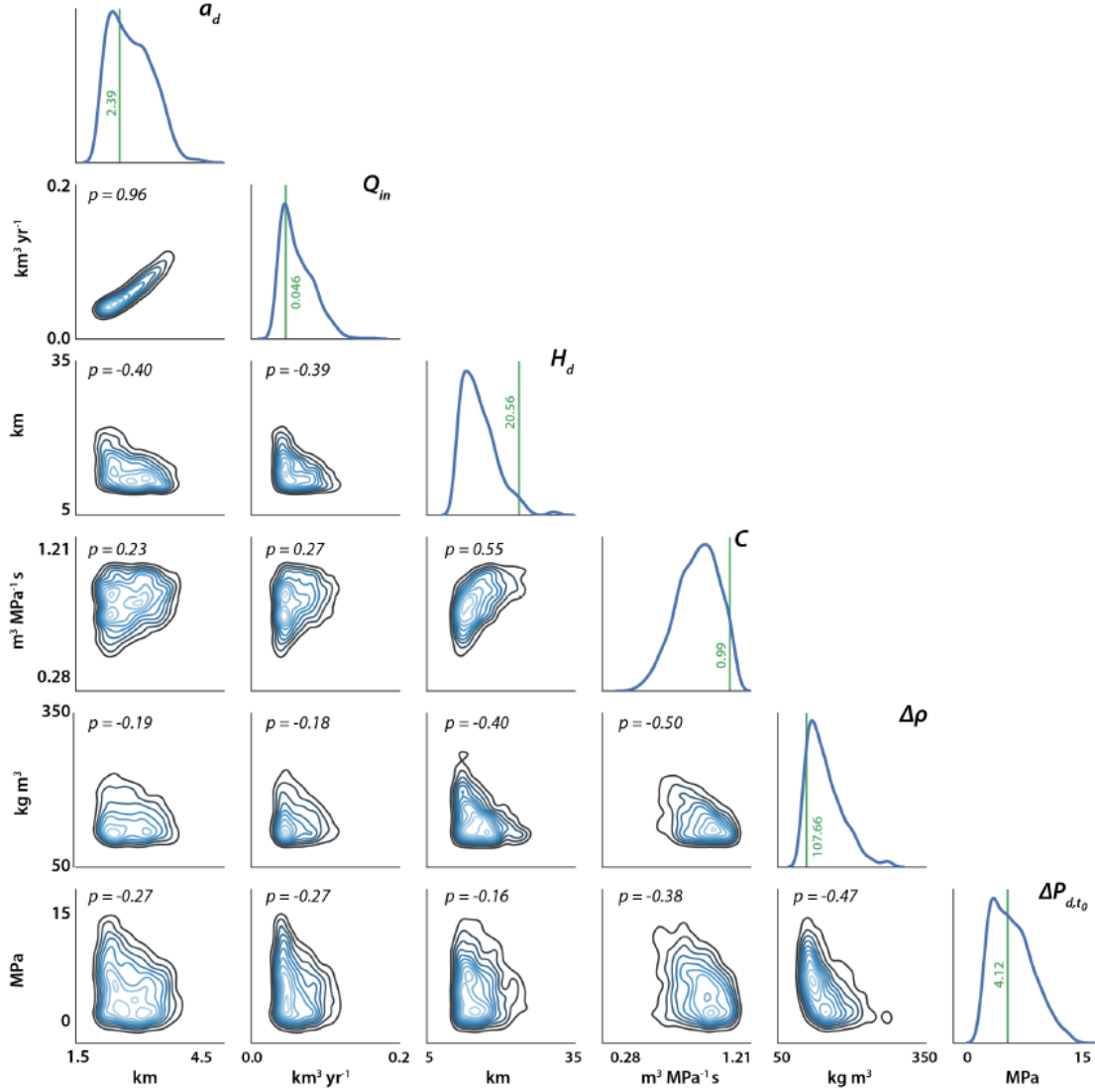


Figure 4.3 – Posterior pdf of some unknown parameters of a two-chamber magma model of the 2011 post-eruptive event of the Grímsvötn volcano obtained from GNSS displacement measurements. a_d is the radius of the deep reservoir, Q_{in} is the magma inflow rate at the bottom, H_d is the depth of the deep reservoir, C is the characteristic of the hydraulic connection with $C = \frac{a_c^4}{\mu H_c}$ where a_c is the radius of the conduit, μ is the viscosity and H_c is the height of the hydraulic connection, $\Delta\rho$ is the density contrast between the rock and the magma, $\Delta P_{d,t_0}$ is the initial over-pressure of the deep reservoir at time t_0 . The marginal pdf for each uncertain parameter is shown in the diagonal histogram plots. The green vertical lines with numbers indicate the best-fit values of the parameters. The off-diagonal contour plots are the joint kernel-density estimate between pairs of parameters with their corresponding Pearson correlation coefficients. A p-value close to ± 1 implies strong correlation between the parameters (Bato et al. (2018)).

from the value at the previous instant as expressed in the following model integration equation,

$$\mathbf{x}_n = \mathcal{M}(\mathbf{x}_{n-1}) + q_n \quad (4.9)$$

where \mathcal{M} is the forward model operator which represents the physical process of the phenomenon, it can be linear or nonlinear. q is the model error which can be due to the choices or limitations related to the model physics and parameters, including errors associated with assumptions, theory and conceptualisations within the underlying equations, errors due to the computational grid and its discretisation, numerical errors related to the time step or numerical methods used to solve the mathematical equations and errors associated with the model parameters.

To start the model, an initial condition of \mathbf{x} , denoted \mathbf{x}_0 , is necessary. In most cases, the initial condition is obtained from assumptions, measurements or previous studies, thus subject to uncertainty.

$$\mathbf{x}_0 = \mathbf{x}_0^t + \eta \quad (4.10)$$

where \mathbf{x}_0^t is the true initial condition and η is the error of the initial condition.

The data observations, \mathbf{y} , are related to the model state vector through the observation operator,

$$\mathbf{y}_n = \mathcal{H}(\mathbf{x}_n) + \epsilon_n \quad (4.11)$$

where \mathcal{H} is the observation operator, often supposed to be linear. ϵ is the observation error due to either the instrument itself or different perturbations during the data acquisition and noise generated during the data processing.

In general, the model error, the initial condition error and the observation error are uncorrelated with each other, thus $E[q\eta^{iT}] = E[q\epsilon^T] = E[\eta^i\epsilon^T] = 0$. These errors are also assumed following a normal distribution in lots of cases for the sake of simplicity.

At each instant, the model error covariance, P , and the observation error covariance, R , are computed as follows :

$$P = E[q_k q_m^T] \quad (4.12)$$

$$R = E[\epsilon_k \epsilon_m^T] \quad (4.13)$$

with k, m denoting index of model state vector elements or observation vector elements and T denoting the transpose operator.

Accurate knowledge of the model error covariance and the observation error covariance is crucial to guarantee the relevance of the assimilation results. However, their quantification is not always simple in the practice, especially the quantification of the model error because of insufficient knowledge about the phenomenon under observation.

Ensemble Kalman Filter

Ensemble Kalman Filter (EnKF) constitutes one of the most widely used data assimilation approach in operational forecasting, thanks to its high performance in dealing with nonlinear model, high dimensional state vector, etc. (Yan et al. (2014, 2015)). One important feature of EnKF is the way to construct the model error covariance. It proposes a Monte Carlo approximation of the model error by means of an ensemble of model state (Evensen (2003)). For this, a large number of realisations of the uncertain model variables are generated following a prior distribution. These realizations propagate to a set of model state vector during the forward model integration. In this way, errors due to uncertain model variables are propagated to the error of the model state vector. The set of model state vector is called ensemble, hence the name of the EnKF. The number of the set is called ensemble size and each model state vector in the set is called ensemble member. The ensemble continues to propagate at each time step of the model integration and represents the model error by means of a (Gaussian) distribution (Figure 4.4). The mean of the ensemble is

taken as the mean model state and the covariance of the ensemble corresponds to the model error covariance. The choice of the ensemble size is a trade-off between a sufficient representation of the model error and the computational burden. The nominal ensemble size in oceanic applications is 100. In case of a high dimensional model state vector and limited computational resources, the solution consists of generating a large ensemble in a first time and then performing a SVD to reduce the ensemble size without loss of useful information (Yan et al. (2014)).

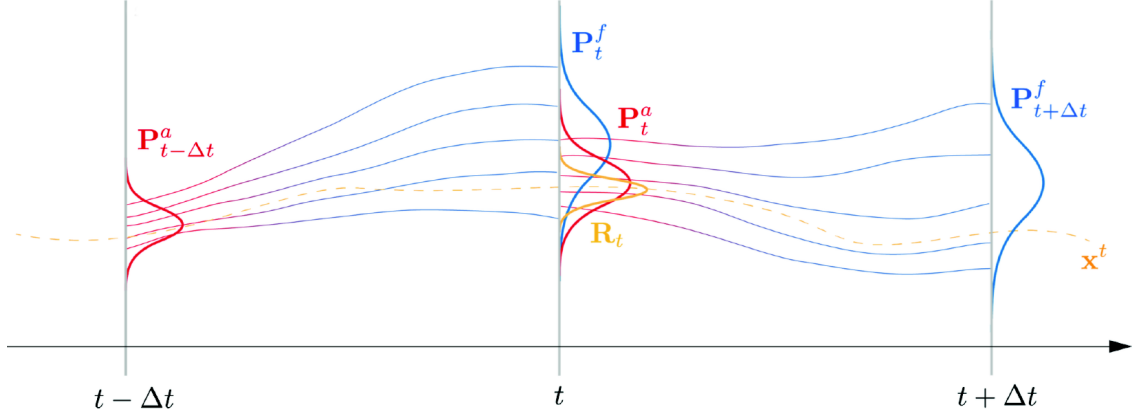


Figure 4.4 – Simplified illustration of the EnKF. Each line corresponds to an ensemble member and a set of lines represent a distribution. The blue lines represent the error propagation through free model integration at the forecast step. The red lines represent the correction by observations with error covariance R (yellow distribution) at the analysis step. x^t represents the true state (Bato (2018)).

Starting from an initial condition, EnKF performs the forecast step and the analysis step in an iterative way.

Forecast step The forecast step consists of predicting the model state vector value from its value at the previous time step and is carried out by the model integration under the control of the model operator (equation 4.21, Figure 4.4). This step is performed for each ensemble member.

The forecast of the model state is given by the ensemble mean of the forecast, while the forecast error covariance is given by the covariance of the ensemble as follows :

$$\bar{x}^f = \frac{1}{N} \sum_{i=1}^N x_i^f \quad (4.14)$$

$$P^f = \frac{1}{N-1} (x^f - \bar{x}^f)(x^f - \bar{x}^f)^T \quad (4.15)$$

with f denoting forecast and N the ensemble size.

Analysis step At the analysis step, the model state vector obtained at the forecast step is updated by the data observations in order to obtain an estimate of the model state with improved accuracy, namely analysis (Figure 4.4). The relative contribution of the model forecast and the data observations to the estimation of the analysis is determined based on their error covariance. Large errors correspond to small contributions. For this, the kalman gain is computed as follows,

$$K = P^f H^T (H P^f H^T + R)^{-1} \quad (4.16)$$

For each ensemble member, the model state vector is updated in the following way

$$x^a = x^f + K(y - Hx^f) \quad (4.17)$$

with a denoting analysis and f denoting forecast.

The analysis of the model state and the analysis error covariance are given by,

$$\bar{\mathbf{x}}^a = \frac{1}{N} \sum_{i=1}^N \mathbf{x}_i^a \quad (4.18)$$

$$P^a = \frac{1}{N-1} (\mathbf{x}^a - \bar{\mathbf{x}}^a)(\mathbf{x}^a - \bar{\mathbf{x}}^a)^T \quad (4.19)$$

Indeed, the analysis error covariance can also be deduced from the forecast error covariance, that is,

$$P^a = P^f - K H P^f \quad (4.20)$$

According to equation 4.20, the variance of the analysis is inherently smaller than that of the forecast, which implies the improvement of the model state vector that should be provided by data assimilation (even though it cannot be the case sometimes). That is why the specification of the model error covariance and the observation error covariance should be as accurate as possible in order that the analysis error covariance represents the reality. Indeed, the problem of underestimation of the analysis error covariance often occurs in EnKF, due to inappropriate model error specification. This problem can further result of ensemble collapse, i.e. ensemble members converge to one single member. A common solution consists of empirically applying an inflation factor (e.g. in the range of [1.05, 1.1]) to the analysis error covariance at each time step. Afterwards, the analysis of the model state vector is used as an updated initial condition to restart the forward model integration in order to produce the forecast for the next time step. In this way, a new iteration of the forecast step and then the analysis step begins, and so on.

Case study

Data assimilation, in particular EnKF, has been proposed, for the first time in volcanology, to predict magma chamber over-pressure that is one of the key parameters to infer an impending effusive eruption, in the Ph.D thesis of Mary Grace Bato. Very promising results have been obtained in the study of the inter-eruptive and post-eruptive activities of the Grímsvön volcano located in Iceland during the period of 2004 - 2016, which confirms the capability of data assimilation in following up the dynamical volcanic system roots and in near-real-time volcanic forecasting.

Dynamical model The two-chamber magma model proposed in (Reverso et al. (2014)) (Figure 4.5), which is a simple and generic dynamical model for the magma plumbing system, was used. This model consists of two reservoirs embedded in an elastic medium and connected by a hydraulic pipe. The deeper reservoir is assumed to be fed by a constant magma inflow, which corresponds to the bottom boundary condition of the system. This model is characterized by a set of geometrical and rheological parameters and solves for the temporal evolution of the magma over-pressures for the shallow and the deep reservoirs respectively. As shown by Reverso et al. (2014), this simple model provides a consistent explanation for the temporal evolution of the post-eruptive displacement measured at Grímsvön volcano after the three last eruptions (1998, 2004 and 2011).

In this model, the values of the over-pressure within the shallow and deep reservoirs, respectively, ΔP_s and ΔP_d , at a given time, t_{n+1} , are derived from their values at the previous time step, t_n , using the following discrete time step equations,

$$\frac{\Delta P_s(t_{n+1}) - \Delta P_s(t_n)}{t_{n+1} - t_n} = \frac{Ga_c^4}{8\mu H_c a_s^3} ((\rho_r - \rho_m)gH_c + \Delta P_d(t_n) - \Delta P_s(t_n)) \quad (4.21)$$

$$\frac{\Delta P_d(t_{n+1}) - \Delta P_d(t_n)}{t_{n+1} - t_n} = \frac{G}{\pi a_d^3} Q_{in} - \frac{\gamma_s a_s^3}{\gamma_d a_d^3} \frac{\Delta P_s(t_{n+1}) - \Delta P_s(t_n)}{t_{n+1} - t_n} \quad (4.22)$$

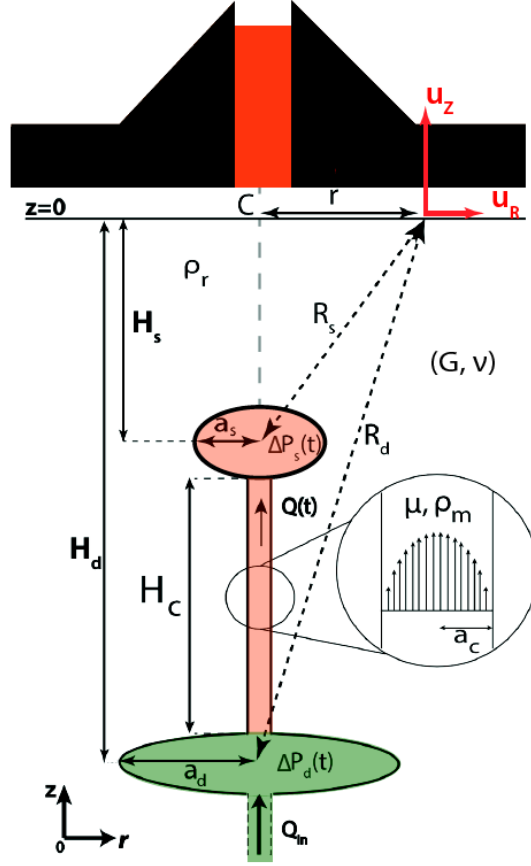


Figure 4.5 – Schematic sketch of the two-chamber magma model. The magma inflow rate at the bottom reservoir Q_{in} and the radius of the deep reservoir a_d are the two parameters considered to be uncertain in this study. Observations (vertical and horizontal displacements) are recorded at the surface at a given location S characterized by its distance r from the center of the volcanic system C . $R_s = \sqrt{r^2 + H_s^2}$ and $R_d = \sqrt{r^2 + H_d^2}$ are distances between S and the respectively (Bato (2018)).

with a_c the radius of the conduit, a_d the radius of the deep reservoir, a_s the radius of the shallow reservoir, H_s and H_d the depth of the shallow and deep reservoirs respectively, G the shear modulus, μ the viscosity of the magma, ρ_r the density of the host rock, ρ_m the density of the magma, g the gravity, Q_{in} the magma inflow rate in the deep reservoir, γ_s and γ_d two scaling factors for volume-pressure relationship depending on the shape of the reservoir, 1.0 for a Mogi point (sphere) source and $8(1 - \nu)/3\pi$ for a sill.

Based on the Mogi model, the radial displacement, u_R , and the vertical displacement, u_z , observed at the surface can be expressed as :

$$u_R(t) = \frac{1 - \nu}{G} r \left(\alpha_s \frac{a_s^3}{R_s^3} \Delta P_s(t) + \alpha_d \frac{a_d^3}{R_d^3} \Delta P_d(t) \right) \quad (4.23)$$

$$u_z(t) = \frac{1 - \nu}{G} r \left(H_s \alpha_s \frac{a_s^3}{R_s^3} \Delta P_s(t) + H_d \alpha_d \frac{a_d^3}{R_d^3} \Delta P_d(t) \right) \quad (4.24)$$

where ν is the Poisson's ratio, α_s and α_d are two scaling factors for displacement-pressure relationship depending on the shape of the reservoir, with value of 1.0 for a Mogi point source and $4H_s^2/\pi R_s^2$, $4H_d^2/\pi R_d^2$ respectively for a sill.

Equations 4.23 and 4.24, showing the relationship between the surface displacements and over-pressures of the shallow and deep reservoirs, provides a link between the data observations and the model state variables, a key element of data assimilation.

Ensemble generation According to volcanic expert's knowledge, in a first approximation, the model error of the two-chamber magma model mainly results from two uncertain model parameters, the magma inflow at the bottom of the system Q_{in} and the radius of the deep reservoir a_d . The ensemble members are thus generated from these two uncertain model parameters in order to represent as accurately as possible the model error. Gaussian distributions are considered for these two parameters, because 1) no information about the real distribution is available 2) EnKF provides optimal results in case of Gaussian distributions. More precisely, two types of distributions are generated, including, 1) a truncated Gaussian distribution wherein the mean is centered on the nominal value of the uncertain parameter, namely unbiased case; 2) a truncated Gaussian distribution that does not include the nominal value of the uncertain parameter with the mean being very far away from the nominal value, namely biased case. Gaussian distributions are truncated to ensure the physical sense of the parameters. The nominal values of Q_{in} and a_d are obtained from the MCMC inversion (Figure 4.3). The ensemble size is set to 1000. Here, a large ensemble size is possible, thanks to the small dimension of the model state vector.

Data observations Data observations include essentially displacement time series measured by GNSS. These displacement measurements are characterized by high temporal sampling (daily) and low spatial coverage (only one GPS station). InSAR displacement measurements, with high spatial coverage but relatively low temporal sampling (e.g. 12 days) are not available because of snow covers over the Grímsvötn volcano. However, InSAR displacement time series are simulated in order to highlight the impact of the spatial distribution and the temporal sampling of data observations on the assimilation performance in case of synthetic simulations. In Figure 4.6, the daily 3D

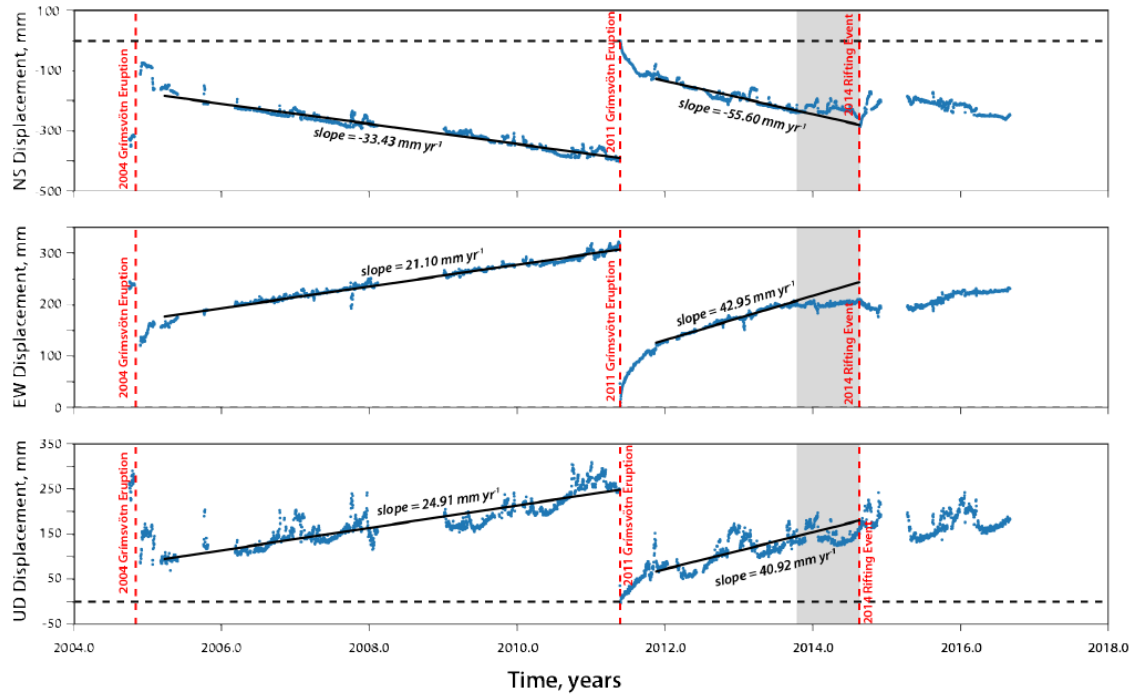


Figure 4.6 – GPS time series measured at GFUM station from 30 Sep 2004 to 01 Sep 2016. The blue dots are the actual data. The red broken lines mark the 2004 and 2011 Grímsvötn eruptions as well as the 2014 major rifting event. The black solid lines are the linear fit to the linear part of each post-eruptive event. The black broken lines are shown as a reference for the zero-displacement value. The shaded gray area corresponds to the assumed shift from linear to constant trend around 10 months before the 2014 rifting event. Note that the vertical component of the time series is not corrected for either glacial isostatic adjustment (GIA) or seasonal effects. The horizontal component is however, corrected for tectonic trend (Bato (2018)).

surface displacement observed at GFUM station from 30 September 2004 to 1 September 2016 at

Grímsvötn volcano is shown. The eruption events are marked by discontinuities. The nominal errors of these displacement are 1 mm and 10 mm for horizontal and vertical displacements respectively. Given the symmetry of the volcanic model, one GPS point is sufficient to constrain the model parameters.

Experiment setup Two cases are considered, 1) state estimation 2) state - parameter estimation. In the case of state estimation, the state vector includes the over-pressures in the shallow and deep reservoirs, $\mathbf{x} = [\Delta P_s, \Delta P_d]$. Only the evolution of the over-pressures in the shallow and deep reservoirs is tracked. In the case of state-parameter estimation, besides the over-pressures, the evolution of the magma inflow rate, Q_{in} , is also tracked, the state vector is thus $\mathbf{x} = [\Delta P_s, \Delta P_d, Q_{in}]$. Unlike the over-pressures, the magma inflow rate is not directly related to the eruption, but the follow up of its temporal evolution gives insights into the volcanic system roots, which information cannot be retrieved by other classical methods such as inversion.

The initial values of over-pressures are set to zero, assuming that both reservoirs had been fully depressurized by the previous eruption. The initial value of the magma inflow rate is obtained from the MCMC inversion (Figure 4.3). Data assimilation is performed every day when the GNSS displacement measurement is available. In synthetic simulations, other assimilation windows, e.g. 12 days, have also been tested to highlight its impact on the assimilation results.

Real data application We have mainly investigated the 2004-2011 inter-eruptive data set, the 2011 post-eruptive data set and 2014-2015 eruptive data set at the Grímsvötn volcano in Iceland in the Ph.D thesis of Mary Grace Bato.

Figure 4.7 and Figure 4.8 illustrate the results of sequentially assimilating the radial displacement by EnKF in the 2004-2011 inter-eruptive period. Both the over-pressures and the time varying uncertain parameter Q_{in} can be closely followed with data assimilation. For a comparison purpose, the free run of the model (only model prediction, without data assimilation) is also presented. Indeed, the free run of the model have already provided satisfactory results for the prediction of the over-pressures and the radial displacement, because the uncertain model parameters were well constrained by the MCMC inversion using the initial part of the data set. However, the free run of the model seems insufficient in predicting the evolution of the magma inflow rate, Q_{in} , which implies that inversion only cannot be able to track the evolution of the magma inflow rate.

Assuming a statistical distribution of the threshold magma over-pressure leading to reservoir wall ruptures, the prediction of the over-pressures can be used to estimate the timing of an impending eruption. A Gaussian distribution of the failure over-pressure, ΔP_f , with the mean value of 44 MPa and the standard deviation (σ) of 11 Pa was considered, based on previous records (Albino et al. (2010, 2018)), to forecast the rupture of the shallow magma chamber. Several eruption zones have thus been introduced based on the evolution of the shallow over-pressure, ΔP_s , at each time step,

- No eruption zone, with $0 \leq \Delta P_s \leq \Delta P_f - 2\sigma$
- Sub-critical zone, with $\Delta P_f - 2\sigma < \Delta P_s \leq \Delta P_f - \sigma$
- Critical zone, with $\Delta P_f - \sigma < \Delta P_s \leq \Delta P_f$
- Super-critical zone, with $\Delta P_s > \Delta P_f$

To compute the probability of the rupture, we first assign a failure over-pressure at $t = 0$ for each ensemble member, these values are drawn randomly from the Gaussian distribution previously mentioned and considered as the reference failure over-pressure that remains constant over time. Then at each time step, the probability of rupture is calculated as the percentage of ensemble members that exceed the assigned reference failure over-pressure value. Forecasts can be provided in the form "an eruption might occur within the next N_{\min}^{\max} days.

According to Figure 4.9, the mean over-pressure that triggered the 2011 eruption is 38.09 MPa. Before the eruption, all the ensemble members were already in the critical state with a probability

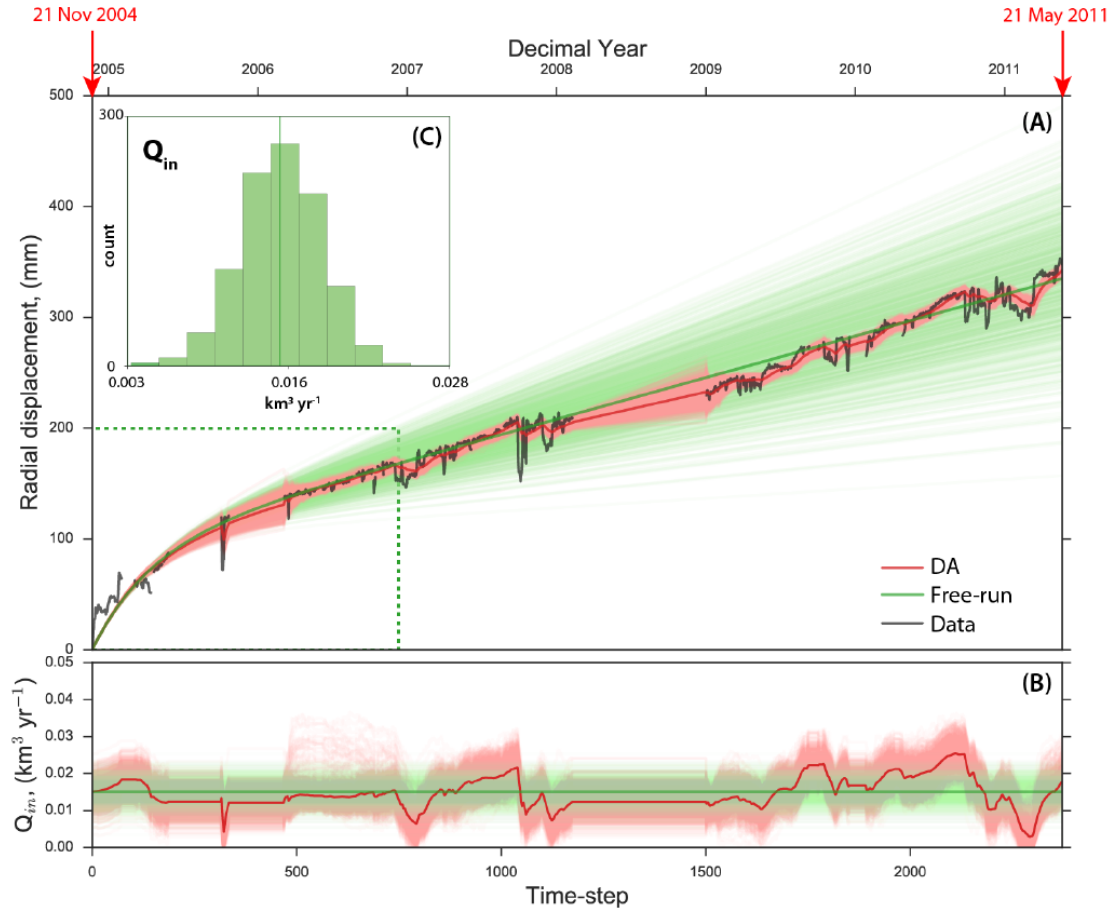


Figure 4.7 – A) Entire 2004-2011 inter-eruptive radial data set (black) and the resulting data fits by : 1) free run of the model (green) and 2) data assimilation with EnKF (red). The green dotted box covers the data set used to estimate the non-evolving uncertain parameters by inversion. B) estimated magma inflow rate, Q_{in} , as a function of time using : free run (green) and EnKF (red). (C) prior distribution of Q_{in} used for ensemble generation in the unbiased case. (Bato (2018))

of rupture equal to $\sim 24\%$. With further tests using different values for the non-evolving uncertain parameters (to avoid the possible dependence of the probability of the rupture on the initially fixed non-evolving uncertain parameters), we concluded that when $25\% \pm 1\%$ of the ensemble exceeded the failure over-pressure, an actual eruption is imminent. Further details about how to estimate the timing, N_{min}^{max} , can be found in Bato (2018). All the results previously shown, as well as those not shown here but in Bato (2018), confirm the capability of data assimilation (i.e. EnKF) in near-real-time forecasting.

The investigation of the 2011 post-eruptive data set until and after the 2014 rifting event is shown in Figure 4.10. Different from the 2004-2011 inter-eruptive case (Figure 4.7), a decreasing trend of the magma inflow rate is observed between 2013 and 2014. Data assimilation enabled us to closely follow this trend. We obtained a minimum rate of $0.007 \text{ km}^3 \text{yr}^{-1}$, which corresponds to a drop of $0.039 \text{ km}^3 \text{yr}^{-1}$ relative to its prior value.

The analysis of the probability of rupture also showed that just before the 2014 rifting event, Grímsvötn's shallow magma reservoir was already at the critical stage of rupturing and could have erupted in 2015. However, no eruption has occurred, suggesting that a transient event may have happened and postponed the supposed eruption. This transient event has been evidenced by the observation of the decreasing of the magma inflow rate mentioned previously, the latter corresponding to the interplay between the Grímsvötn volcano and the nearby Bárðarbunga volcano (Bato et al. (2018)). We were able to estimate that the magma inflow beneath Grímsvötn dropped

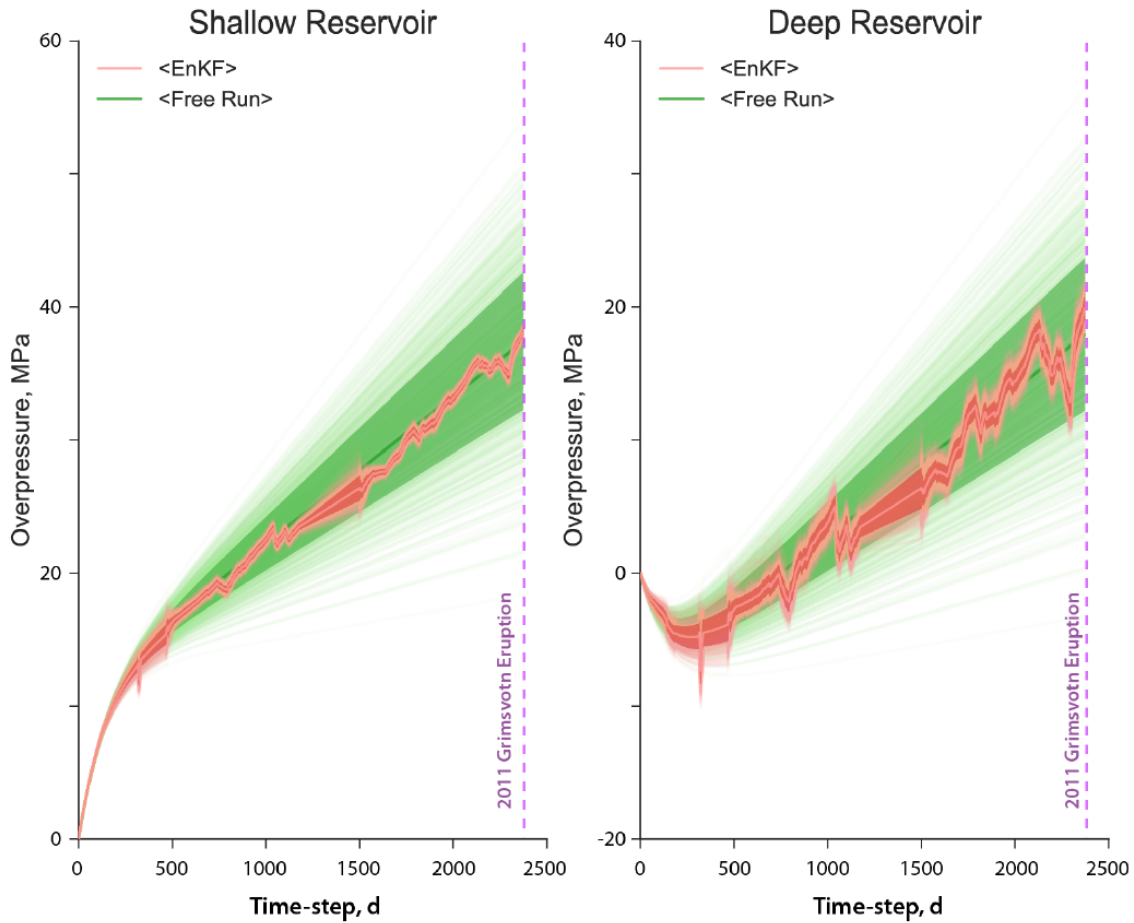


Figure 4.8 – Over-pressures of the shallow and deep reservoirs obtained with EnKF (red) in the 2004-2011 inter-eruptive period. The corresponding data fit is illustrated in Figure 4.7. The pink color represents each ensemble member and the dark red shade is the standard deviation of the ensemble distribution (also called ensemble spread). It follows that the pink line within the dark red shade is the mean of the ensemble. The light green colors are the ensemble members of the free run and the darker green shade is the ensemble spread. The purple broken lines mark the 2011 eruption. (Bato (2018))

up to 85% during the 10 months preceding the initiation of the Bárðarbunga rifting event. The loss of at least $0.016 \text{ km}^3 \text{ yr}^{-1}$ in the magma supply of Grímsvötn is interpreted as a consequence of magma accumulation beneath Bárðarbunga and subsequent feeding of the Holuhraun eruption 41 km away. This transient event might have postponed Grímsvötn's supposed eruption in 2015.

The results of the 2011 post-eruptive data set and the 2014-2015 eruptive data set go beyond volcanic eruption forecasting and showcase the capability of EnKF to track parameters that can suddenly fluctuate in time and to give insight into the volcanic system roots.

Synthetic simulations The impact of the temporal sampling and spatial distribution has been investigated through synthetic simulations. The main findings show that both GNSS and InSAR data sets are able to track the true behaviour of the shallow and deep over-pressures. However, when it comes to estimating the uncertain model parameters, Q_{in} and a_d at the same time, only the InSAR-type data allow the convergence of to their true values. The challenge remains with the temporal sampling of InSAR data. InSAR data fail when the assimilation is performed every 12 days (sampling interval of Sentinel-1 data). The advantage of using GNSS data to capture the behavior of the over-pressures is its high temporal sampling (e.g. daily or even hourly). InSAR data on the other hand, are less frequent to acquire but provide better spatial coverage and constraints on the uncertain parameters. In order to exploit the advantages of both data sets, it is recommended

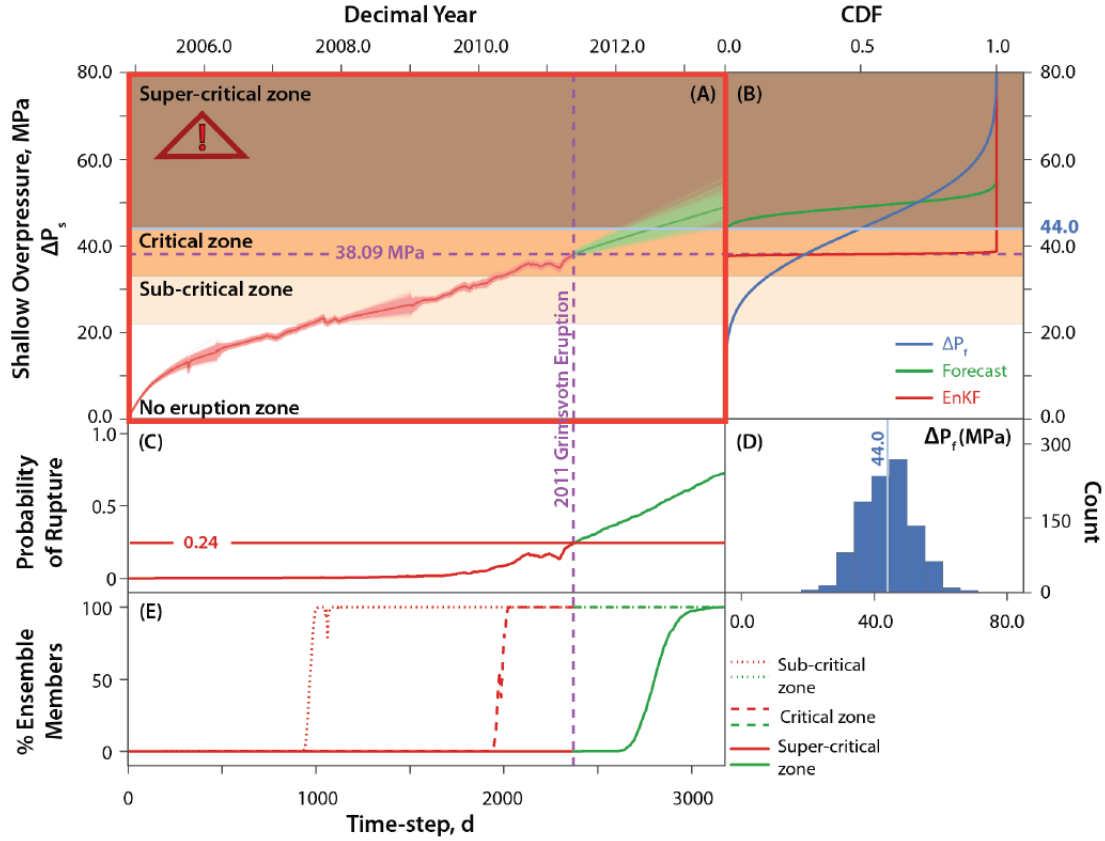


Figure 4.9 – (A) Evolution of the EnKF-derived shallow over-pressure constrained by the initial part of the 2004-2011 radial displacement data set (i.e. Figure 4.7), embedded on the eruption zones. (B) cumulative distribution function (CDF) illustrating the failure over-pressure (blue) as well as the over-pressures at the end of the assimilation (red) and at the end of free run (green). (C) probability of rupture calculated from the percentage of ensemble members that exceeded the reference failure over-pressure randomly drawn from the distribution in (D). (E) percentage of ensemble members entering each eruption zone as a function of time. (Bato (2018))

to jointly assimilate the GNSS-like and InSAR-like data.

The impact of the position of the data observation with respect to the volcano axis has also been studied. The near field displacement signals are mostly related to the shallow reservoir whereas at farther distances (i.e. > 16 km and > 10 km for the radial and vertical displacements, respectively), the displacement signals become dominated by the deep reservoir. Given this, we can infer that far-field data can bring more information about the deep reservoir but note also that going farther away from the volcano axis, the signal-to-noise ratio weakens. Therefore, careful attention should be paid when assimilating far field data to distinguish between deep reservoir activities and noise presented in the data.

The impact of the prior distribution of uncertain model parameters used for ensemble generation, i.e. the previously mentioned unbiased and biased cases, on the prediction of the shallow and deep over-pressures, as well as the uncertain model parameters is small, as long as the assimilation duration is sufficiently long and data observations are sufficiently accurate. In the biased case, the assimilation results succeed in converging to the true values after a while along the assimilation period, even though large fluctuations are observed at the beginning of the assimilation. However, notice that the over-pressure in the deep reservoir is more likely to be affected by a poorly specified prior distribution of uncertain model parameters. If this happens, the prediction of the vertical displacement is also biased and the bias is more pronounced going farther away from the volcano axis.

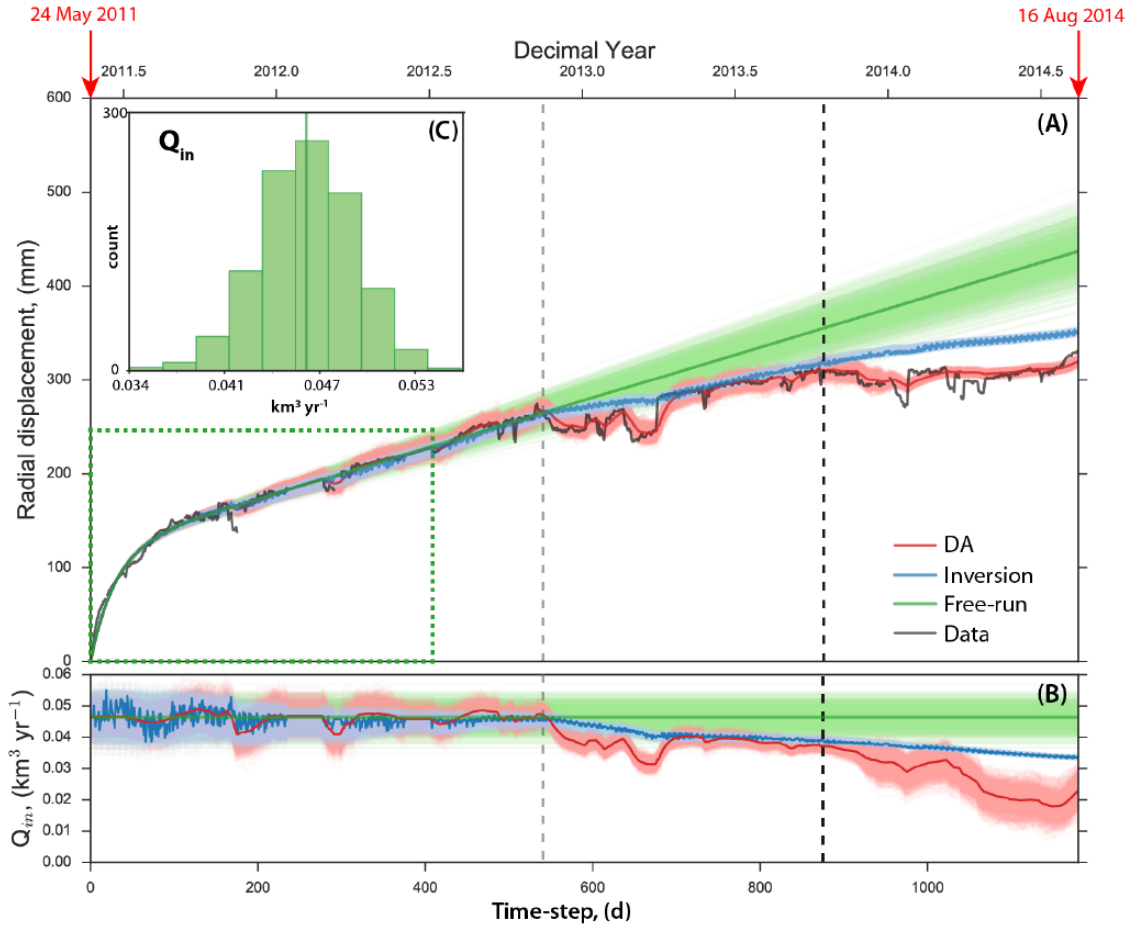


Figure 4.10 – A) Entire 2011 post-eruptive data set (black) and the resulting data fits by : 1) free run of the model (green), 2) MCMC inversion (blue), and 3) data assimilation with EnKF (red). The green dotted box covers the data set used to estimate the non-evolving uncertain parameters. B) estimated magma inflow rate, Q_{in} , as a function of time using : free run (green), EnKF (red) and MCMC (blue). Note that the gray and black broken lines (Figure 4.10 A and B) correspond to the points where a decreasing trend in Q_{in} , tracked with EnKF, are observed. C) prior distribution of Q_{in} used for free run, data assimilation and inversion (Bato et al. (2018)).

4.2.3 Discussions

Inversion estimates geophysical parameters in static contexts (i.e. the estimated geophysical parameters do not evolve in time), while data assimilation can do the geophysical parameters estimation job in dynamical contexts. Data assimilation thus outperforms inversion in following up time-varying geophysical parameters. Inversion works with prior distributions of unknown geophysical parameters (uniform distribution in case of no information) and data observations. Data assimilation requires initial conditions of model parameters, prior distributions of uncertainty model parameters and data observations. Taking aside the specific research objective and constraints of the static or dynamical context, practically, we use inversion when the geophysical parameters of interest are unknown and data assimilation when the geophysical parameters of interest are uncertain. Using inversion to estimate initial conditions for data assimilation as done in Bato et al. (2018) represents an excellent idea.

Not explicitly stressed in section 4.2.2, Bayesian inference also constitutes the foundation of data assimilation. Both stochastic data assimilation methods (e.g. EnKF, Particle Filter) and variational data assimilation methods (e.g. 4D-var) are based on the Bayesian formulation given in equation 4.3. In EnKF, Gaussian distributions are assumed for error statistics. At each analysis step, both the

prior pdf and likelihood are Gaussian (equation 4.5), the most likely model parameters are obtained by maximising the posterior pdf by solving an optimization problem. The optimal estimator, known also as the best linear unbiased estimator (BLUE), gives the solutions in equations 4.16, 4.17 and 4.20. Therefore, inversion and data assimilation are closely connected : EnKF performs inversion in a sequential way.

Despite the widespread applications and remarkable achievement in geophysical parameters estimation and prediction, model-driven inversion and assimilation approaches exhibit some shortcomings : 1) Overly simplistic solutions are frequently adopted in geophysical modelling, in particular in case of limited understanding of the underlying physical processes. Moreover, the quantification of the model error is tremendously difficult, even impossible. 2) The overwhelming amount of computing resources of Bayesian inversion quickly goes beyond any feasible real time potential, in particular in case of large (spatial and temporal) scale imaging applications. 3) Partial observations that do not cover the full model parameter space are available in lots of cases. Remind that InSAR and offset tracking provide displacement measurements with a temporal sampling of several days while GNSS provides displacement measurements over isolated points. There is not yet satellite cancellation that comes up with both high spatial and temporal sampling rate. 4) Difficulty exists in specifying an appropriate prior distribution of model parameters, because accurate prior knowledge is not always available. Poorly specified prior distributions can play an important role in the reliability of the final results. 5) The solutions, including prior distribution and regularisation designing, are often case dependent, thus have no extensive universality and suitability in general. For all these reasons, data driven approaches presented in the following section can provide important alternative solutions.

4.3 Data driven approaches

The recent advent of neural networks based machine learning paradigms enables the development of new solutions to tackle the previous shortcomings of model-driven inversion and prediction problems.

In contrast to physical model based approaches, neural networks based methods are highlighted by the following features : 1) the use of generic models but adapted to specific problems through automatic learning against training data. 2) free from prior knowledge about the phenomenon under observation and statistical hypotheses made on model parameters and/or data observations. Nevertheless, neural networks can also take prior knowledge into account as network structural constraints and regularization terms. 3) capable of finding non-linearity in the solution that we were unaware of in the theory and hidden regularities in the data that we have overlooked. 4) capable of dealing with data/model complexity such as high dimension, implicit relationship between data and model parameters, partial knowledge on physics.

For example, in Laloy et al. (2018), GANs have been incorporated into a MCMC approach in an hydrological inversion to overcome the difficulty in choosing an appropriate prior and to reduce the expensive computational effort. In this work, GANs have been used to define a low dimensional representation of the original high dimensional data. Following this, the model parameters research space was much reduced. In this way, the inversion by MCMC could be performed within a low-dimensional space, thanks to which, the efficiency of the MCMC inversion has been significantly improved. In Laloy et al. (2019), the same authors further improved the computational cost by replacing the MCMC by gradient-based deterministic methods (e.g. quasi-Newton gradient descent and Gauss-Newton). In Mosser et al. (2018), GANs have been deployed to formulate the seismic forward and inverse processes with synthetic simulations. In Jacquemont et al. (2021), deep multitask learning is used for inverse problems in astrophysics for gamma ray

parameters estimation. RNN relying on LSTM cells have been deployed to predict earthquake trends and structural seismic response from historical data in Vardaan et al. (2019), Zhang et al. (2019). CNNs, as well as hybrid CNN-LSTM, have been used with success for climate predictions (e.g. precipitation forecast, hurricane forecast, etc.) (Giffard-Roisin et al. (2020), Shi et al. (2015)). Note further that, in physical model based inversion, a first set of key model parameters that control the data observation are identified beforehand often based on previous studies or experts' experience. The main role of inversion is thus to determine model parameters values and there is no need to identify key model parameters in inversion. Therefore, in case of unidentified key model parameters, semi-blind or blind inversion becomes impossible. With the advance of neural networks, it is possible to solve a model parameters disentanglement problem (i.e. key model parameters identification) by unsupervised learning (Locatello et al. (2019)). This is really important for geophysical targets for which not much work has been realised for diverse reasons.

All these neural networks based proof-of-concept studies highlight the interest of neural networks based methods compared to the traditional physics based methods and open new perspective for geophysical parameters inversion and prediction with SAR displacement time series where large amounts of spatial and time-varying data are available but no neural networks based methods have so far been published.

4.4 Conclusion & perspectives

Inversion constitutes the unique solution to get insights into the subsurface geological structures that induce the displacement observed at the Earth's surface. Model driven inversion methodologies have been developed since a very long time in geophysical community and have been firmly established nowadays. Advanced but standard inversion methods such as Bayesian inversion, have widely been used as routine methods in numerous studies of earthquakes, volcanoes, etc. Actually, the advance of geophysical modeling constitutes a key factor that potentially limits the further development of model driven inversion methodologies.

Data assimilation can also be considered as the unique solution for near-real-time forecasting of key geophysical parameters that are strongly related to natural hazards and for getting insights into the non-observed subsurface dynamical system roots. Recently proposed to volcanology (Bato et al. (2017, 2018)) and to glaciology (Gillet-Chaulet et al. (2016)), data assimilation still has large development prospect in these two domains, as well as in operational monitoring of landslides, slow slip events, etc., for which vast stream of displacement time series is available. Achievement of methodological development in data assimilation in the atmosphere-ocean community is worthy of fully exploiting in order to be beneficial to operational displacement estimation and natural hazard prediction. In the Ph.D thesis of Mary Grace Bato, we confirmed the capability of data assimilation (i.e. EnKF) to predict the probability of a volcano to erupt, based on the tracking of the over-pressures in the magma chambers. Then, the new question is when and where the magma arrives at the Earth's surface, given the rupture of a magma chamber. To answer this question, another Ph.D thesis is being set up, with the objective to predict the location and timing of eruptive vents induced by magmatic intrusion propagation by means of Partial Filter.

Besides further investigation of data assimilation, I'm also interested in neural networks based data driven approaches for inversion and prediction problems. To tackle inversion and prediction issues by means of neural networks will complement significantly the common physics based approaches and enlarge undoubtedly the scientific insights in the geophysical community. Moreover, this meets entirely the actual opportunity and also challenge for huge and regular SAR satellite data exploitation and opens new perspectives for neural networks based data-driven methods in SAR satellite data exploitation. This work constitutes a work package in my ANR young researcher

project. Collaborations with colleagues specializing in deep learning will be started in order to propose novel recursive neural networks models with both linear and nonlinear functionalities, adapted to the SAR displacement data specificity (i.e. spatial and time varying data), by combining GAN and LSTM (or alternatives such as causal convolutional networks) for physical parameters inversion and prediction problems. Prior physical knowledge (e.g. model parameter value range, covariance structure, etc.) will be incorporated into the neural networks in order to enhance the learning process and to improve the interpretability (be able to predict what is going to happen, given a change in input or algorithmic parameters) and explainability (be able to explain the internal mechanics of a neural networks system). A particular effort will be made on the understanding of the neural network functioning in order to ensure the accountability and then the actionability of the results for operational use. The ultimate objective consists of the synergistic exploitation of both model driven and data driven approaches.

Conclusions & perspectives

In this report, I summarized my research works around SAR image exploitation for displacement measurement and geophysical parameters estimation, as well as related state-of-the-art works, in line with four research directions organised according to four different scientific objectives : displacement estimation from SAR image time series, missing data imputation in SAR/optical displacement time series, displacement time series analysis and geophysical parameters estimation and prediction.

Past, ongoing and future works in each research direction have been discussed. For displacement measurement from SAR images, my interest lies in the multi-temporal InSAR approaches. With the past experience of applications and a thorough study of the state-of-the-art multi-temporal InSAR approaches, I decided to propose new approaches to respond to operational monitoring requirement. A recursive and robust multi-temporal InSAR approach, able to integrate SAR images in a gradual way and take the non Gaussian data statistics into account, is being established in the Ph.D thesis of Viet Hoa Vu Phan, in collaboration with colleagues specializing in statistical signal processing, in particular in robust and recursive covariance matrix estimation. For missing data imputation in SAR/optical displacement time series, two approaches, namely EM-EOF and extended EM-EOF, based on EOF decomposition of the temporal and spatio-temporal covariance of displacement time series in an EM scheme have been proposed in the Ph.D thesis of Alexandre Hippert-Ferrer. Indeed, the missing data problem in SAR displacement time series was addressed for the first time in the Ph.D thesis of Alexandre. Missing data issues being trivial, plays an important role in the reliability and completeness of displacement measurements. The perspective of the EM-EOF and extended EM-EOF approaches corresponds to parametric approaches that aim to estimate first-order and/or second-order statistical parameters of the distribution that describe the data directly from incomplete data observations in an EM scheme. The interest of parametric approaches lies not only in the capacity of dealing with any data distribution independent of applications, but also in the possibility of recursive implementations (i.e. recursive estimation of covariance matrix) that opens perspectives for operational processing. For displacement time series analysis, I presented data-driven and statistical model driven approaches for displacement measurement fusion with the objective to provide a consistent and easily interpretable displacement time series, for displacement signal separation from other perturbations and for automatic displacement signal detection from large data sets such as global volcano monitoring. An on-going Ph.D thesis is focused on the offset tracking displacement measurements fusion to improve the reliability and completeness. Given the background of the Ph.D student (geology/geophysics), the standard least-square inversion has been chosen as the baseline method and efforts are made to deal with remaining open issues such as data weighting, choice of temporal baselines, multi-sensor displacement measurements fusion, etc. For geophysical parameters estimation and prediction, model driven inversion and data assimilation methodologies have been introduced. Works carried out in the Ph.D thesis of Mary Grace Bato, being pioneering works deploying data assimilation in volcanology, have been presented. Perspectives to further exploit data assimilation for volcanic hazard prediction and to tackle the problem of geophysical parameters estimation and prediction by means of neural networks based approaches have been discussed. A synergistic deployment of both model driven and data driven inversion and prediction methodologies constitutes the future work that I want to develop in the coming years.

Thanks to my multidisciplinary experience, my research activities spread over a large spectrum of subjects. Certainly, my multidisciplinary experience is beneficial from the point of view that it allows me to acquire skills in different research fields, somehow enlarges my research vision and makes it possible to jointly exploit advances in different scientific areas to solve the problem of interest. However, the drawback of this multidisciplinary experience is also obvious, that is, I'm not an expert in any research direction. Therefore, I do not intend to diversify my research works any more. On one hand, my efforts are made to keep the methodological consistency in my future research works. For instance, for the development of a recursive and robust multi-temporal InSAR approach and the development of parametric approaches for missing data imputation, the common key methodology behind consists of recursive and robust estimation of the covariance matrix. The only difference lies in the data type and the inherent structure of the covariance matrix. In case of the multi-temporal InSAR approach, we deal with complex valued SAR images and the inherent structure of the covariance of SAR image time series is strongly related to the temporal decorrelating property, but can be expressed by a Kronecker product in a general way. In case of missing data imputation, we handle real valued displacement time series and the inherent structure of the covariance of displacement time series is often low rank. Displacement time series analysis in particular displacement measurements fusion, inversion and data assimilation can also be grouped together according to the common methodology : synergistic deployment of data and (statistical and/or physical) model. In my opinion, there are very few or even no pure data driven approaches in fact. To my knowledge, most state-of-the-art data driven approaches are based on statistical and/or mathematical models, a hidden model that describes the process or phenomenon under observation being retrieved based on data observations. Neural networks based approaches, the most likely pure data driven approaches, are indeed based on a large number of mathematical models. The common key elements of all data and model fusion methodologies include the weight of each contribution and the optimization strategy to resolve an estimation problem. On the other hand, my efforts are made to jointly deploy my previous, ongoing and future works in the aforementioned four research directions to promote operational monitoring of natural hazards by means of SAR images. Indeed, each of the four research directions constitutes a processing step in a natural hazard monitoring chain : estimate displacement measurements from SAR image time series, improve the completeness of the previously obtained displacement measurements, analyze displacement measurements to extract consistent and reliable displacement information, estimate and predict the key geophysical parameters related to natural hazards from previously improved displacement measurements. Of course, my contribution will only be one of the efforts towards operational monitoring of natural hazards. There is still a long way to go for both operational monitoring of natural hazards and my scientific carrier.

Bibliographie

- F. Albino, V. Pinel, and F. Sigmundsson. Influence of surface load variations on eruption likelihood : Application to two icelandic subglacial volcanoes, grímsvotn and katla. *Journal of Geophysical Research : Solid Earth*, 181(3) :1510 – 1524, 2010.
- F. Albino, F. Amelung, and P. Gregg. The role of pore fluid pressure on the failure of magma reservoirs : insights from indonesian and aleutian arc volcanoes. *Journal of Geophysical Research : Solid Earth*, 123(2) :1328–1349, 2018.
- A. Alvera-Azcarate, A. Barth, J-M Beckers, and R. H. Weisberg. Multivariate reconstruction of missing data in sea surface temperature, chlorophyll, and wind satellite fields. *J. Geophys. Res.*, 112(C03008), 2007.
- N. Anantrasirichai, J. Biggs, F. Albino, P. Hill, and D. Bull. Application of machine learning to classification of volcanic deformation in routinely generated insar data. *Journal of Geophysical Research*, 123(8) :6592–6606, 2018.
- N. Anantrasirichai, J. Biggs, F. Albino, and D. Bull. A deep learning approach to detecting volcano deformation from satellite imagery using synthetic datasets. *Remote Sensing of Environment*, 230(111179), 2019a.
- N. Anantrasirichai, J. Biggs, F. Albino, P. Hill, and D. Bull. The application of convolutional neural networks to detect slow, sustained deformation in InSAR time series. *Geophysical Research Letters*, 46 :11850–11858, 2019b.
- H. Ansari, F. De Zan, and R. Bamler. Sequential estimator : Towards efficient insar time series analysis. *IEEE Transaction on Geoscience and Remote Sensing*, 55(10) :5637 – 5652, 2017.
- H. Ansari, F. De Zan, and R. Bamler. Efficient phase estimation for interferogram stacks. *IEEE Transaction on Geoscience and Remote Sensing*, 56(7) :4109 – 4125, 2018.
- H. Ansari, F. De Zan, and A. Parizzi. Study of systematic bias in measuring surface deformation with SAR interferometry. *IEEE Transaction on Geoscience and Remote Sensing*, 59(2) :1285 – 1301, 2021.
- S. Arridge, P. Maass, O. Öktem, and C.B. Schönlieb. Solving inverse problems using data-driven models. *Acta Numerica*, pages 1–174, 2019. doi : <https://doi.org/10.1017/S0962492919000059>.
- M. G. Bato. *Towards the assimilation of deformation measurements in volcanology*. PhD thesis, Université Grenoble Alpes, 7 2018.
- M.G. Bato, V. Pinel, and Y. Yan. Assimilation of deformation data for eruption forecasting : Potentiality assessment based on synthetic cases. *Frontiers in Earth Science*, 2017. doi : [doi:10.3389/feart.2017.00048](https://doi.org/10.3389/feart.2017.00048).
- M.G. Bato, V. Pinel, Y. Yan, F. Jouanne, and J. Vandemeulebrouck. Possible deep connection between volcanic systems evidenced by sequential assimilation of geodetic data. *Scientific Reports*, 2018. doi : <https://doi.org/10.1038/s41598-018-29811-x>.

- J. M. Beckers and M. Rixen. EOF calculations and data filling from incomplete oceanographic datasets. *J. Atmos. Oceanic Technol.*, 20(12) :1836–1856, 2003.
- D.P.S. Bekaert, P. Segall, T.J. Wright, and A.J. Hooper. A network inversion filter combining GNSS and InSAR for tectonic slip modeling. *Journal of Geophysical Research*, 121 :2069–2086, 2016.
- P. Berardino, G. Fornaro, R. Lanari, and E. Santosti. A new algorithm for surface deformation monitoring based on small baseline differential sar interferograms. *IEEE Transactions on Geoscience and Remote Sensing*, 40(11) :2375–2383, 2002.
- H. Björnsson and S. A. Venegas. *A Manual for EOF and SVD Analyses of Climatic Data*. Department of Atmospheric and Oceanic Sciences and Center for Climate and Global Change Research, McGill University, 02 1997.
- J. Bolibar, A. Rabatel, I. Gouttevin, C. Galiez, T. Condom, and E. Sauquet. Deep learning applied to glacier evolution modelling. *The Cryosphere Discussion*, 14(2), 2020.
- N. Bontemps, P. Lacroix, and M.P. Doin. Inversion of deformation fields time-series from optical images, and application to the long term kinematics of slow-moving landslides in peru. *Remote Sensing of Environment*, 210 :144–158, 2018.
- J.M. Brankart, C. Ubelmann, C.E. Testut, E. Cosme, P. Brasseur, and J. Verron. Efficient parameterization of the observation error covariance matrix for square root or ensemble kalman filters : Application to ocean altimetry. *Monthly Weather Review*, 137 :1908–1926, 2009.
- D.S. Broomhead and Gregory P. King. Extracting qualitative dynamics from experimental data. *Physica D : Nonlinear Phenomena*, 20(2) :217 – 236, 1986. ISSN 0167-2789. doi : [https://doi.org/10.1016/0167-2789\(86\)90031-X](https://doi.org/10.1016/0167-2789(86)90031-X). URL <http://www.sciencedirect.com/science/article/pii/016727898690031X>.
- F. Casu, A. Manconi, A. Pepe, and R. Lanari. Deformation Time-Series Generation in Areas Characterized by Large Displacement Dynamics : The SAR Amplitude Pixel-Offset SBAS Technique. *IEEE Transactions on Geoscience and Remote Sensing*, 49(99) :1–12, 2011.
- Wen-Yen Chang, Meng-Che Wu, Yang-Lang Chang, Sheng-Yung Shih, and Bormin Huang. Gpu acceleration of adaptive local kriging applied to retrieving slant-range surface motion maps. *IEEE J. Sel. Top. Appl. Earth Obs. Remote Sens.*, 11(11) :4317–4325, 2018. doi : 10.1109/JSTARS.2018.2871877.
- C.W. Chen and H.A. Zebker. Phase unwrapping for large SAR interferograms : Statistical segmentation and generalized network models. *IEEE Transaction on Geoscience and Remote Sensing*, 40(8) :1709–1719, 2002.
- Tao Chen, Elaine Martin, and Gary Montague. Robust probabilistic pca with missing data and contribution analysis for outlier detection. *Computational Statistics & Data Analysis*, 53(10) : 3706–3716, 2009.
- J. Cohen-Waeber, R. Burgmann, E. Chaussard, C. Giannico, and A. Ferretti. Spatiotemporal patterns of precipitation-modulated landslide deformation from independent component analysis of insar time series. *Geophysical Research Letter*, 45(4) :1878–1887, 2018.
- M. Dalaison and R. Jolivet. A kalman filter time series analysis method for InSAR. *Journal of Geophysical Research*, 125(e2019JB019150), 2020.
- S . Daout, H. Sudhaus, T. Kausch, A. Steinberg, and B. Dini. Interseismic and postseismic shallowcreep of the north qaidam thrustfaults detected with a multitemporalinsar analysis. *Journal of Geophysical Research*, 124 :7259–7279, 2019. doi : <https://doi.org/10.1029/2019JB017692>.

- A. P. Dempster, N. M. Laird, and D. B. Rubin. Maximum likelihood from incomplete data via the em algorithm. *J. Royal Statistical Society. Series B (Methodological)*, 39(1) :1–38, 1977.
- M. P. Doin, C. Lasserre, G. Peltzer, O. Cavalié, and C. Doubre. Corrections of stratified tropospheric delays in SAR interferometry : Validation with global atmospheric models. *Journal of Applied Geophysics*, 69(1) :35–50, 2009.
- M.P. Doin, S. Guillaso, R. Jolivet, C. Lasserre, F. Lodge, G. Ducret, and R. Grandin. Presentation of the small baseline NSBAS processing chain on a case example : the Etna deformation monitoring from 2003 to 2010 using Envisat data. In *Proceedings of the European Space Agency Symposium "Fringe"*, 2011.
- S. K. Ebmeier. Application of independent component analysis of multitemporal insar data with volcanic case studies. *Journal of Geophysical Research*, 121 :8970–8986, 2016.
- G. Evensen. The Ensemble Kalman Filter : theoretical formulation and practical implementation. *Ocean Dynamics*, 53 :343–367, 2003. doi : 10.1007/s10236-003-0036-9.
- Renaud Fallourd. *Monitoring alpine glaciers by combination of heterogeneous informations : High Resolution SAR image and ground measurements*. Thèse de doctorat, Université de Grenoble, April 2012. URL <https://tel.archives-ouvertes.fr/tel-00718596>.
- A. Ferretti, C. Prati, and F. Rocca. Permanent scatterer in SAR interferometry. *IEEE Transactions on Geoscience and Remote Sensing*, 39(1) :8–20, 2001.
- A. Ferretti, F. Novali, F. De Zan, C. Prati, and F. Rocca. Moving from ps to slowly decorrelating targets : a prospective view. In *Proceedings of the European Conference on Synthetic Aperture Radar*, 2008.
- A. Ferretti, A. Fumagalli, F. Novali, C. Prati, F. Rocca, and A. Rucci. A new algorithm for processing interferometric data-stacks : SqueeSAR. *IEEE Transactions on Geoscience and Remote Sensing*, 49(9) :3460–3470, 2011.
- G. Fornaro, S. Verde, D. Reale, and A. Pauciuolo. Caesar : An approach based on covariance matrix decomposition to improve multibaseline - multitemporal interferometric SAR processing. *IEEE Transactions on Geoscience and Remote Sensing*, 53(4) :2050–2065, 2015.
- A. Fournier, C. Eymin, and T. Alboussiere. A case for variational geomagnetic data assimilation : insights from a one-dimensional, nonlinear, and sparsely observed MHD system. *Nonlinear processes in Geophysics*, 14 :163–180, 2007a.
- A. Fournier, G. Hulot, D. Jault, W. Kuang, A. Tangborn, N. Gillet, E. Canet, J. Aubert, and F. Lhuillier. An introduction to data assimilation and predictability in geomagnetism. *Space Science Reviews*, 155(1-4) :247–291, 2007b.
- Gabriel Frahm and Uwe Jaekel. A generalization of tyler’s m-estimators to the case of incomplete data. *Computational Statistics & Data Analysis*, 54(2) :374–393, 2010.
- M.E. Gaddes, A. Hopper, M. Bagnardi, H. Inman, and F. Albino. Blind signal separation methods for InSAR : The potential to automatically detect and monitor signals of volcanic deformation. *Journal of Geophysical Research*, 123 :10266–10251, 2018.
- M.E. Gaddes, A. Hopper, and M. Bagnardi. Using machine learning to automatically detect volcanic unrest in a time series of interferograms. *Journal of Geophysical Research*, 124 : 12304–12322, 2019.

- Florian Gerber, Rogier de Jong, Michael E. Schaepman, Gabriela Schaepman-Strub, and Reinhard Furrer. Predicting missing values in spatio-temporal remote sensing data. *IEEE Trans. Geosci. Remote Sens.*, 56(5) :2841–2853, 2018.
- A. Gesrt. Probabilistic inversion methods. In Y. Yan, editor, *Inversion & Data Assimilation*. ISTE – John Wiley Sons, 2021.
- M. Ghil, M.R. Allen, M. D Dettinger, K. Ide, D. Kondrashov, M.E. Mann, A.W. Robertson, A. Saunders, Y. Tian, F. Varadi, and P. Yiou. Advanced spectral methods for climatic time series. *Review of Geophysics*, 40, 1 :1–41, 2002.
- S. Giffard-Roisin, M. Yang, G. Charpiat, C. Kumler-Bonfanti, B. Kégl, and C. Monteleoni. Tropical cyclone track forecasting using fused deep learning from aligned reanalysis data. *Frontiers in Big Data*, 2020. doi : <https://doi.org/10.3389/fdata.2020.00001>.
- F. Gillet-Chaulet, G. Durand, O. Gagliardini, C. Mosbeux, J. Mouginot, F. Rémy, and C. Ritz. the form of the basal friction law under pine island glacier. *Geophysical Research Letter*, 43 : 10311–10321, 2016.
- R. Goldstein and C. Werner. Radar interferogram filtering for geophysical applications. *Geophysical Research Letter*, 25(21) :4035 – 4038, 1998.
- N.E. Golyandina and K.D. Usevich. 2d-extension of singular spectrum analysis : Algorithm and elements of theory. *Matrix Methods : Theory, Algorithms and Applications*, pages 449–473, 2010.
- P.M. Gregg and J.C. Pettijohn. A multi-data stream assimilation framework for the assessment of volcanic unrest. *Journal of Volcanology and Geothermal Research*, 309 :63–77, 2016.
- Andreas Groth and Michael Ghil. Monte carlo singular spectrum analysis (ssa) revisited : Detecting oscillator clusters in multivariate datasets. *J. Climate*, 28(19) :7873–7893, 2015. doi : 10.1175/JCLI-D-15-0100.1. URL <https://doi.org/10.1175/JCLI-D-15-0100.1>.
- A. M. Guarnieri and S. Tebaldini. On the exploitation of target statistics for sar interferometry applications. *IEEE Transaction on Geoscience and Remote Sensing*, 46(11) :3436–3443, 2008.
- A. Monti Guarnieri and S. Tebaldini. Hybrid cramér-Rao bounds for crustal displacement field estimators in SAR interferometry. *IEEE Signal Processing Letters*, 14(12) :1012–1015, 2007.
- Sverrir Gudmundsson, Freysteinn Sigmundsson, and Jens Carstensen. Three-dimensional surface motion maps estimated from combined interferometric synthetic aperture radar and gps data. *J. Geophys. Res.*, 107, 10 2002. doi : 10.1029/2001JB000283.
- H. Hadhri, F. Vernier, A. Atto, and E. Trouvé. Time-lapse optical flow regularization for geophysical complex phenomena monitoring. *ISPRS Journal of Photogrammetry and Remote Sensing*, 150 : 135–156, 2019.
- A. Hannachi, I.T. Jolliffe, and D.B. Stephenson. Empirical orthogonal functions and related techniques in atmospheric science : A review. *Int. J. Climatol.*, 27 :1119–1152, 2007.
- Frédéric Herman, Brian Anderson, and Sébastien Leprince. Mountain glacier velocity variation during a retreat/advance cycle quantified using sub-pixel analysis of aster images. *J. Glaciol.*, 57(202) :197–207, 2011. doi : 10.3189/002214311796405942.
- E.A. Hetland, P. Musé, M. Simons, Y.N. Lin, P.S. Agram, and C.J. DiCaprio. Multiscale InSAR time series analysis of surface deformation. *Journal of Geophysical Research*, 117(B02404), 2012.

-
- A. Hippert-Ferrer. *Missing data imputation in SAR displacement time series*. PhD thesis, Université Savoie Mont-Blanc, 10 2020.
- A. Hippert-Ferrer, Y. Yan, and P. Bolon. Em-eof : gap filling in incomplete sar displacement time series. *IEEE Transaction on Geoscience and Remote Sensing*, 2020a. doi : 10.1109/TGRS.2020.3015087.
- A. Hippert-Ferrer, Y. Yan, and P. Bolon. Spatiotemporal filling of missing data in remotely sensed displacement measurement time series. *IEEE Geoscience and Remote Sensing Letters*, 2020b. doi : 10.1109/LGRS.2020.3015149.
- K. Hocke and N. Kämpfer. Gap filling and noise reduction of unevenly sampled data by means of the lomb-scargle periodogram. *Atmos. Chem. Phys.*, 9(12) :4197–4206, 2009. doi : 10.5194/acp-9-4197-2009. URL <https://www.atmos-chem-phys.net/9/4197/2009/>.
- A. Hooper. A multi-temporal InSAR method incorporating both persistent scatterer and small baseline approaches. *Geophysical Research Letters*, 35, 2008.
- A.J. Hooper, P. Segall, and H.A. Zebker. Persistent scatterer interferometric synthetic aperture radar for crustal deformation analysis with application to Volcan Alcedo, Galapagos. *Journal of Geophysical Research*, 112(B07407), 2007.
- J. Hu, X.L. Ding, L. Zhang, Q. Sun, Z.W. Li, J.J. Zhu, and Z. Lu. Estimation of 3-d surface displacement based on InSAR and deformation modeling. *IEEE Transactions on Geosciences and Remote Sensing*, 55(4) :2007–2016, 2017.
- M. Jacquemont, T. Vuillaume, A. Benoit, G. Maurin, and P. Lambert. Deep learning for astrophysics, understanding the impact of attention on variability induced by parameter initialization. In *Proceedings of the ICPR'2020 Workshop Explainable Deep Learning-AI*, 2021.
- M. Jauvin, Y. Yan, E. Trouvé, B. Fruneau, M. Gay, and B. Girard. Integration of corner reflectors for the monitoring of mountain glacier areas with sentinel-1 time series. *Remote Sensing*, 11(8) :988, 2019. doi : <https://doi.org/10.3390/rs11080988>.
- R. Jolivet and M. Simons. A multipixel time series analysis method accounting for ground motion, atmospheric noise, and orbital errors. *Geophysical Research Letters*, 45 :1814–1824, 2018.
- R. Jolivet, R. Grandin, C. Lasserre, M.-P. Doin, and G. Peltzer. Systematic insar tropospheric phase delay corrections from global meteorological reanalysis data. *Geophys. Res. Lett.*, 38(17), 2011. doi : 10.1029/2011GL048757.
- R. Jolivet, C. Lasserre, M.P. Doin, S. Guillaso, G. Peltzer, and R. Dailu. Shallow creep on the haiyuan fault (gansu china) revealed by SAR interferometry. *Journal of Geophysical Research*, 117(B06401), 2012.
- B. M. Kampes. *Radar interferometry : persistent scatterer technique*. Springer, 2006.
- M. Katzfuss and N. Cressie. Spatio-temporal smoothing and EM estimation for massive remote sensing data sets. *Journal of Time Series Analysis*, 32 :430–446, 2011.
- D. Kondrashov and M. Ghil. Spatio-temporal filling of missing points in geophysical data sets. *Nonlinear Processes Geophys.*, 13 :151–159, 2006.
- A. P. Kositsky and J.-P. Avouac. Inverting geodetic time series with a principal component analysis-based inversion method. *J. Geophys. Res.*, 115(B03401), 2010.
-

- Andreas Kääb, Solveig H. Winsvold, Bas Altena, Christopher Nuth, Thomas Nagler, and Jan Wuite. Glacier remote sensing using sentinel-2. part i : Radiometric and geometric performance, and application to ice velocity. *Remote Sensing*, 8(7), 2016. ISSN 2072-4292. doi : 10.3390/rs8070598. URL <https://www.mdpi.com/2072-4292/8/7/598>.
- E. Laloy, R. Hérault, D. Jacques, and N. Linde. Training-image based geostatistical inversion using a spatial generative adversarial neural network. *Water Resources Research*, 54 :381–406, 2018.
- E. Laloy, N. Linde, C. Ruffino, R. Hérault, G. Gasso, and D. Jacques. Gradient-based deterministic inversion of geophysical data with generative adversarial networks : is it feasible ? *Computers & Geosciences*, 133(104333), 2019.
- R. Lanari, O. Mora, M. Manunta, J.J. Mallorqui, P. Berardino, and E. Sansosti. A Small-Baseline Approach for Investigating Deformations on Full-Resolution Differential SAR Interferograms. *IEEE Transaction on Geoscience and Remote Sensing*, 42(7) :1377–1386, 2004.
- H. Liang, L. Zhang, X. Ding, Z. Lu, X. Li, J. Hu, and S. Wu. Suppression of coherence matrix bias for phase linking and ambiguity detection in mtinsar. *IEEE Transaction on Geoscience and Remote Sensing*, 59(2) :1263 – 1274, 2021.
- Chao-Hung Lin, Kean-Hua Lai, Zhi-Bin Chen, and Jyun-Yuan Chen. Patch-based information reconstruction of cloud-contaminated multitemporal images. *IEEE Trans. Geosci. Remote Sens.*, 52(1) :163–174, 2014.
- R. J. A. Little and D. B. Rubin. *Statistical analysis with Missing Data*. Wiley, New York, 2nd edition, 2002.
- Chuanhai Liu. Efficient ml estimation of the multivariate normal distribution from incomplete data. *Journal of Multivariate Analysis*, 69 :206–217, 1999. doi : 10.1006/jmva.1998.1793.
- J.H. Liu, J. Hu, Z.W. Li, J.J. Zhu, Q. Sun, and J. Gan. A method for measuring 3-d surface deformations with insar based on strain model and variance component estimation. *IEEE Transactions on Geosciences and Remote Sensing*, 56(1) :239–250, 2018.
- Junyan Liu and Daniel P. Palomar. Regularized robust estimation of mean and covariance matrix for incomplete data. *Signal Processing*, 165 :278 – 291, 2019. ISSN 0165-1684. doi : <https://doi.org/10.1016/j.sigpro.2019.07.009>. URL <http://www.sciencedirect.com/science/article/pii/S0165168419302622>.
- F. Locatello, S. Bauer, M. Lucic, G. Rätsch, S. Gelly, B. Schölkopf, and O. Bachem. Challenging common assumptions in the unsupervised learning of disentangled representations. In *Proceedings of the 36th International Conference on Machine Learning*, 2019.
- P. Lopez-Quiroz, M.P. Doin, F. Tupin, P. Briole, and J.M. Nicolas. Time series analysis of mexico city subsidence constrained by radar interferometry. *Journal of Applied Geophysics*, 69 :1–15, 2009.
- F. Magrini, D. Jozinović, F. Cammarano, A. Michelini, and L. Boschi. Local earthquakes detection : A benchmark dataset of 3-component seismograms built on a global scale. *Artificial Intelligence in Geosciences*, 1 :1–10, 2020. doi : <https://doi.org/10.1016/j.aiig.2020.04.001>.
- G. Marsy, F. Vernier, X. Bodin, E. Trouvé, W. Castaings, A. Walpersdorf, E. Malet, and B. Girard. Temporal consolidation strategy for ground based image displacement time series. *IEEE Journal of Selected Topics in Applied Earth Observations and Remote Sensing*, 2021.

- L. Maubant, E. Pathier, S. Daout, M. Radiguet, M.-P. Doin, E. Kazachkina, V. Kostoglodov, N. Cotte, and A. Walpersdorf. Independent component analysis and parametric approach for source separation in insar time series at regional scale : Application to the 2017–2018 slow slip event in guerrero (mexico). *Journal of Geophysical Research : Solid Earth*, 125(3) :e2019JB018187, 2020. doi : 10.1029/2019JB018187. URL <https://agupubs.onlinelibrary.wiley.com/doi/abs/10.1029/2019JB018187>.
- F. Melgani. Contextual Reconstruction of Cloud-Contaminated Multitemporal Multispectral Images. *IEEE Trans. Geosci. Remote Sens.*, 44 :442–455, February 2006. doi : 10.1109/TGRS.2005.861929.
- A. Mian, G. Ginolhac, J.P. Ovarlez, and A. Atto. New robust statistics for change detection in time series of multivariate SAR images. *IEEE Transactions on Signal Processing*, 67(2) :520–534, 2019.
- Romain Millan, Jérémie Mouginot, Antoine Rabatel, Seongsu Jeong, Diego Cusicanqui, Anna Derkacheva, and Mondher Chekki. Mapping surface flow velocity of glaciers at regional scale using a multiple sensors approach. *Remote Sensing*, 11(21), 2019. ISSN 2072-4292. doi : 10.3390/rs11212498. URL <https://www.mdpi.com/2072-4292/11/21/2498>.
- K. Mosegaard and A. Tarantola. Monte carlo sampling of solutions to inverse problems. *Journal of Geophysical Research*, 100 :12431–12447, 1995.
- L. Mosser, W. Kimman, J.S. Dramsch, S. Purves, A. De la Fuente, and G. Ganssle. Rapid seismic domain transfer : Seismic velocity inversion and modeling using deep generative neural networks. In *Proceedings of 80th EAGE Annual Conference and Exhibition 2018 European Association of Geoscientists and Engineers*, 2018.
- Gerald R. North, Thomas L. Bell, Robert F. Cahalan, and Fanthune J. Moeng. Sampling errors in the estimation of empirical orthogonal functions. *Mon. Weather Rev.*, 110(7) :699–706, 1982. doi : 10.1175/1520-0493(1982)110<0699:SEITEO>2.0.CO;2. URL [https://doi.org/10.1175/1520-0493\(1982\)110<0699:SEITEO>2.0.CO;2](https://doi.org/10.1175/1520-0493(1982)110<0699:SEITEO>2.0.CO;2).
- James Overland and R W. Preisendorfer. A significance test for principal components applied to a cyclone climatology. *Mon. Weather Rev.*, 110 :1, 01 1982. doi : 10.1175/1520-0493(1982)110<0001:ASTFPC>2.0.CO;2.
- B. Pinel-Puysségur, R. Michel, and J.P. Avouac. Multi-Link InSAR time series : Enhancement of a wrapped interferometric database. *IEEE Journal of Selected Topics in Applied Earth Observations and Remote Sensing*, 5(3) :784–794, 2012.
- Rudolph W. Preisendorfer. *Principal Component Analysis in Meteorology and Oceanography*. Elsevier, 1988.
- R. Prébet, Y. Yan, M. Jauvin, and E. Trouvé. A data-adaptive eof-based method for displacement signal retrieval from insar displacement measurement time series for decorrelating targets. *IEEE Transaction on Geoscience and Remote Sensing*, 57(8) :5829–5852, 2019.
- T. Reverso, J. Vandemeulebrouck, F. Jouanne, V. Pinel, T. Villemin, E. Sturkell, and P. Bascou. A two-magma chamber model as a source of deformation at grímsvötn volcano, iceland. *Journal of Geophysical Research : Solid Earth*, 119(6) :4666 – 4683, 2014.
- F. Rocca. Modelling interferogram stacks. *IEEE Transaction on Geoscience and Remote Sensing*, 45(10) :3289–3299, 2007.
- Donald B. Rubin. Inference and missing data. *Biometrika*, 63(3) :581–592, 1976.

- G. A. Ruggiero, E. Cosme, J.-M. Brankart, J. Le Sommer, and C. Ubelmann. An efficient way to account for observation error correlations in the assimilation of data from the future SWOT high-resolution altimeter mission. *Journal of Atmospheric and Oceanic Technology*, 33(12) : 2755–2768, 2016.
- N. Sambridge and K. Mosegaard. Monte carlo methods in geophysical inverse problems. *Reviews of Geophysics*, 40(3) :3–1–3–29, 2002.
- S. Samiei-Esfahany, J. Esteves Martins, F. van Leijen, and R.F. Hanssen. Phase estimation for distributed scatterers in InSAR stacks using integer least squares estimation. *IEEE Transaction on Geoscience and Remote Sensing*, 54(10) :5671–5687, 2016.
- M. Schmitt, J.L. Schonberger, and U. Stilla. Adaptive covariance matrix estimation for multi-baseline InSAR data stacks. *IEEE Transaction on Geoscience and Remote Sensing*, 52(11) : 6807–6817, 2014.
- Tapio Schneider. Analysis of incomplete climate data : Estimation of mean values and covariance matrices and imputation of missing values. *J. Climate*, 14 :853–871, 2001.
- P. Segall. Volcano deformation and eruption forecasting. *Geological Society, London, Special Publications*, 380 :85–106, 2013.
- X. Shi, Z. Chen, H. Wang, D.Y. Yeung, W.K. Wong, and W.C. Woo. Convolutional lstm network : A machine learning approach for precipitation nowcasting. *Advances in neural information processing systems*, pages 802–810, 2015.
- F. Sica, F. Calvanese, G. Scarpa, and P. Rizzoli. A CNN-based coherence-driven approach for InSAR phase unwrapping. *IEEE Geoscience and Remote Sensing Letters*, 2021. doi : 10.1109/LGRS.2020.3029565.
- Albert Tarantola. *Inverse problem theory and methods for model parameter estimation*. SIAM, 2005.
- H. J. Thiébaux and F. W. Zwiers. The interpretation and estimation of effective sample size. *J. Climate Appl. Meteor.*, 23(5) :800–811, 1984. doi : 10.1175/1520-0450(1984)023<0800:TIAEOE>2.0.CO;2. URL [https://doi.org/10.1175/1520-0450\(1984\)023<0800:TIAEOE>2.0.CO;2](https://doi.org/10.1175/1520-0450(1984)023<0800:TIAEOE>2.0.CO;2).
- M. Titos, A. Bueno, L. Garcia, M.C. Benitez, and J. Ibanez. Detection and classification of continuous volcano-seismic signals with recurrent neural networks. *IEEE Transaction on Geoscience and Remote Sensing*, 57(4) :1936 – 1948, 2019.
- S. Usai. A least squares database approach for sar interferometric data. *IEEE Transactions on Geoscience and Remote Sensing*, 41(4) :753–760, 2003.
- K. Vardaan, T. Bhandarkar, N. Satish, S. Sridhar, R. Sivakumar, and S. Ghosh. Earthquake trend prediction using long short-term memory RNN. *International Journal of Electrical and Computer Engineering*, 9(2) :1304–1312, 2019.
- Alexandre Verger, Frédéric Baret, Marie Weiss, Sivasathivel Kandasamy, and Eric Vermote. The cacao method for smoothing, gap filling and characterizing seasonal anomalies in satellite time series. *IEEE Trans. Geosci. Remote Sens.*, 51(4) :1963–1972, 2013.
- F. Vernier, R. Fallourd, J.M. Friedt, Y. Yan, E. Trouvé, J.M. Nicolas, and L. Moreau. Fast correlation technique for glacier flow monitoring by digital camera and space-borne sar images. *EURASIP Journal on Image and Video Processing*, 11, 2011. doi : 10.1186/1687-5281-2011-11.

- Y. Wang and X. Zhu. Robust estimators for multipass SAR Interferometry. *IEEE Transaction on Geoscience and Remote Sensing*, 54(2) :968–980, 2016.
- C.J. Willmott and K. Matsuura. On the use of dimensioned measures of error to evaluate the performance of spatial interpolators. *International Journal of Geographic Information Science*, 20(1) :89 – 102, 2006.
- T. Wright, B. Parsons, and E. Fielding. Measurement of interseismic strain accumulation across the north anatolian fault by satellite radar interferometry. *Geophysical Research Letters*, 28(10) : 2117–2120, 2001.
- Meng-Che Wu, Jian Guo Liu, and Philippa Jane Mason. Adaptive local kriging to retrieve slant-range surface motion maps of the wenchuan earthquake. *Int. J. Remote Sens.*, 34(21) :7589–7606, 2013. doi : 10.1080/01431161.2013.822600.
- Wei Wu, Luoqi Ge, Jiancheng Luo, Ruohong Huan, and Yingpin Yan. A spectral-temporal patch-based missing area reconstruction for time-series images. *Remote Sensing*, 10 :1560, 2018.
- Y. Yan, M.P. Doin, P. Lopez-Quiroz, F. Tupin, B. Fruneau, V. Pinel, and E. Trouvé. Mexico City subsidence measured by insar time series : Joint analysis using PS and SBAS approaches. *IEEE Journal of Selected Topics in Applied Earth Observations and Remote Sensing*, 5(4) : 1312–1326, 2012a.
- Y. Yan, G. Mauris, E. Trouvé, and V. Pinel. Fuzzy uncertainty representations of co-seismic displacement measurements issued from sar imagery. *IEEE Transactions on Instrumentation & Measurement*, 61(5) :1278–1286, 2012b.
- Y. Yan, V. Pinel, E. Trouvé, E. Pathier, J. Perrain, P. Bascou, and F. Jouanne. Coseismic slip distribution of the 2005 kashmir earthquake from SAR amplitude image correlation and differential interferometry. *Geophysical Journal International*, 193(1) :29–46, 2013.
- Y. Yan, A. Barth, and J.M. Beckers. Comparison of different assimilation schemes in a sequential Kalman filter assimilation system. *Ocean Modelling*, 73 :123–137, 2014.
- Y. Yan, A. Barth, J.M. Beckers, G. Candille, J.M. Brankart, and P. Brasseur. Ensemble assimilation of ARGO temperature profile, sea surface temperature, and altimetric satellite data into an eddy permitting primitive equation model of the North Atlantic Ocean. *Journal of Geophysical Research. Oceans*, 120, 2015. doi : 10.1002/2014JC010349.
- Y. Yan, A. Dehecq, E. Trouvé, G. Mauris, N. Gourmelen, and F. Vernier. Fusion of remotely sensed displacement measurements : Current status and challenges. *IEEE Geoscience and Remote Sensing Magazine*, 4(1) :6–25, 2016.
- Yajing Yan. *Fusion of displacement measurements from SAR imagery : application to seismo-volcanic modeling*. Thèse de doctorat, Université de Grenoble, 2011. URL <https://tel.archives-ouvertes.fr/tel-00667990>.
- Y. Zhan and P.M. Gregg. Data assimilation strategies for volcano geodesy. *Journal of Volcanology and Geothermal Research*, 344 :13–25, 2017.
- Y. Zhan, P.M. Gregg, E. Chaussard, and Y. Aoki. Sequential assimilation of volcanic monitoring data to quantify eruption potential : Application to kerinci volcano, sumatra. *Front. Earth Sci.*, 19, 2017. doi : <https://doi.org/10.3389/feart.2017.00108>.

- Q. Zhang, Q. Yuan, C. Zeng, X. Li, and Y. Wei. Missing data reconstruction in remote sensing image with a unified spatial–temporal–spectral deep convolutional neural network. *IEEE Trans. Geosci. Remote Sens.*, 56(8) :4274–4288, Aug 2018. ISSN 0196-2892. doi : 10.1109/TGRS.2018.2810208.
- R. Zhang, Z. Chen, S. Chen, J. Zheng, O. Buyukozturk, and H. Sun. Deep long short-term memory networks for nonlinear structural seismic response prediction. *Computers and Structures*, 220 : 55–68, 2019.
- Z. Zhang and Y. Lin. Data-driven seismic waveform inversion : a study on the robustness and generalization. *IEEE Transaction on Geoscience and Remote Sensing*, 58(10) :6900–6913, 2020.
- L. Zhou, H. Yu, and Y. Lan. Deep convolutional neural network-based robust phase gradient estimation for two-dimensional phase unwrapping using SAR interferograms. *IEEE Transaction on Geoscience and Remote Sensing*, 58(7) :4653 – 4665, 2020.

Vers la surveillance opérationnelle de la déformation de la Terre et la prévision des risques naturels

Towards operational monitoring of Earth deformation and prediction of natural hazards

Résumé

Mon activité de recherche se développe autour de l'imagerie SAR (Synthetic Aperture Radar), mais couvre un spectre large des sujets allant de l'exploitation des images SAR pour la mesure de déplacement à la surface de la Terre jusqu'à l'estimation des paramètres géophysiques qui caractérisent la source en profondeur du déplacement observé en surface. Je m'intéresse à la fois aux développements méthodologiques, notamment ceux pour mieux exploiter la masse de données SAR disponibles, et aux applications des méthodes aux objets d'intérêt géophysiques telles que les séismes, les volcans, les subsidences en milieux urbains et les glaciers alpins. Dans ce rapport, je présente de manière synthétique mes travaux de recherche menés ces dernières années essentiellement à travers des stages et thèses que j'ai co-encadrés ou co-encadre ; je présente également l'état de l'art permettant un positionnement approprié de mes travaux, ainsi que les perspectives de mon activité de recherche. Ces travaux seront présentés suivant quatre axes de recherche organisés selon quatre objectifs scientifiques différents : l'estimation du déplacement à partir de séries temporelles d'images SAR, la reconstruction des données manquantes dans les séries temporelles de déplacement SAR/optique, l'analyse des séries temporelles de mesure de déplacement, et l'estimation et la prédiction des paramètres géophysiques.

Mots-clés : SAR, multi-temporal InSAR, mesure de déplacement, série temporelle, inversion, assimilation de données

Abstract

My research activities have been developed around Synthetic Aperture Radar (SAR) imagery, but cover a wide spectrum of subjects starting from the exploitation of SAR images for displacement measurement at the Earth's surface until the estimation of geophysical parameters which characterize the subsurface geological structures that induce the displacement observed at the surface. I am interested in both methodological developments, especially those to better exploit the mass of available SAR data, and applications of the methods to targets of geophysical interest such as earthquakes, volcanoes, subsidence in urban environments and alpine glaciers. In this report, I give a summary of my research works carried out in recent years, mainly through Master internships and Ph.D theses that I co-supervised or co-supervise. I also introduce the related state-of-the-art works, as well as the perspectives of my research activities. These works will be presented in line with four research axes organized according to four different scientific objectives : estimation of the displacement from time series of SAR images, reconstruction of the missing data in the time series of SAR/optical displacement, analysis of the time series of displacement measurement and estimation and prediction of geophysical parameters.

Keywords : SAR, multi-temporal InSAR, displacement measurement, time series, inversion, data assimilation